NASA Contractor Report 4779

Three Dimensional Viscous Flow Field in an Axial Flow Turbine Nozzle Passage

D. Ristić and B. Lakshminarayana
Pennsylvania State University
University Park, Pennsylvania

Prepared for
Lewis Research Center
under Grant NAG3–555

National Aeronautics and
Space Administration

Office of Management
Scientific and Technical
Information Program

1997

ABSTRACT

The objective of this investigation is experimental and computational study of three dimensional viscous flow field in the nozzle passage of an axial flow turbine stage. The nozzle passage flow field has been measured using a two sensor hot-wire probe at various axial and radial stations. In addition, two component LDV measurements at one axial station (x/c_m=0.56) were performed to measure the velocity field. Static pressure measurements and flow visualization, using a fluorescent oil technique, were also performed to obtain the location of transition and the endwall limiting streamlines. A three dimensional boundary layer code, with a simple intermittency transition model, was used to predict the viscous layers along the blade and endwall surfaces. The boundary layers on the blade surface were found to be very thin and mostly laminar, except on the suction surface downstream of 70% axial chord. Strong radial pressure gradient, especially close to the suction surface, induces strong cross flow components in the trailing edge regions of the blade. On the endwalls the boundary layers were much thicker, especially near the suction corner of the casing surface, caused by secondary flow. The secondary flow region near the suction-casing surface corner indicates the presence of the passage vortex detached from the blade surface. The corner vortex is found to be very weak.

The presence of a closely spaced rotor downstream (20% of the nozzle vane chord) introduces unsteadiness in the blade passage. The measured instantaneous velocity

signal was filtered using FFT square window to remove the periodic unsteadiness introduced by the downstream rotor and fans. The filtering decreased the free stream turbulence level from 2.1% to 0.9% but had no influence on the computed turbulence length scale.

The computation of the three dimensional boundary layers is found to be accurate on the nozzle passage blade surfaces, away from the endwalls and the secondary flow region. On the nozzle passage endwall surfaces the presence of strong pressure gradients and secondary flow limit the validity of the boundary layer code.

TABLE OF CONTENTS

LIST OF TABLES

Page no.

LIST OF FIGURES

Page no.

NOMENCLATURE

A	-King's law coefficient or damping factor.
A_α	-Hot-wire angular calibration coefficient.
B	-King's law coefficient.
c	-Axial chord.
c_t	-Axial chord at blade tip.
c_m	-Axial chord at midspan.
C_{fs}	-Skin friction coefficient (Equation 4.9).
C_P	-Nozzle static pressure coefficient. $(p-P_{01}) / \frac{1}{2}\rho V_{x1}^2$
d	-Wire distance from wall or wire thickness.
E	-Output voltage.
f	-Frequency.
g	-Metric tensor
H	-Spanwise distance. $(r-r_h)/(r_t-r_h)$ (H=0.0 hub, H=1.0 casing surface)
H_2	-Metric tensor in the ξ_2 direction (Equation 4.3)
H_{ss}	-Shape factor.(δ_s^*/θ_s)
h	-Static enthalpy
J	-Jacobian.
k	-wire cooling coefficient.
l	-Wire length or length scale.

l_{ref}	-Reference length.
$\dot{m}$	-Mass flow rate.
N	-Rotations per minute.
n	-King's law logarithmic slope coefficient.
P,p	-Pressure.
P_0	-Total Pressure
q_0	-Levy-Lees Length scale(Equation 4.3)
r	-Radius measured from facility centerline.
R	-Reaction.
Re	-Reynolds number.
s,c,n	-Surface coordinates in the streamwise, crosswise, and normal direction (see Figure 4.1).
S	-Pitch wise distance normalized by blade spacing (S=0.0 suction, S=1.0 pressure surface).
T_0	-Total temperature.
Tu	-Total turbulence intensity.
U	-Free steam total velocity.
U_m	-Rotor blade speed at midspan.
U_{cf}	-Hot-wire velocity calibration coefficient.
u,v,w	-Velocity components in three-dimensional boundary layers.
V	-Total or mean velocity.
v'	-Velocity fluctuation (Equation 3.2)

v_s', v_c'	-Instantaneous velocity fluctuation in the streamwise and crosswise direction.
W	-Mass flow rate.
x,y,z	-Cartesian coordinate variables (See Fig 4.1).
x,r,θ	-Turbine cylindrical coordinate system.
u^*	-Friction velocity $= \sqrt{\tau_w / \rho}$.
α	-Probe rotation angle or yaw angle.
β	-Three dimensional boundary layer skew angle or radial angle.
δ	-Boundary layer thickness.
δ^*	-Boundary layer displacement thickness (Equation 4.5 and 4.6).
ϕ	-Wire angle.
Γ	-Intermitency factor.
η	-Efficiency.
μ	-Viscosity.
μ_t	-Turbulent viscosity.
θ^*	-Boundary layer momentum thickness (Equation 4.6 and 4.7).
ρ	-Density.
τ	-Shear stress or time variable.
ξ_1, ξ_2, ξ_3	-Levi-Lees variables.
ψ	-Loading coefficient ($\Delta h_o/U_m^2$).

Subscript

c	-Cross wise flow direction.
cal	-Calibration value.
e	-Effective.
edge	-Boundary layer edge conditions.
inner	-Inner region variable.
in	-Input Value.
i	-Instantaneous value.
m	-Measured or mean value.
outer	-Outer region variable.
p	-Probe coordinates.
ref	-Reference value.
rot	-Rotor.
s	-Stream wise flow direction.
stat	-Stator
t	-Tip.
T	-Total value.
TT	-Total to Total.
tran	-Transition.
w	-Wall property.
xw	-X-wire probe.
1,3	-One axial chord upstream of nozzle and one chord downstream of rotor

location.

x,r,θ	-Axial, radial, and tangential directions.
1,2	-Wire 1 and wire 2.
∞	-Free stream value.

Superscripts

‘	-Instantaneous fluctuations.
“	-Probe coordinate system.
–	-Average value.

ACKNOWLEDGEMENTS

The research was supported by NASA Lewis Research Center through Grant NSG-3-555, with R. Boyle and K. Civinskas as technical monitors. The LDV system used in this research program was acquired with the funds provided by the NSF through Equipment Grant MSME-85-06626.

The assistance of M. Zaccaria, L. Gourgeon and other members of the Turbomachinery Group in acquiring this data is also acknowledged. Thanks are also extended to J. Fetterolf for his assistance with the hot wire equipment.

CHAPTER 1

INTRODUCTION AND LITERATURE REVIEW

In a constant quest for improved performance and efficiency the turbine designers have steadily increased the operating temperatures and pressures. This has resulted in a trend toward a decrease in blade height, longer chord length, and an increase in the thickness of the leading and trailing edges of the blade partly due to the cooling requirements of these critical locations. The lower aspect ratios result in increased viscous losses.

The flow field in modern turbomachinery is highly complex due to a variety of flow conditions throughout the stages. The flow field in a turbine nozzle passage includes regions of viscid and inviscid flow, which can include regions of highly three-dimensional flow field in typical modern blade design. In addition, the flow field can be steady and unsteady, including: laminar, transitional, turbulent, and separated flows. Interaction of the developing boundary layers (usually along a curved flow path) on the blade, hub, and casing surfaces leads to generation of secondary flow regions and complex flow field in the endwall regions. The flow field can include regions of subsonic, transonic and supersonic flows, with complex phenomena such as shock wave boundary layer interaction. Non-uniformity in the flow field leads to off design conditions and unsteady flow in subsequent stages resulting in higher losses and flow separation. The flow field is further complicated by the presence of periodic wakes propagating through the stationary

and rotating blade passages.

In the nozzle passage the two dominant effects are the presence of three dimensional boundary layers influenced by the existence of cross flow (radial and transverse) pressure gradients and the development of secondary flows.

1.1 Nozzle Passage Flow Field

The flow field in the nozzle passage of a single stage axial flow turbine is initially uniform and mostly inviscid. Over a large region of the passage at the inlet the flow field is generally two dimensional and steady. The presence of a developing boundary layer region along the endwalls influence only the regions in close proximity to the boundaries. Along the surface of the blade, downstream of the leading edge, a three-dimensional boundary layer begins to develop due to the pressure gradient in the radial direction. The pressure gradient in the radial direction, produced by the change in swirl, induces radial inward flows in the boundary layers along the blade surfaces. In the endwall regions the blade-to-blade pressure gradient tends to transport fluid from pressure surface toward the suction surface resulting in three dimensional boundary layers or secondary flows near the endwalls.

The dominant viscous effects in the nozzle passage are therefore present in the form of secondary flow effects near endwalls and development of two and three dimensional blade boundary layers which are described in more detail in the following sections and will be the major objective of this exploration.

1.1.1 Secondary Flow in Turbine Nozzle Passage

The classical model for secondary flows in cascades was proposed by Hawthorne (1955) and is shown in Figure 1.1a. The vortex system in the downstream endwall region arises from the distortion and convection of the vortex filaments in the inlet boundary layer passing through the curved passage. In addition, the vortex sheet is composed of trailing filaments, due to the differing velocities along the suction and pressure surfaces, and the trailing shed vorticity arising from the change in the blade circulation. In subsequent experiments this theoretical model was found to be inadequate for turbines. The secondary flow model was refined by Klein (1966) by recognizing the existence of a horseshoe vortex originating from the rotation into a vortical motion of an endwall boundary layer developing along the leading edge of the blade. The horseshoe vortex originates at the leading edge of the blade and rolls into the passage vortex shown in Figure 1.1b - Klein called this a stagnation point vortex. Based on the experimental data (utilizes three dimensional pressure probe and flow visualization of limiting streamlines) Langston et al. (1977) proposed a modification to Klein's model by including the merging of the pressure side horseshoe vortex with the passage vortex. His secondary flow model is shown in Figure 1.1c. The following descriptions are based on rectilinear cascades, which in general may not be an accurate description of the flow in real turbine nozzles.

As described earlier, the horseshoe vortex develops at the leading edge of the blade, due to the interaction of the endwall boundary layer and the leading edge. According to Langston, the pressure side of the horseshoe vortex rolls up smoothly into

a)

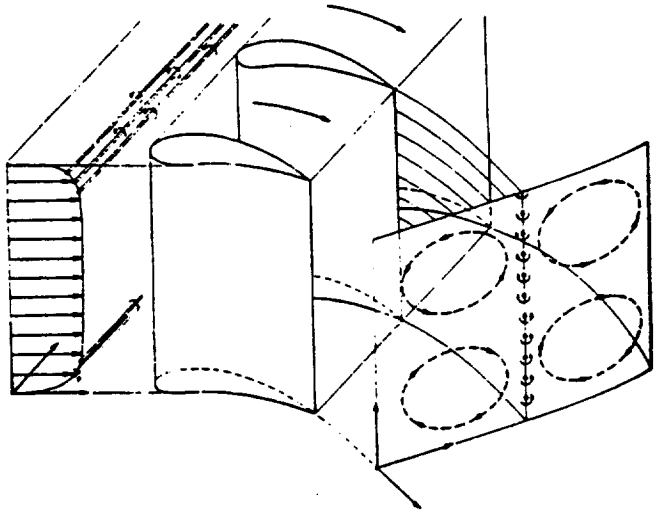

b)

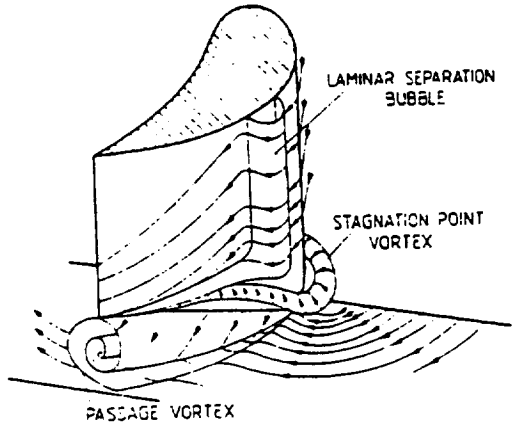

c)

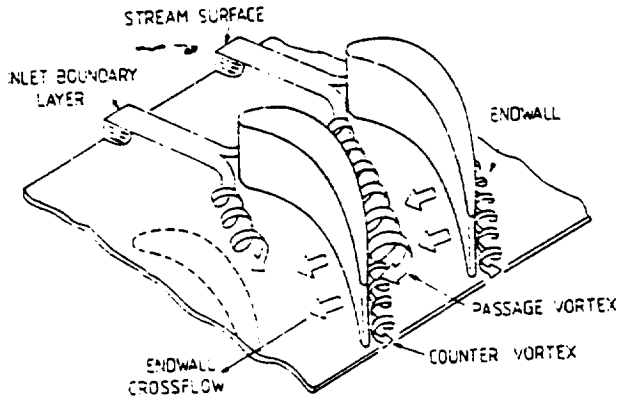

Figure 1. 1 Secondary Flow models by: a) Hawthorne(1955), b) Klein (1966) , c) Langston (1976).

the passage vortex. On the other hand, the suction side of the vortex wraps around the passage vortex, based on the flow visualization tests of Moore and Smith (1983). A review of various models, and the nature of the passage vortex and horse shoe vortex is given in Sieverding (1985). The development of the horseshoe vortex on the suction side is not well understood since measurements which utilize pressure probes near the leading edge and accelerating region are not able to detect the small vortex. In the region close to the trailing edge the horseshoe vortex has lost its intensity due to the influence of the passage vortex.

The corner vortex develops along the suction/endwall corner, and is typically very difficult to detect because of its small size. Evidence of the existence of the corner vortex is manifested in the overturning of the flow.

Along the endwall surfaces near the leading edge the flow field can be divided into distinct regions by the three dimensional separation line and the reattachment line, often called the stagnation streamline. The two lines meet at the saddle point located close to the leading edge of the blade. The horseshoe vortex develops behind the separation line starting from the saddle point, with the suction side following the blade surface and the pressure side migrating toward the suction side of the next blade.

The development of secondary flow is not very well understood in realistic blade configurations, compared to the previous description in rectilinear cascades. The influence of the appreciable radial pressure gradient, blade curvature, potential effect of downstream rotor and non-uniform inlet flow field have not been fully investigated and this is the

objective of the research reported here. In addition the influence of the secondary flow and downstream rotor on the redistribution of unsteadiness, boundary layer development, and interaction are also investigated.

1.1.2 Three Dimensional Boundary Layers

Three dimensional boundary layers arise in a variety of flow conditions such as swept wings, corner flows, wing body junctions, turbine blades, and rotating bodies. The pressure driven three dimensional boundary layers result from the presence of a pressure gradient in the transverse direction. The three dimensional boundary layers also arise due to the three dimensional shape of the surface, or due to the interaction of boundary layers. The three dimensional boundary layers in turbomachinery can be pressure driven along the surface of the blade and endwalls (Figure 1.2a) and arise due to the interaction of the boundary layers at the endwall-blade surface corners (see Figure 1.2b).

Most of the available research on three dimensional boundary layers has been performed on external configurations and rectilinear cascades. Very little work has been done to investigate boundary layer development in realistic configurations representative of modern jet engines. The following discussion will mainly concentrate on the endwall and blade boundary layers in axial turbomachinery and cascades.

One of the earliest measurements of three dimensional boundary layer development in a turbomachinery flow field was performed by Anand and Lakshminarayana (1978) on the rotor of a rocket pump inducer utilizing a rotating three sensor hot wire probe.

a)

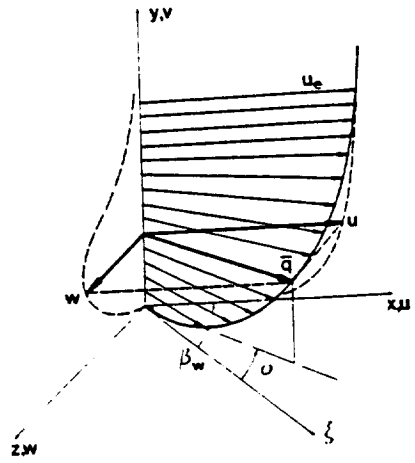

b)

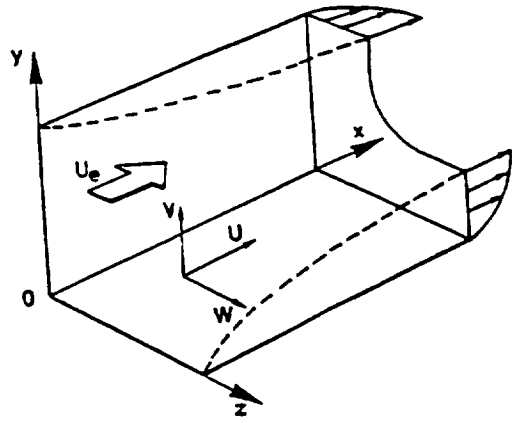

Figure 1. 2 Three dimensional boundary layers. a) Pressure driven boundary layer skew - blade surface; b) Boundary layer interaction - corner flow. Source Krause et al. (1982).

Significant outward radial velocity was observed inside the rotor blade boundary layers. The magnitude of the radial component was found to be strongly influenced by the chordwise velocity profiles. Bammert and Sandstede (1980) measured boundary layer profiles on smooth and rough surfaces of a turbine blade cascade with 60° turning using a miniature (0.25 mm diameter) pressure probe. Increased surface roughness increased the boundary layer thickness and induced earlier separation and transition. The boundary layer thickness increased uniformly along the suction surface, but on the pressure surface the boundary layer thickness started to decrease at x/c=0.5 due to the favorable pressure gradient. Velocity profiles inside the blade boundary layer were obtained by Lakshminarayana et al. (1982), using a miniature x-wire rotating probe, at five radial locations in the tip region of a compressor rotor blade. Later more detailed measurements by Pouagare, Galmes, and Lakshminarayana(1985) established that in the regions away from the endwalls, the boundary layers are mainly influenced by the pressure gradients in the radial direction. Very high three dimensionality was observed in the boundary layers in the tip region, where the tip leakage effect dominated.

Hodson (1983) observed that the periodic unsteadiness due to upstream nozzle on the rotor blade boundary layers influenced the transition and boundary layer development. This unsteadiness also contributed to the increase in the profile losses. The flow was found to be fully laminar along the pressure surface and the transition from laminar to turbulent flow occurred at 78% of the chord. A good review of boundary layer research in cascades is given in Deutsch and Zierke (1987).

Mee et al. (1992) performed detailed measurements on a transonic turbine cascade, using a miniature flattened Pitot tube with an opening of only 0.10 mm. The turning angle was 111 degrees and the inlet Mach number was 0.31. The measured velocity profiles indicate a thin unsteady separation bubble occurring on the suction surface close to the location where the favorable pressure gradient occurs.

1.1.3 Computation of Three Dimensional Boundary Layers

Accurate prediction of boundary layer development on turbomachinery blading is difficult due to the complex nature of the three dimensional flow field. This could be resolved using a Navier-Stoke code, but the solution would not be accurate due to limitations imposed by the grid spacing in the regions close to the surface of the blade. Simpler quasi-three dimensional and viscous methods can not resolve the highly three dimensional flow field. The boundary layer approach , where the free stream velocity or pressure is prescribed, is very efficient and accurate. This approach could predict the heat transfer, pressure losses and boundary layer growth in turbine passages. This approach has been developed by Lakshminarayana, et al. (1982), Anand and Lakshminarayana (1980) and Vatsa (1984).

The turbulent boundary layer growth is governed by two length scales which have different properties. In the near wall region, turbulence is influenced by the presence of the wall and the well known law of the wall is sufficient to describe the boundary layer profile. Far from the wall the turbulence is wake-like and an outer layer length scale governs the

turbulence quantities.

A three-dimensional boundary layer code was developed by Anderson(1985) utilizing the methods developed by Vatsa (1985). This method utilizes the Levy-Lees transformations modified for the body fitted coordinate system. For laminar two dimensional boundary layers, the Levy-Lees transformation, given by Blottner (1970) has shown to be very effective in capturing the boundary layer growth. The Levy-Lees transformation greatly simplifies the computation. Werle and Verdon(1980) have generalized these equations for turbulent boundary layers, by replacing the laminar viscosity by an effective turbulent coefficient creating a generalized turbulent version of the Levy-Lees transformations. Vatsa and Davis(1973) extended the Levy-Lees transformations to 3-D turbulent boundary layers which reduce to the two dimensional forms of Blottner and Werle.

Vatsa's (1984) procedure includes three separate analyses: (1) An analysis to construct a general non-orthogonal surface coordinate system for twisted turbine blading. (2) Calculation of the boundary layer edge conditions from a known static pressure distribution. (3) 3-D boundary layer analysis which predicts the boundary layer growth with prescribed edge conditions.

The solution of the boundary layer equations requires accurate specification of the edge conditions in the free stream. The required edge conditions are two components of velocity, total enthalpy (rhotalpy) and the thermodynamic properties (pressure and temperature). Typically the edge conditions are from experimental measurements or from

an Euler or panel solution of the flow field. One possible problem in using the Euler solution to determine the boundary layer growth is the inability of the solution to capture the secondary flow effects in the endwall region. A better approach is to use an Euler solution evaluated at the blade surface but based on experimentally determined pressure distribution.

The momentum integral approach has been used by Lakshminarayana et al (1982) to predict the three dimensional turbulent boundary layer development on a fan rotor blade and the predictions are compared with hot-wire data. The results were found to be in agreement with experimental data on the pressure surface and over most of the suction surface, except in the trailing edge region.

1.2 Objective of Research

The major objective of this research is to understand the characteristics of three dimensional boundary layers on nozzle vane, casing and hub endwall surfaces of an axial flow turbine nozzle passage. The objectives include the following:

- Investigation of the nature of nozzle vane passage boundary layer development, including transition, laminar and turbulent flow regions and variation of the boundary layer integral properties along the blade and endwall surfaces.

- Investigation of the interaction between the secondary flow regions and the three dimensional boundary layers in blade nozzle passage.

- Study the nature of unsteadiness in the nozzle vane passage and vane boundary layers due to potential effects of downstream rotor.

- Prediction of the turbulent and laminar boundary layer characteristics using a

three dimensional boundary layer technique and assessment of the ability of a boundary layer code to predict the viscous flow field accurately.

These investigations should lead to improvements in blade design, efficiency and cooling methods.

1.3 Method of Investigation

The applicability and limitations of the boundary layer procedure is investigated by comparing with the experimentally measured properties. The experimental methods used in the investigation include laser Doppler Velocimetry (LDV), hot wire, pneumatic pressure measurements, and flow visualization.

The flow field in the nozzle passage has been measured using a two-dimensional LDV technique allowing measurements of the velocity components and turbulent properties in an non-intrusive fashion. Static pressure measurements where obtained on blade surfaces and passage endwalls using pressure taps located at various locations along the blade passage. The results are used for the computation of the boundary layer development on the blade surfaces.

A two sensor, crossed, hot wire probe is used to obtain detailed boundary layer measurements in the blade and endwall regions. This technique enabled measurement of the steady and unsteady phenomenon in the nozzle blade passage, including boundary layers and secondary flow. Flow visualization of the transition and limiting streamlines is performed using an fluorescent oil technique.

The boundary layer development and characteristics were also investigated by performing a computational simulation using a three dimensional boundary layer code modified for the current application. The predicted boundary layer profiles, edge conditions, and losses are compared with the experimental data.

CHAPTER 2

EXPERIMENTAL FACILITY AND INSTRUMENTATION

The measurements reported here were performed inside the nozzle of the Axial Flow Turbine Research Facility (AFTRF) located in the Turbomachinery Laboratory of the Pennsylvania State University. The primary measurement techniques used to acquire the results are the Laser Doppler Velocimeter (LDV) and the hot wire anemometer. What follows is a brief description of the facility, measurement techniques and calibration procedures.

2.1 Experimental Facility

The axial flow turbine is an open circuit facility with an enclosure around the inlet made out of a thin, small cell foam, a large bell-mouth inlet section, stator and rotor test section, followed by two axial flow fans which provide the required pressure rise, and a outlet with an acoustic enclosure. The inlet, test section, rotating instrument section and the slip ring unit are shown in Figure 2.1. The installed blading is based on advanced GE design procedures and is representative of modern axial turbine blade design. The diameter of the facility is 91.4 cm, the hub to tip ratio is 0.73. The stator has 23 nozzle guide vanes followed by 29 rotor blades, with outlet guide vanes located 3 rotor chords down stream of the turbine stage. The variable flow rate is provided by two adjustable pitch, axial flow

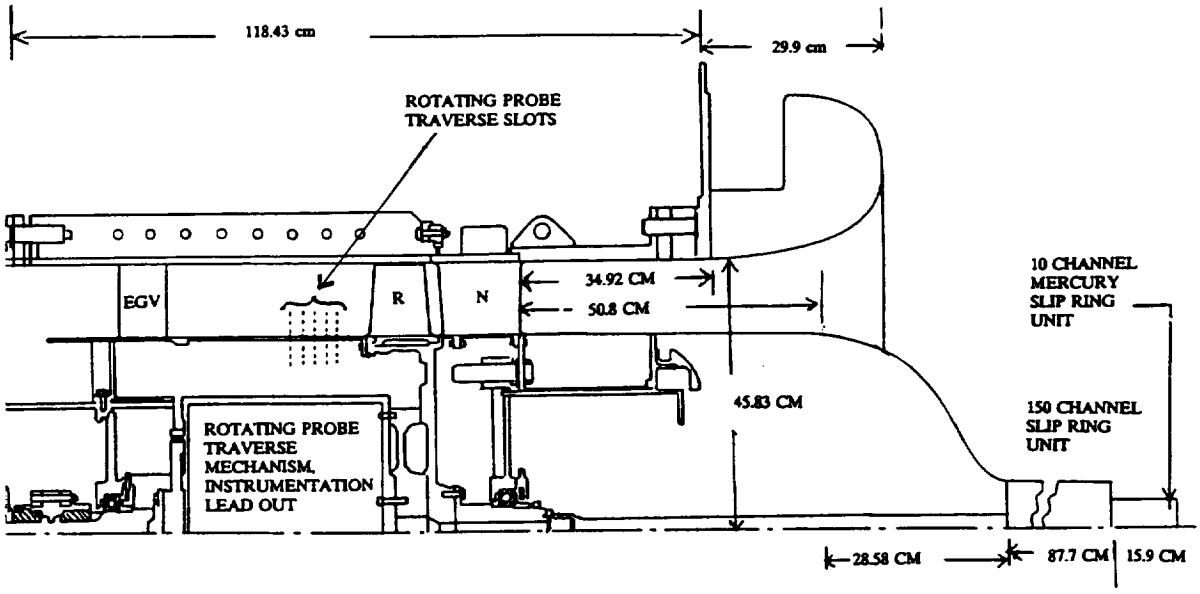

Figure 2. 1 Schematic of the Axial Flow Turbine Research Facility (AFTRF) inlet, test section, and rotating instrumentation.

fans and an aerodynamically designed throttle. This allows control of the mass flow through the turbine stage up to the maximum of 22 000 ft^3/min, with the fans providing a peak pressure rise of 74.7 mm Hg (40 in. water). The turbine rotor speed is continuously variable from 175 to 1695 RPM through the use of an electronically controlled eddy current brake that is capable of absorbing up to 90 Hp of rotor output. The speed is adjustable to ±1 RPM, with normal fluctuations of the line voltage.

The facility is equipped with a 150 channel slip ring unit, used to connect the rotating instrumentation and traversing mechanism to the stationary frame. Rotating anemometers, pressure transducers, amplifiers, and a probe traversing mechanism are all located inside a rotating instrument drum.

Data acquisition is accomplished using a 486 PC with 8 MB of RAM, and a Metrabyte DAS-20, 8 channel digital A/D sample card with a maximum sampling rate of 120 kHz. The card is used for data acquisition of the hot wire anemometer signal and measurement of steady pressure measurements. The board is also used for controlling a pressure stepping system (Scanivalve) to acquire the steady pressures through the use of software controlled 2 D/A channels. The LDV data is acquired using a dedicated data acquisition system (Dostek) allowing measurement of three LDV channels within a software specified coincidence window.

The performance parameters of the AFTRF have been reported by Lakshminarayana et al. (1992), and a summary of the design operating performance parameters is presented in Table 2.1. The parameters are based on a one dimensional mean line study at design point. The basic design features of the nozzle vane and rotor

Table 2. 1 Overall Performance Parameters of the AFTRF

Total Temperature at inlet (°K): T_0	289	Mass Flow rate (kg/s): W	11.05
Total Pressure at inlet(kPa): P_0	101.36	Pitchline Reaction: R	0.382
Specific work output (kJ/kg) : $\Delta h/W$	5.49	Pitchline Loading Coefficient: ψ	1.88
Flow Function: $W\sqrt{T}/P$ ($kg\sqrt{^0K}\ m^3/kN\ s$)	1.85	Hub Loading Coefficient: ψ	2.63
Speed Function: $N\sqrt{T}$ ($RPM/\sqrt{^0K}$)	77.69	Stator Zweifel Coefficient:	0.725
Rotational Speed: N (RPM)	1300	Rotor Zweifel Coefficient:	0.976
Total Pressure Ratio: P_{01}/P_{03}	1.0778	Power: (kW)	60.6
Total Temperature Ratio: T_{03}/T_{01}	0.981	Stator Efficiency: η_{stat}	0.99421
Pressure Drop: P_{03}-P_{01} (mmHg.)	56.04	Rotor Efficiency: η_{rot}	0.8815
Hub Reaction: R	0.181	Total to Total Isentropic Efficiency: η_{TT}	0.8930

Table 2. 2 Turbine Stage and Blading Features

Hub to Tip Ratio:	0.7269	Vane (Inlet Velocity) Re:	(3~4) x 10^5
Tip Radius:	0.4582 m	Blade (Inlet Velocity) Re:	(3~5) x 10^5
Blade Height:	0.1229 m	Ave. Tip Clearance:	0.97 mm
Nozzle - Number of Blades:	23	Rotor - Number of Blades:	29
- Chord :	0.1768 m	- Chord :	0.1287 m
- Spacing :	0.1308 m	- Spacing :	0.1028 m
- Max. Thickness :	38.81 mm	- Max. Thickness :	22.0 mm
- Turning Angle :	70 °	- Turning Angle :	95°tip,126° hub

blading are presented in Table 2.2 based on the design requirements. One of the unique capabilities of the facility design are provisions for variation of the nozzle-rotor spacing from 20% to 50% nozzle vane chord. In the present research program, the mid blade spacing is 20% of the nozzle vane chord.

All measurements in the current investigation were performed at a corrected RPM of 1300, constant mass flow rate ($\dot{m}$) of 10.53 kg/s, and pressure ratio (P_{01}/P_{03}) of 1.078. The throttle setting is kept at a fixed position throughout the experiments.

2.2 Hot Wire Anemometer Measurement Technique

Hot wire anemometry, in use since the late 1800's, has emerged as a powerful technique for measurement of unsteady flow velocities. In the current experiment a two sensor hot wire probe was used to determine the unsteady velocity components in two directions simultaneously. Calibration of the probe was accomplished using a modified high speed, temperature controlled, low turbulence TSI 1155 calibration jet. Modifications included installation of a termocouple measuring total temperature, pitch and yaw automated traverses, nozzles of varying exit diameter, and a heating element. The probes used were straight TSI 1247 and 90° bend TSI 1250A probes. These are connected to a AA Labs AN-1003 six channel hot-wire/hot-film anemometer. The average spacing between the sensors measured, using a precision optical measurement system, was found

to be 0.203±0.005 mm. The wire length (l) was 2.45 mm., with the sensor being a 5 μm. Tungsten wire. A schematic of the probe is given in Figure 2.2. The probe was mounted on a precision traverse system which allowed motion in the tangential direction at 1/32° intervals of the circumferential direction, and 0.1 mm in the radial direction.

The probe was calibrated for flow velocity, angularity, temperature and wall effects.

2.2.1 Calibration of Two Sensor Hot Wire

The classical formulation for determining the effective velocity as a function of the bridge output voltage is King's (1914) law expressed as:

$$E = A + B \cdot V_e^n \tag{2.1}$$

The output voltage E is recorded for a variety of known flow effective velocities U_{eff}, and the calibration constants A and B are determined using least squares fit to smooth out the irregularities in the calibration. The log slope n, is assumed constant for low Reynolds numbers and typically taken to have a value of 0.45. Although this procedure has the benefits of ease in implementation and the ability to slightly extend the range of usability, due to the use of computer processing of the measured data greater accuracy can be achieved by using a higher order polynomial function curve fit which can be written in the following form:

$$V_e = \sum_{n=0}^{k} A_n \cdot E^n \tag{2.2}$$

The benefits of using this approach are incorporation of compressibility effects for higher

velocity measurements, accurate behavior at both high and low velocities, and computational simplicity. In Figure 2.3a, the calibration of a two sensor probe with the polynomial curve fit superimposed on the actual measured points is shown. The calibration is performed keeping a constant temperature in the flow field, and the probe is aligned at 90° with respect to the direction of the flow. The angular sensitivity of the probe is evaluated by rotating the probe at constant jet velocity and recording the output voltages for various angles of rotation. The probe coordinate system is shown if Figure 2.2.

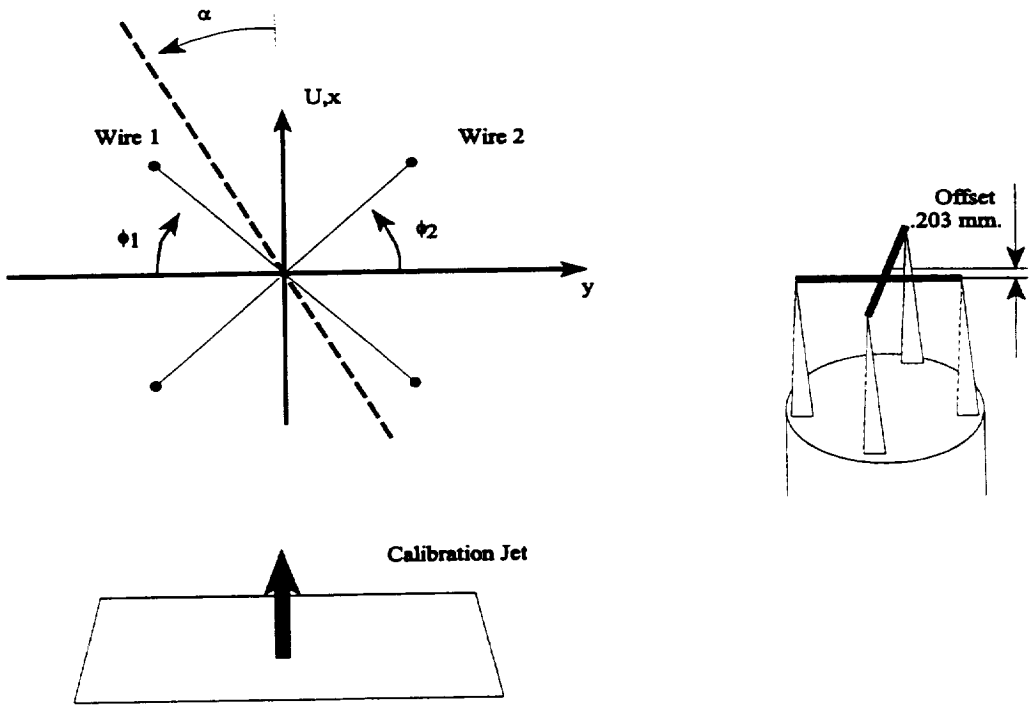

Figure 2. 2 Angular calibration of two sensor hot wire and probe layout.

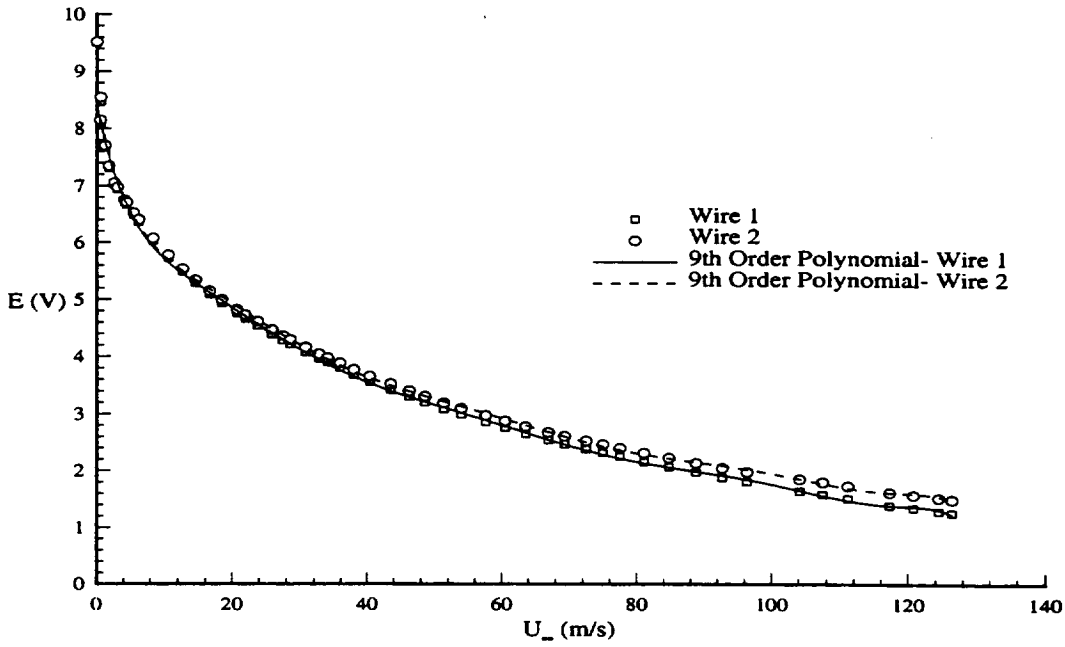

a)

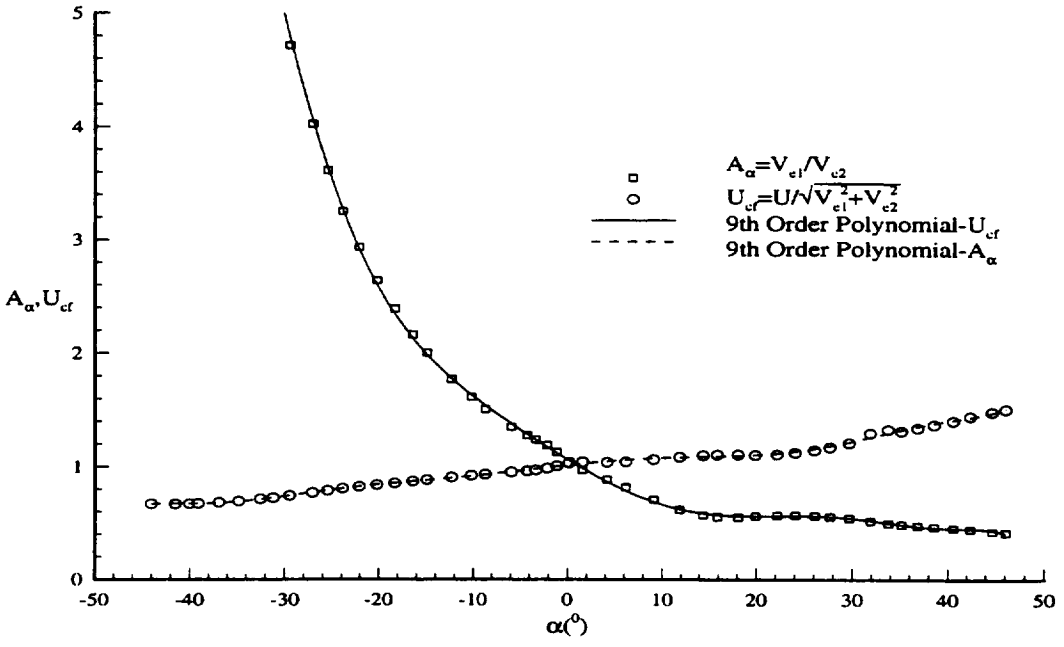

b)

Figure 2. 3 Hot Wire Calibration. a) Effective Velocity, b) Angular Calibration.

Determination of the effective velocity is accomplished using the yaw angle relationship Hinze (1959), which in this case can be written as:

$$V_{e_1} = U^2(\cos^2\phi_1 + k_1^2 \sin^2\phi_1)$$
$$V_{e_2} = U^2(\cos^2\phi_2 + k_2^2 \sin^2\phi_2) \qquad (2.3)$$

The sensor angles ϕ_1 and ϕ_2, are measured using an optical protractor and an 20 X microscope with an accuracy of 0.5°. The coefficients, k_1 and k_2 are determined experimentally to be close to 0.109 for the l/d ratio of 490, which is close to the value suggested by Lomas (1986).

The angular calibration of the cross wire sensor is performed using the following method developed by Blanco et al. (1993). The angular coefficient A_α, and velocity coefficient U_{cf} are defined as:

$$A_\alpha = \frac{V_{e_1}}{V_{e_2}} \qquad U_{cf} = \frac{U}{\sqrt{V^2_{e_1} + V^2_{e_2}}} \qquad (2.4)$$

The coefficients are calculated for each individual rotation angle α in the range of ±45°, shown in Figure 2.3b and are assumed to be only functions of a α for a constant calibration velocity. From the resulting data, a higher order polynomial curve fit of the coefficients is obtained. The evaluation of the measured velocity is therefore accomplished by the determination of the angular coefficient $A_\alpha = V_{e1}/V_{e2}$. From the coefficients of the curve fit $A_\alpha = A_\alpha(\alpha)$, we can now obtain the probe rotation angle α and consequently the velocity calibration coefficient U_{cf}. The magnitude of velocity can then be determined by using $V = U_{cf}\sqrt{V_{e1}^2 + V_{e2}^2}$. One of the advantages of this method is that

the influence of the probe supports on the measurement is taken into account in the calibration. From Figure 2.3b it is apparent that the probe support effects are not symmetrical for positive and negative rotation angles.

Determination of the temperature effect on the measured bridge voltage output is critical for hot wire measurements taken at significantly different ambient conditions than calibration conditions. Due to the nature of the AFTRF (open circuit facility), the flow temperature varied during the measurement, in some cases by as much as 10 °C from the initial temperature.

Radeztsky et al. (1993) developed a technique for compensating for the voltage drift due to the temperature fluctuations. For a constant flow velocity, the bridge output voltage is a linear function of the temperature. The calibration procedure developed here involves measurements of the output voltage of individual sensors for a fixed jet velocity over a range of temperatures (see Figure 2.4a). The slope of the linear variation of the output voltage (dE/dT), for a constant flow velocity, can be determined from the measurement. This can then be used to correct the measured voltage for temperature variation. A typical calibration curve for the temperature fluctuation slope as a function of jet velocity is shown in Figure 2.4b. Since the slope of the temperature variation is a function of the velocity, the correction has to be applied iteratively. An initial guess of the total velocity is used to determine the value of dE/dT and a correction to the output voltage is computed. The new value of total velocity based on the corrected voltage is compared to the initial guess and the process is repeated until the velocity converged to an

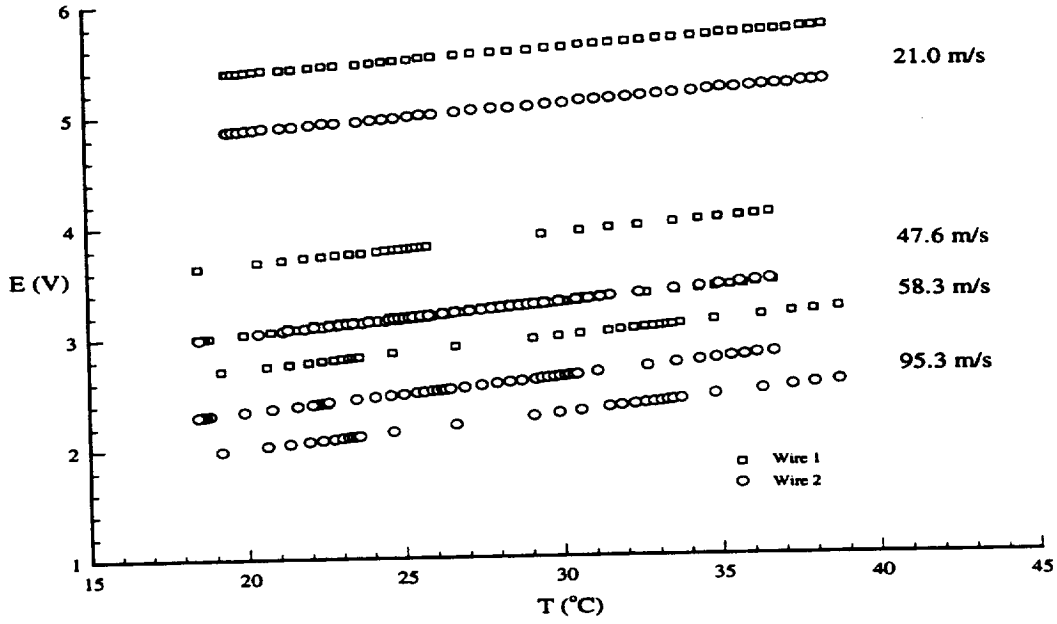

a)

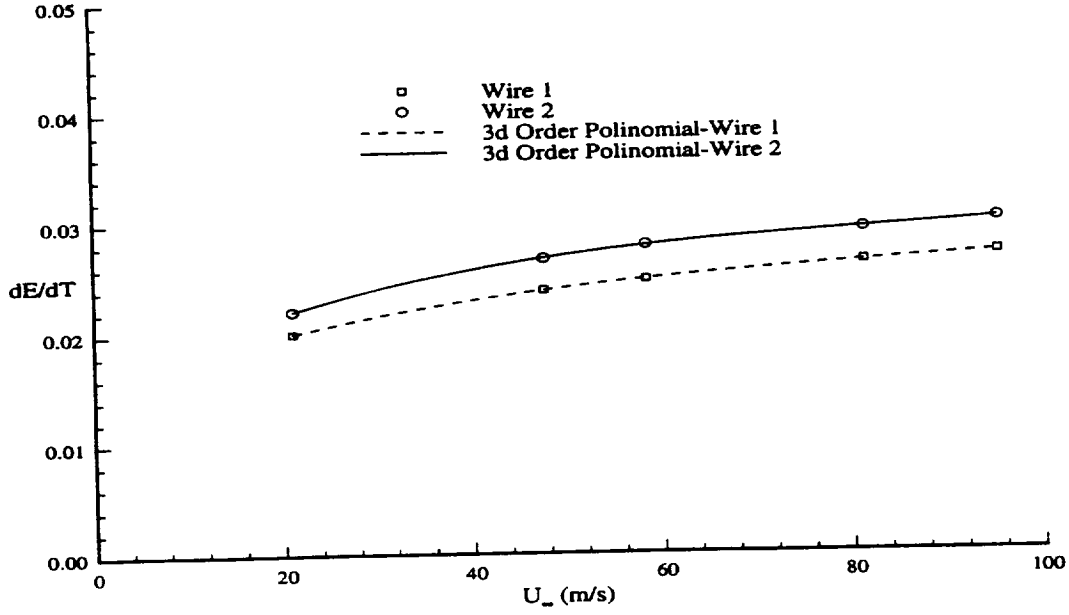

b)

Figure 2. 4 Hot wire temperature correction. a) Constant velocity variation, b) Temperature gradient variation.

unique value. Usually only a 4 to 5 iterations were required for a convergence criterion of 0.1 m/s.

Additional complexity of hot-wire measurements in the close proximity of an wall is the increase of heat transfer from the sensor to the surface. The near wall effect was observed by Dryden(1936), for typical sensors, to be appreciable at distances of 0.9 to 1.5 mm. from the wall. Oka and Kostic (1972) found out that the near wall effect was also a function of surface material and reflectivity(due to thermal radiation). The effect can be quite large in the near wall region. The present approach was to perform a near wall calibration using a flat plate machined to the same surface roughness and of the same material as the turbine nozzle blading. The hot-wire probe was traversed perpendicular to the surface of the of the plate for various velocities. At the same location on the flat plate with the same flow conditions, a 0.022 in. diameter total pressure probe was traversed and the resulting velocity profile measured. The deviation of the pressure probe measurement from the hot wire is shown in Figure 2.5a (V_{xw} -hot wire probe measured total velocity, V_m -total pressure probe measured total velocity) . The effect was localized only in the near wall region with $d/l_{ref} < 0.4$ (l_{ref} is the wire length, i.e. 2.45 mm., d is the distance from the wall surface), while the measurements outside of this region where not affected. Due to the offset of the individual sensors, a greater influence was observed in wire 1 which is 0.2 mm. closer to the surface. This translated into measurement of a erroneous angle in the near wall region, even through the actual flow direction did not change. The effect of the flow angle deviation is shown in Figure 2.5b (α_{xw} -measured

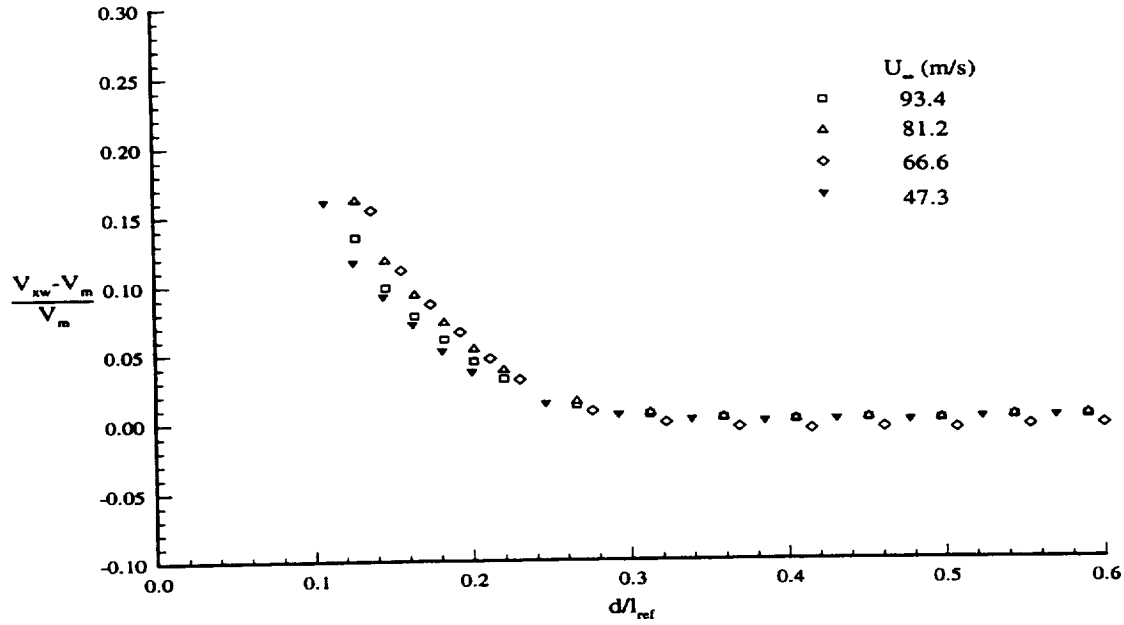

a)

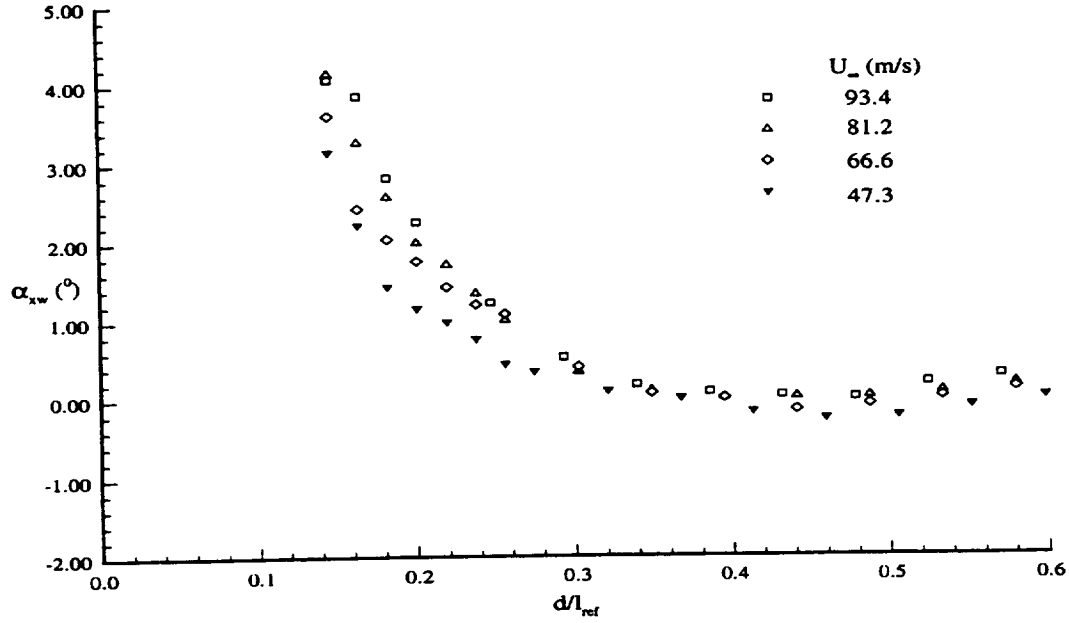

b)

Figure 2. 5 Near wall hot-wire probe correction. a) Total velocity error (V_{xw} - x-wire measurement, V_m - total (pitot) probe measurement), b) Angular correction (α_{xw} - x-wire angular error).

angle by x-wire probe). The deviations in the near wall region indicate that the angular error increases close to the wall due to the additional heat transfer from the closer wire for higher free stream velocities. Away from the very near wall region ($d/l_{ref}>0.3$) the deviations appear to be independent of the free stream velocity, even though the heat transfer is a function of the local Re. The reason is that for the flat plate measurements the boundary layer thickness was too small. The velocity gradients in the measurement region are essentially zero. In the near wall region the heat transfer is mostly radiative and not convective in nature for the very thin boundary layers.

The data processing flow chart for implementation of all the corrections to the hot-wire signal are shown in Figure 2.6. The increase in processing time required to evaluate the signal could be substantial, especially for large sampling data sets. The wall correction is applied only in the region close to the passage surface.

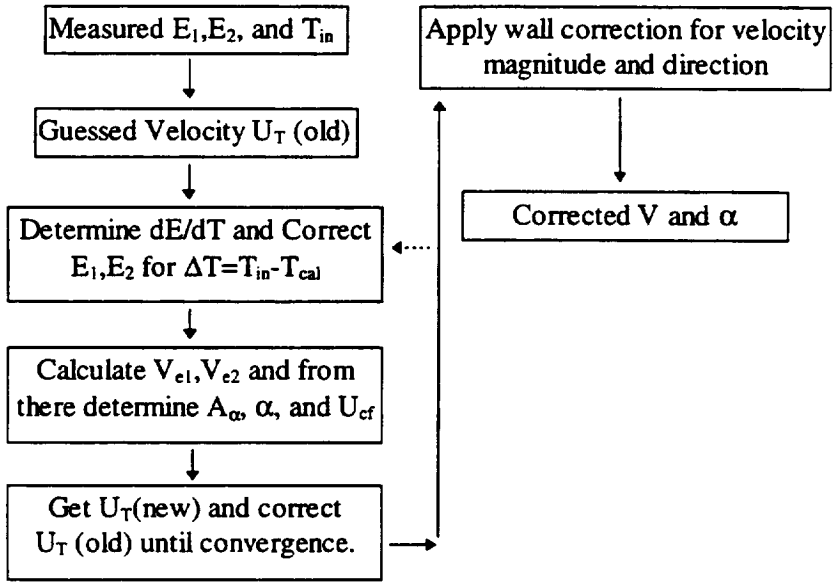

Figure 2. 6 Hot wire signal processing flow chart.

2.2.2 Hot-wire measurement errors

An error analysis of the hot wire measurements, for both steady and turbulent properties, is given in Appendix B. Sources for the errors are: calibration errors, spacing of sensors, positioning accuracy, wire aging, etc. Based on this analysis, the steady velocity measurement is about ± 0.9 % accurate in the boundary layer region. Outside of this region where the zero normal velocity assumption is inaccurate, the error is larger. The maximum error in angle measurements is about 1.2°.

2.3 Static Pressure Measurements

The AFTRF is instrumented with nearly 500 static pressure measurement taps located at a variety of locations in both the stationary and rotating frames. This includes static pressure taps distributed along the circumference of the hub and casing surfaces at 4 axial stations both upstream and downstream of the test section which is used in performance measurements. In the stationary frame, one nozzle vane passage is fully instrumented at 154 locations along the suction and pressure surface of the blade at several axial and radial stations. In the same blade passage 43 pressure taps are located on both endwall surfaces. Similar provisions are made for measurements in one of the rotor blade passages. Due to the long length of the tubing, a 15 sec. time interval was used between measurements, with the averaging time for each measurement being also equal to 15 sec. The pressures are measured sequentially using a stepping system and a single

calibrated (Δp=5 psi.) pressure transducer. Ambient pressures are monitored using an Oakton barometer (accuracy of 0.1 in Hg) every hour of operation time.

2.4 LDV Measurement Technique

The technique is based on the measurement of components of velocity of small (1 μm) particles following the flow through an accurately focused laser beam probe volume. The particle passing the laser beam interference pattern in the probe volume reflects light toward the collection optics at a frequency proportional to the fringe spacing and the particle velocity. The collected light is converted to an electrical signal using a photomultiplier. After signal processing the frequency of the burst is determined using analog processing circuits. By focusing additional laser beams of different wavelengths through the same probe (volume) position the velocity can be measured in other directions.

In the current investigation, a two component TSI LDV measurement system was used allowing simultaneous measurements of velocity components in two directions. The system compromises of a 7W Ion-Argon laser operating in multi-wavelength mode. The laser beam is split using a prism into a blue (488 nm.) and green (514.5) component. These are again split into two equal intensity beams using a system of prisms. The optical system focuses the four beams to a probe volume using a 3.75X expander and a 300 mm focal length lens, through the same optical path. The probe volume dimension are 64 μm across and 740 μm in length. Alignment of the beams is accomplished using an 50 μm

pinhole and individually adjusting the beams for equal intensity interference patterns on a projection screen. The beam half angle is determined by the focusing optics to be 4.95°. The whole optics and laser system is mounted on an optical isolation table designed to minimize temperature induced deformation of the 6 by 10 foot surface and provide vibration damping. The table can be traversed in three directions relative to the test section and rotated about one axis for accurate positioning of the probe volume.

The beam is focused through a 0.125 in. curved Plexiglas window in the nozzle passage, and a flat low distortion 0.125 in. window in the rotor. Since the beams are aligned using a window of the same optical dimensions and properties, the distortion of the beams is minimized. Fine tuning of the alignment is accomplished using the Bragg cell, by frequency shifting of one of the individual color beams. If the probe volume is positioned at a stationary surface the returning signal is equal to the frequency shift of the Bragg cell. The signal is optimized for maximum signal to noise ratio by carefully focusing the transmitting and receiving optics. The surfaces of the test section were painted using a heat resistant flat black paint to decrease reflections from the polished aluminum blades. The measurement plane was tilted by 7.5° from the tangential direction to eliminate direct reflections of the laser beams from the test section window on to the receiving optics.

The seed particles required for the measurement in the nozzle passage were introduced using a six jet atomizer (TSI) far upstream of the measurement location. The atomized mineral oil has an aerodynamic mean diameter of 1 μm (TSI, 1987). The atomizer produced sufficient data rates (≈ 200 per sec.) in the nozzle passage, but proved

to be insufficient in the rotor measurements. A fog machine (commercially available smoke generator manufactured by Rosco) produced a greater quantity of seed particles and decreased the amount of fluid depositing on the window compared to the mineral oil technique, with mean aerodynamic diameter of 1.1 to 1.9 μm (Wiedner, 1988).

The measurements in the rotor were tagged to the angular position of the rotor by using a shaft encoder with a once per and a 6000 per revolution electrical pulse. The data acquired over a number of revolutions of the rotor is stored along with the angular position for post processing.

2.5 Flow Visualization

To determine the limiting streamlines and regions of laminar, transitional, and turbulent flow on the nozzle passage blade and endwall surfaces, a fluorescent oil technique was applied. A thin layer of oil remains for a longer period of time on the surface in regions of low shear stress (i.e. laminar and transition) , and is wiped away faster in regions of high shear stress.

With the addition of fluorescent compounds, the aviation oil would emit light after exposure to ultraviolet (black light fluorescent tubes) radiation. A thin layer of oil was applied using an atomizer to prevent formation of streaks and droplets before the experiment. After a short run (5-10 min.) the oil patterns were photographed using standard color film, full aperture opening and an exposure of 30 sec.

CHAPTER 3

THREE-DIMENSIONAL FLOW FIELD MEASUREMENTS IN THE NOZZLE

Measurements in AFTRF were carried out to provide a basis for the investigation of the three-dimensional boundary layer development in the nozzle blade passage. This investigation included: the general flow field characteristics in the blade passage, the upstream and downstream conditions, blade and endwall static pressure distribution and blade passage surface flow visualization. In addition, information was gathered to aid in the boundary layer computation in the nozzle passage by determining the transition locations.

To achieve this goal, a variety of experimental techniques were utilized. The static pressure distribution along the passage surface was measured using static pressure taps located along the surface of the blade. The velocity components and turbulent properties near midchord (x/c_m=0.56) where measured using a two component LDV system. Fluorescent oil flow visualization was performed along the surface of the blade passage to investigate the nature of the boundary layers and the location of the transition.

3.1 Nozzle Vane Passage Static Pressure Measurements

The static pressure contours along the nozzle vane blade surface are presented in Figure 3.1a and 3.1b., where C_P is defined based on the upstream axial velocity (V_{x1}), p -

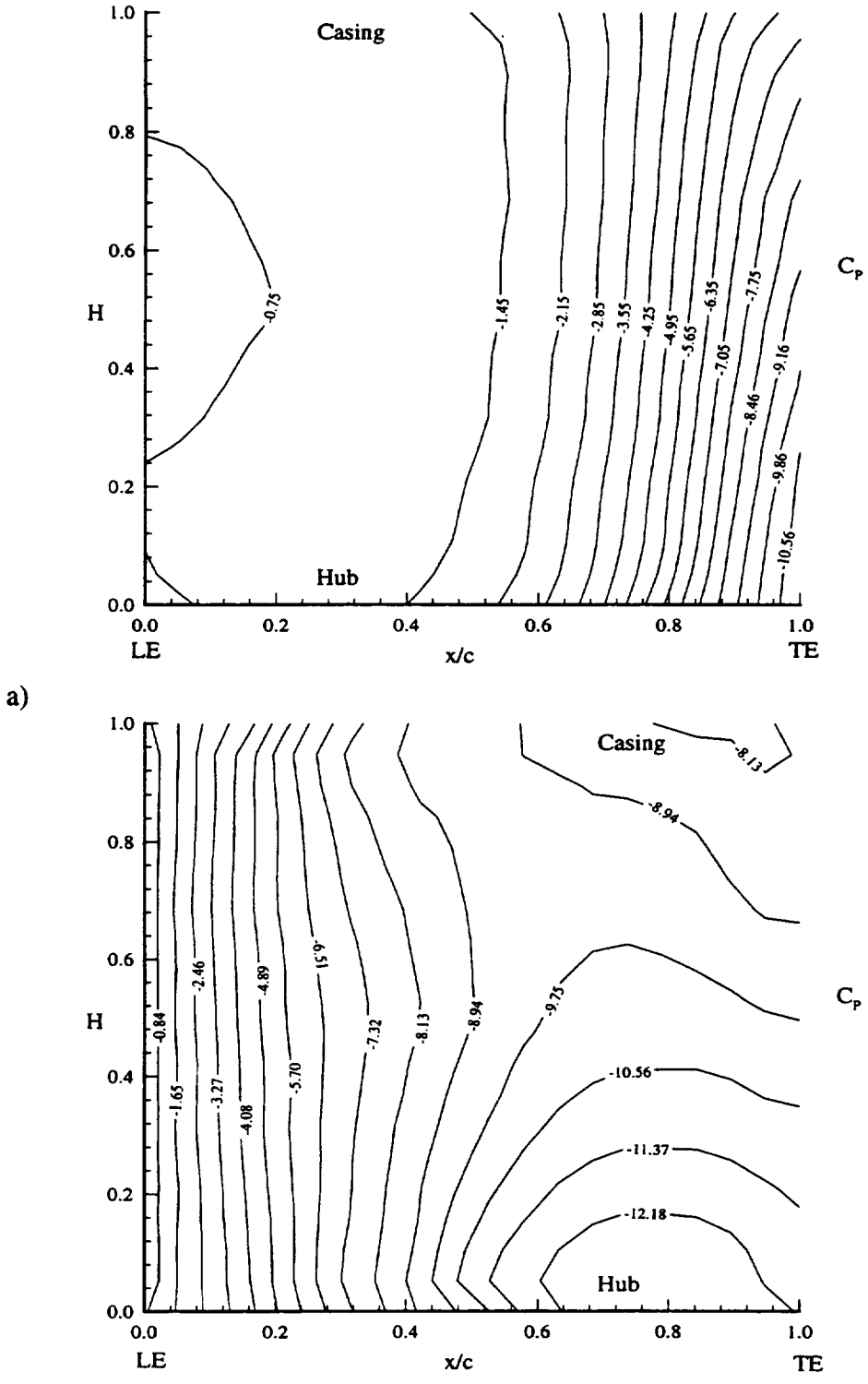

a)

b)

Figure 3. 1 Measured static pressure (C_P) contours on the nozzle blade surface. a) Pressure surface measurements, b) Suction surface measurements.

local static pressure, stagnation pressure (P_{01}), and density (ρ) as:

$$C_P = \frac{p - P_{01}}{\frac{1}{2}\rho V_{x1}^2} \tag{3.1}$$

The upstream axial velocity (V_{x1}) and stagnation pressure (P_{01}) are measured one chord upstream of the leading edge of the nozzle blade. The pressure varies uniformly along the pressure surface. The only appreciable three dimensional effect is evident from the radial pressure gradient near the trailing edge. The variation is small and mainly due to the inviscid effects.

Along the suction surface, larger influence of the secondary flow is apparent through the radial pressure gradient beyond about x/c=0.4. The decrease in static pressures in the hub region is much grater than the decrease in the tip region. The nozzle vane static pressure was computed using a panel method (McFarland, 1981) and a quasi-three dimensional method (Katsanis, 1977) and they are shown in Figure 3.2. The predictions proved to be fairly accurate along the pressure surface, and the quasi-three dimensional prediction proved to be fairly accurate in the hub region (H=0.10 and 0.30) indicating that the pressure distribution in the hub region is mostly due to the inviscid effects. At H=0.10 the panel method greatly under predicted the pressure drop in the trailing edge region (x/c=0.4 to 1.0) compared to the quasi-three dimensional method. In the tip (H=0.0) region both prediction methods proved to be inaccurate due to the existence of a strong secondary flow region (H=0.9 location). At H=0.9 the panel method predicted the static pressure drop accurately up to the minimum pressure location at x/c=0.40, beyond which the panel code over predicted the pressure drop. At mid span

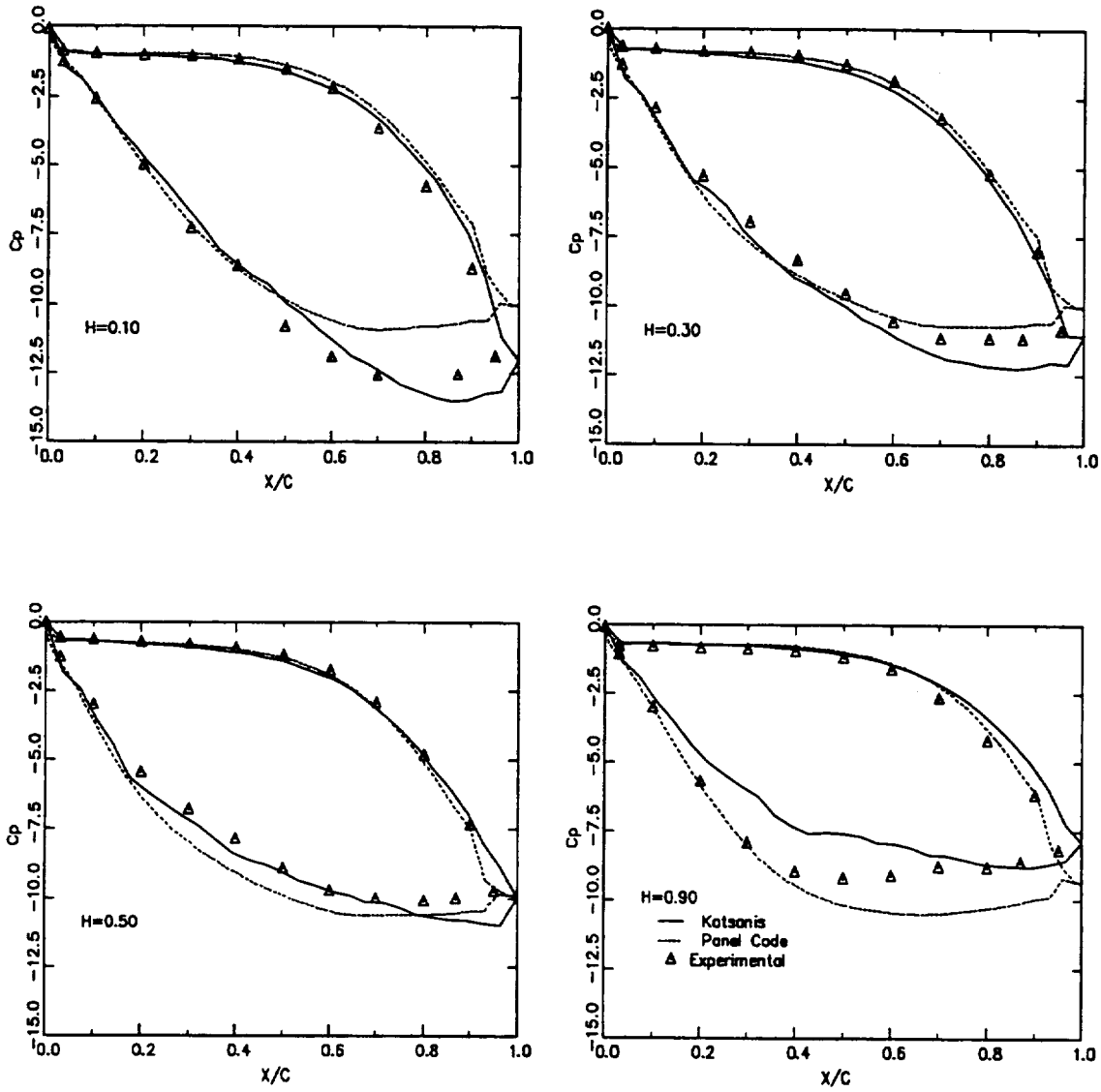

Figure 3. 2 Comparison of the Cp distribution along blade surface between measured and predicted for Katsanis(1977) and Panel Code (McFarland, 1981).

both methods proved to be equally accurate. The static pressure distribution was also measured along the hub and casing endwall surfaces and is shown in Figure 3.3. The cross flow or transverse pressure gradient is apparent along most of the hub and casing surfaces and dominates the flow field. This gives an indication of a very strong three dimensional flow along these surfaces. Along the pressure surface of the blade (S=1.0) the variation is uniform and smoothly decreasing from leading to trailing edge. The pressure field in the hub region seems to be more uniform than that observed along the casing. The minimum pressure locations occur close to the suction surface on both the casing and hub endwalls. On the casing surface, the minimum pressure occurs at x/c=0.50 indicating the region where the passage vortex detaches from the endwall surface and moves into the passage. Along the hub surface the minimum pressure location occurs farther downstream at x/c=0.81. This location indicates the motion of the hub passage vortex toward the blade surface. The location occurs much farther downstream compared to the one observed on the casing surface. This indicates that the hub passage vortex remains closer to the hub surface than the casing vortex, which is transported further inward along the passage.

The general characteristics of the nozzle passage surface pressure distributions are explained by the flow visualization experiments presented later in this chapter. The general conclusions regarding the development of the three dimensional boundary layers based on the measured pressure distribution are:

(1) The boundary layers along the pressure surface of the nozzle vane are mainly two dimensional and are weakly influenced by the radial pressure gradient. The secondary

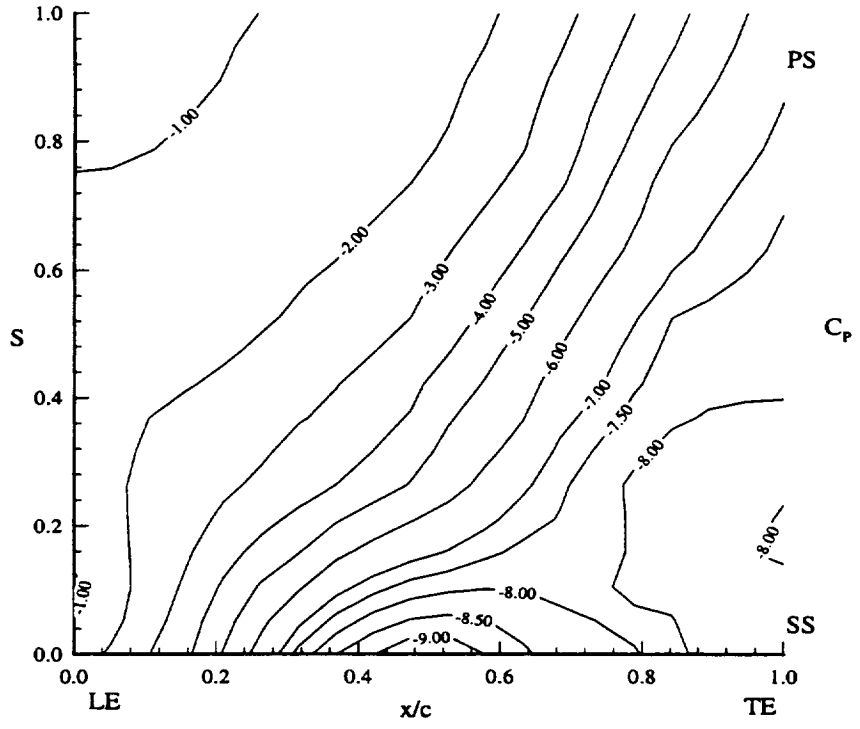

a)

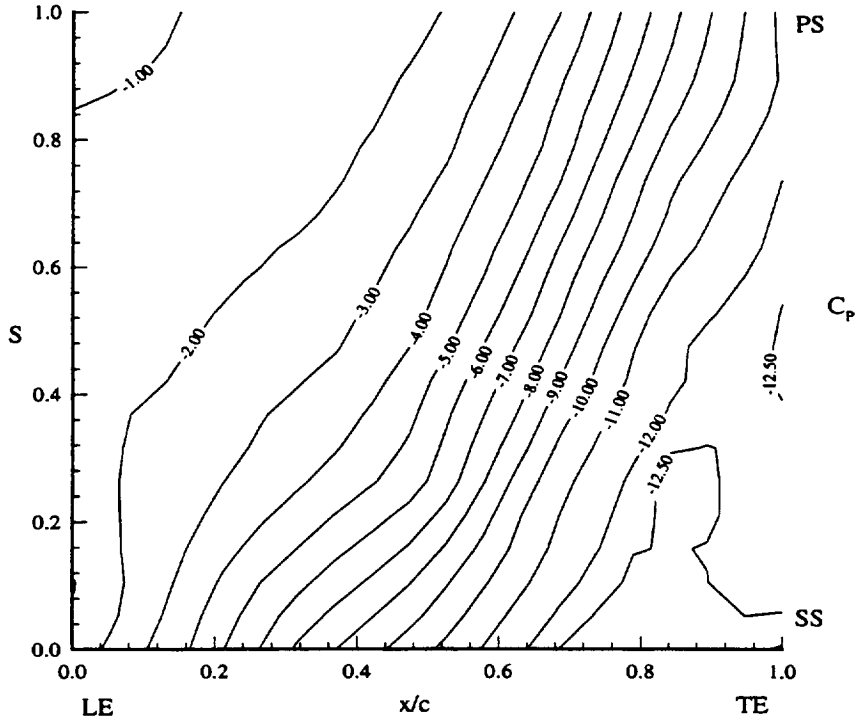

b)

Figure 3. 3 Measured static pressure (C_P) contours along the endwall surfaces. a) Casing surface measurements, b) Hub Surface measurements.

flow region is localized in the endwall regions.

(2) On the suction surface, the flow is accelerating rapidly up to approximately x/c=0.45. The boundary layers in this region are mainly two dimensional and thin. Down stream of this location the three dimensionality increases greatly, especially in the casing suction corner due to the presence of the passage vortex.

(3) The hub wall boundary layer is much thinner than the casing boundary layer due to the presence of a favorable pressure gradient over a larger region than the casing surface. The flow is still strongly three dimensional because of the cross flow pressure gradient.

(4) Along the casing surface, the detachment of the suction side of the passage vortex occurs much earlier than on the hub surface (H=0.5 compared to H=0.81). The three dimensionality is stronger especially in the trailing edge region.

3.2 Nozzle Passage Midchord LDV Measurements (x/c=0.56)

Measurements in the nozzle passage were performed at x/c_m=0.56 (based on the chord length at H=0.50) using a two component LDV system. The axial and tangential components of velocity and the corresponding individual turbulent intensities were acquired simultaneously. Since the axial chord is a function of the radius, the measurements do not correspond with a constant x/c, but with a constant axial distance x. The measurement location is at x/c_m=0.56 based on the chord length at midspan (c_m). The actual measurements are located ranging from x/c=0.615 at the hub to x/c=0.510 at the

tip.

The accuracy of the LDV measurement was validated by traversing a five hole probe at H=0.50 and comparing the results with the LDV measurements shown in Figure 3.4. The errors are within the accuracy band of the measurements and to a large extend were due to difficulties in accurate positioning of the table in the tangential direction. The measured mean total velocity (V) is defined as:

$$V = \sqrt{V_x^2 + V_\theta^2} \qquad V_{x_i} = V_x + v_x' \qquad V_{\theta_i} = V_\theta + v_\theta' \tag{3.2}$$

where subscript $_i$ signifies the measured instantaneous velocity and ' is the velocity fluctuation.

The results of the LDV investigation are shown in Figures 3.5, 3.6, and 3.7. The measured velocity is non-dimensionalized by the blade speed at midspan (U_m). In Figure 3.5a, the measured axial velocity distribution exhibits typical inviscid behavior for a turbine nozzle passage. The blank spaces shown outside the indicated measurement boundary could not be reached as they were located in the laser shadow region. Additional problems were encountered in the boundary layer regions, since sufficient seeding rates could not be sustained in this region. The endwall boundary layers are thin and the secondary flow is not strong enough to be clearly recognized. The contours of the tangential component of velocity (V_θ/U_m) are shown in Figure 3.5b. Close to the suction surface, from H=0.1 to H=0.4, the presence of the suction surface boundary layer can be clearly seen.

The measured yaw angle (α) shown in Figure 3.6a reveals a uniform distribution and is close to the design value of 40° over a the central region of the blade passage. The

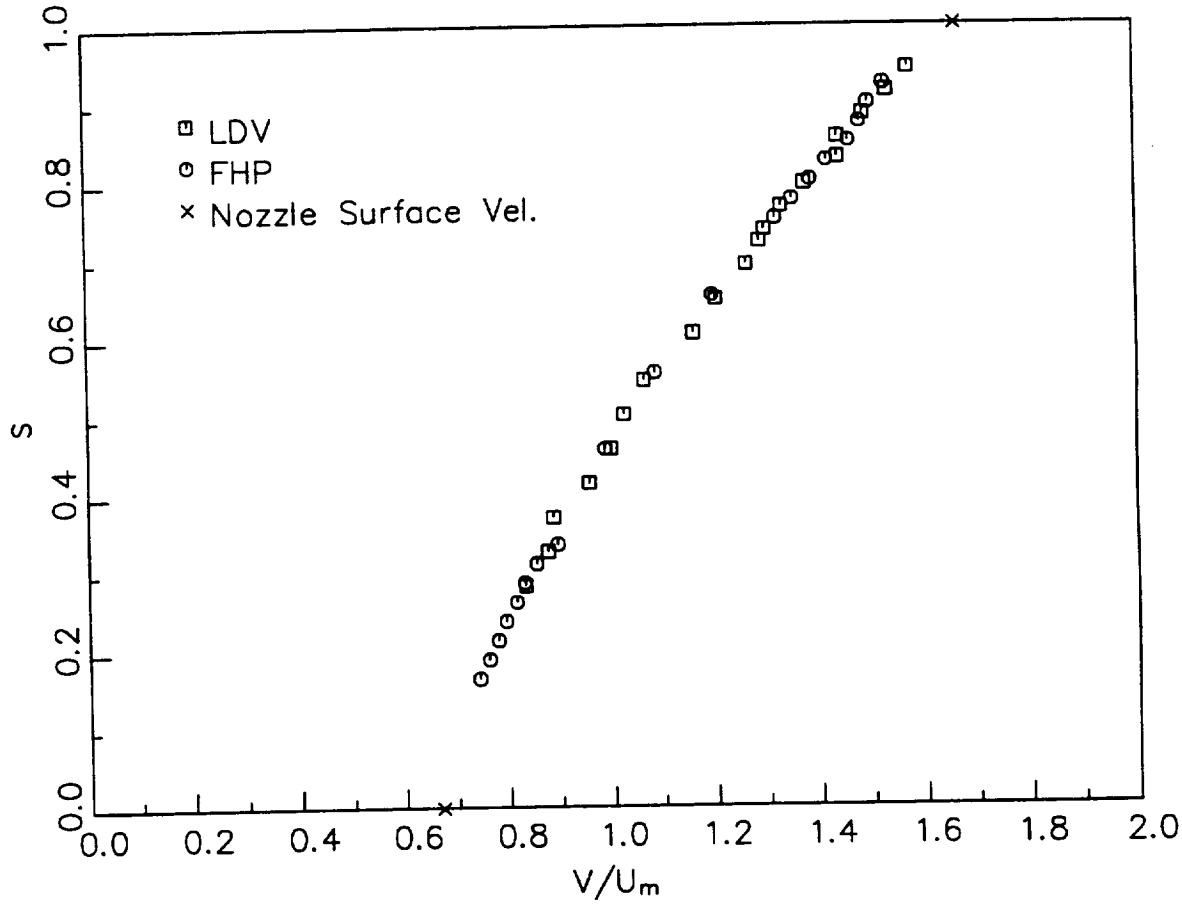

Figure 3. 4 Comparison of LDV and Five Hole Probe at x/c=0.56. Midspan location.

flow turning is higher near the suction surface than near the pressure surface. The region of over turning occurs in the casing boundary layer region (extending from S=0.3 to S=0.8 along the casing endwall surface). Under turning (α=27°) occurs in the casing-suction corner (approximately at S=0.20 and H=0.92). This is an indication that the inception of secondary flow has occurred even through the secondary flows are weak. The underturning region represents the bottom part of the secondary flow region. The over turning associated with the vortex is too weak to be measured at this location.

Measured total turbulence intensity (Tu) is shown in Figure 3.6b is defined as:

$$Tu = \frac{\sqrt{\overline{v_x'^2} + \overline{v_\theta'^2}}}{V} \cdot 100\% \tag{3.3}$$

The turbulent intensities are higher in the secondary flow region close to the casing endwall surface corresponding to the region of high under turning in Figure 3.6a. The turbulent intensity in the free stream is about 2%. The maximum measured value is 9.5 % in the casing boundary layer near the pressure surface. The turbulence intensity distribution in the blade passage indicates that the boundary layer on the hub is much thinner than that is in the casing endwall boundary layer.

The turbulence intensity in the axial (Tu_x) and tangential (Tu_θ) direction are shown in Figure 3.7a and 3.7b respectfully. The components of turbulence are defined as:

$$Tu_x = \frac{\sqrt{\overline{v_x'^2}}}{V} \cdot 100\% \qquad Tu_\theta = \frac{\sqrt{\overline{v_\theta'^2}}}{V} \cdot 100\% \tag{3.4}$$

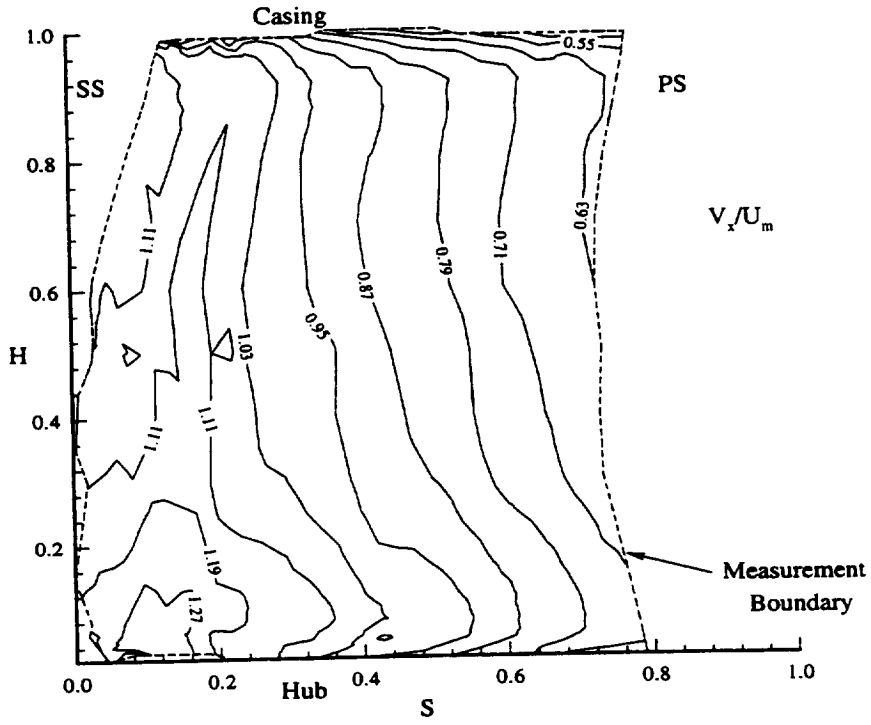

a)

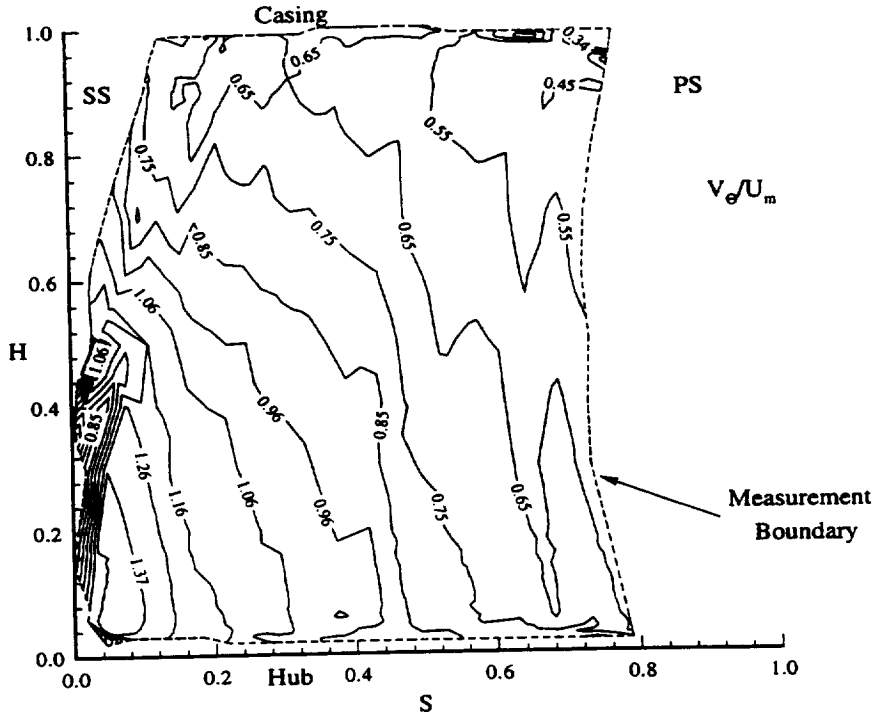

b)

Figure 3. 5 Two component LDV measurements of velocity contours at x/c_m=0.56. a) Axial velocity component V_x/U_m, b) Tangential velocity component V_θ/U_m.

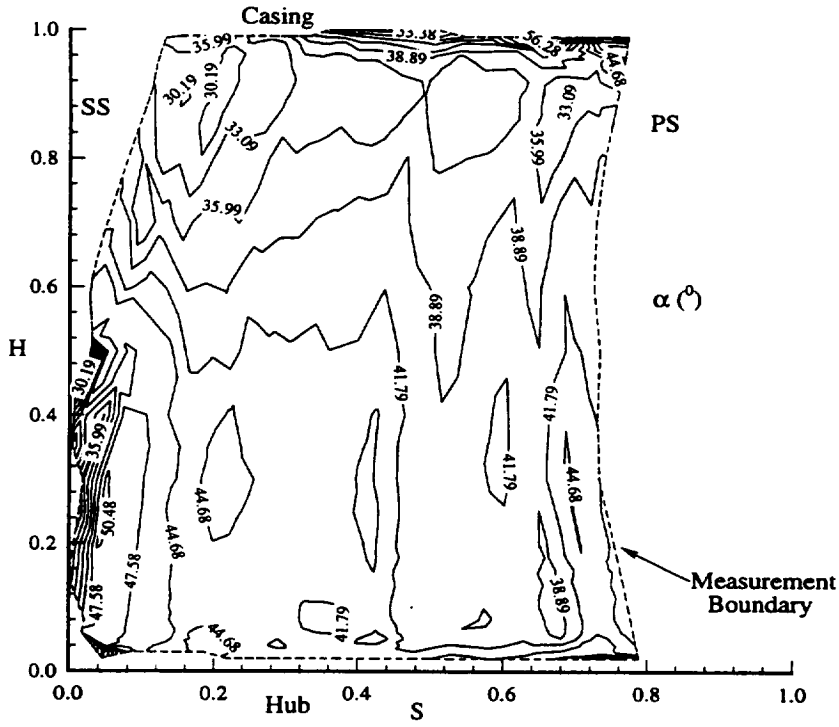

a)

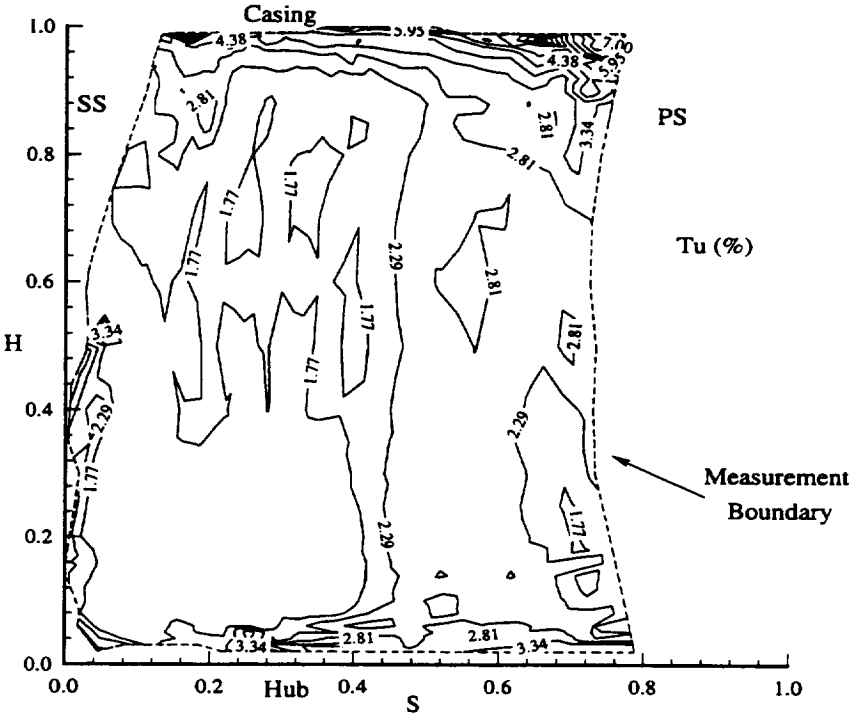

b)

Figure 3. 6 Measurements at x/c_m=0.56 using a two component LDV system. a) Contours of the yaw angle (α) in degrees, b) Total turbulence intensity (Tu).

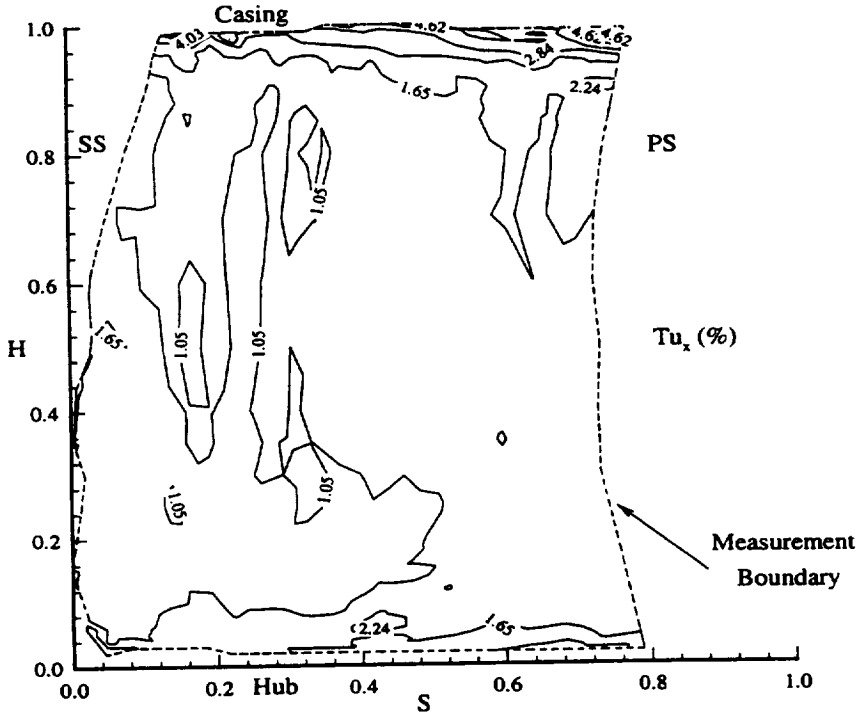

a)

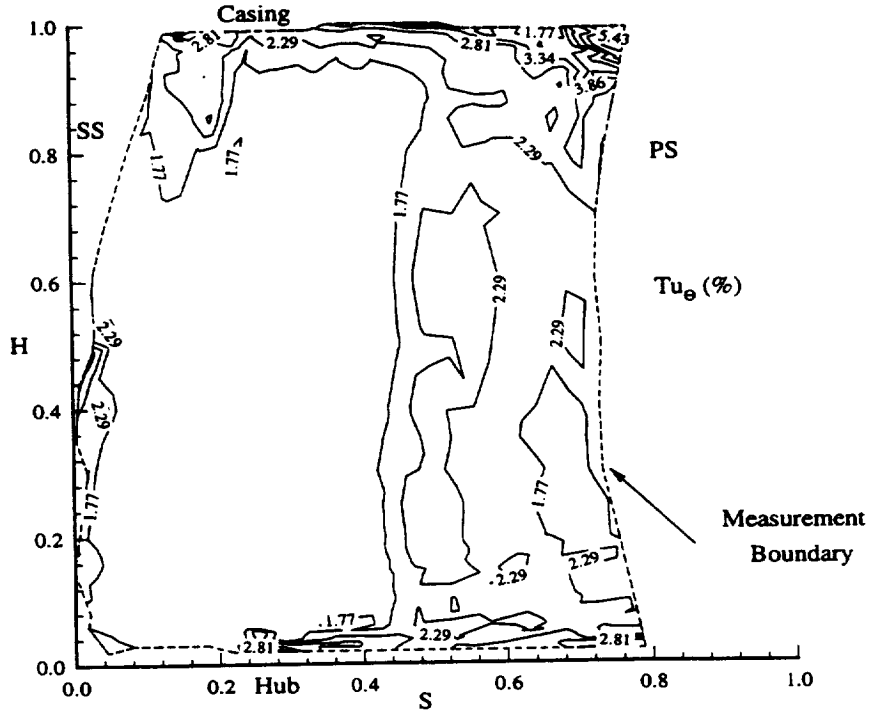

b)

Figure 3. 7 Contours of measured turbulence intensity in the a) Axial direction (Tu_x) and b) Tangential direction (Tu_θ).

The unsteadiness is again high in the endwall regions. The suction passage vortex increases the turbulence intensity in the tangential direction to a value of ≈ 3 % (Figure 3.7b) compared to the free stream value of 1.5 %.

3.3 Flow Visualization in the nozzle passage

The overall characteristics of the near wall flow field were investigated using the fluorescent oil technique. The technique under ideal conditions allows a simple method of determining the regions of laminar and turbulent flow. In some locations, the characteristics of the secondary flow in the blade passage could be observed through the visualized limiting streamlines and stagnation lines. The results are shown in Figure 3.8 and 3.9.

The hub endwall surface flow and most of the pressure surface flow of the blade is visible in Figure 3.8. The trailing edge and suction surface near wall flow is visible in Figure 3.9. The pressure surface boundary layer was tripped by the placement of serrated tape close to the leading edge hub corner, generating a separation zone which is turbulent. Due to the favorable pressure gradient, relaminarization occurred downstream of this location. On the pressure surface, the oil is removed along the leading edge due to the high laminar shear stress. Over the remainder of the blade, the oil remained uniform and covered the entire surface of the blade indicating that the pressure surface boundary layer is laminar from leading to trailing edge. Some of the visible lines are generated by the motion of the oil droplets after the termination of the experiment, especially in the trailing

Figure 3. 8 Flow Visualization of the pressure surface of the nozzle vane and the hub endwall.

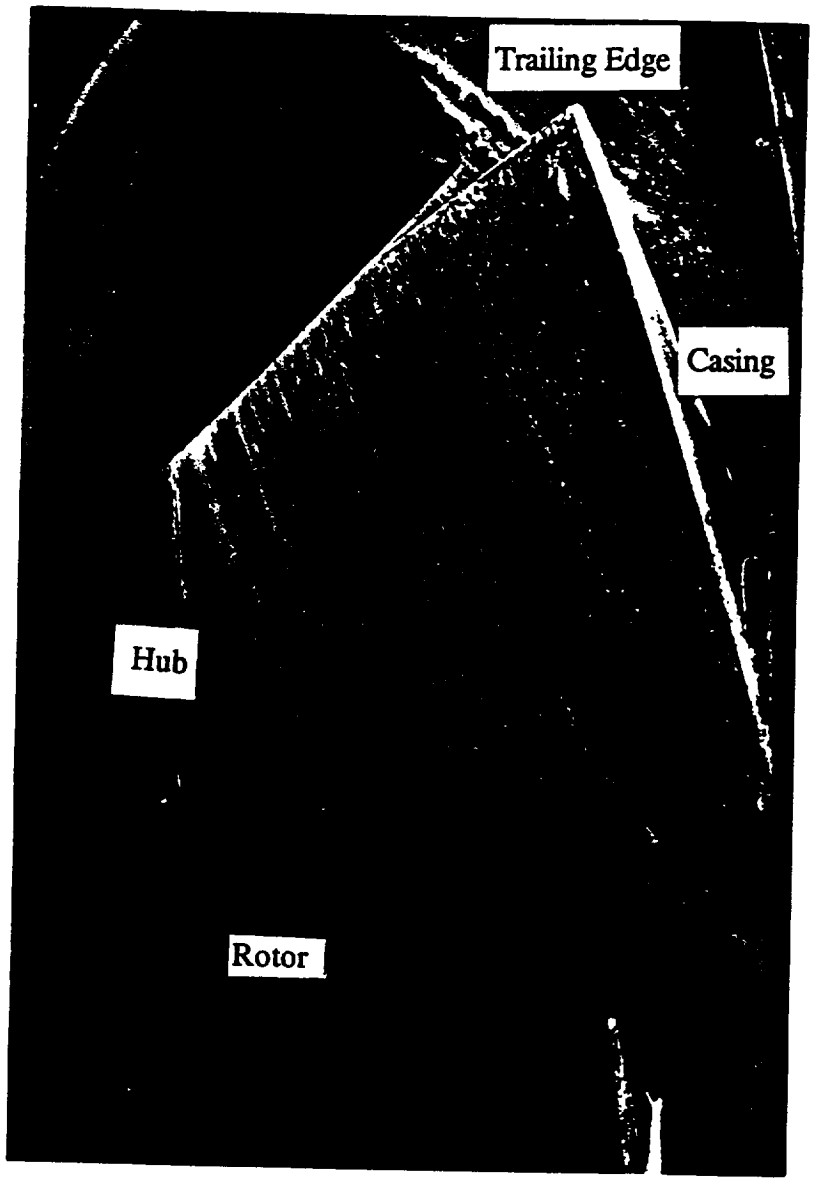

Figure 3. 9 Suction surface, trailing edge region, flow visualization.

edge and the hub endwall regions. In subsequent trials, the position of the tape was varied along the pressure surface with similar results, except at locations downstream of x/c≈0.6, where the boundary layer remained turbulent up to the trailing edge. The lines along the surface of the blade are caused by the surface tension of the oil which tends to create streaks that propagate along the blade. Along the hub endwall a thicker coat of oil was required for visualization. The higher shear stresses present in the turbulent boundary layer removed oil at a faster rate than that on the pressure surface of the blade. The effect of gravity can be clearly seen at the near leading edge, mid passage location where the low local velocity allowed more oil to accumulate than in the nozzle vane passage.

On the suction surface, the flow visualization indicate that transition occurs in the region of x/c≈0.7 to 0.8. The flow visualization in the region close to the casing endwall indicates a large region of radial inward flow (on the blade surface) which extends over most of the blade span. The secondary flow region can be clearly seen originating from approximately x/c=0.45 ~ 0.50 (minimum pressure location), where the passage vortex starts to move radial inward toward the hub. At the trailing edge, the secondary flow influences approximately 20% of the blade span in the casing corner. A second region of highly turbulent flow extends from the location of the passage vortex to approximately midspan, where the radial inward flow is appreciable.

CHAPTER 4

COMPUTATION OF THREE DIMENSIONAL BOUNDARY LAYERS

4.1 Governing Equations and Technique

The computation of the three dimensional boundary layers is based on the assumption that in the thin region close to the surface, where viscous forces dominate, the flow solution can be obtained independently from the external flow provided that the appropriate boundary conditions are imposed. This technique includes three separate steps: coordinate transformation of the general non-orthogonal surface of the turbine blade, calculation of the boundary layer edge conditions from the known static pressure distribution, and a three dimensional boundary layer analysis to predict the boundary layer growth. A brief description of the procedure is included here but detailed explanations and derivations are provided by Anderson (1985).

The obvious choice for a coordinate system transformation is to use a surface conforming non orthogonal coordinate system which would allow simpler computation than a general orthogonal system. The Cartesian coordinate system (x/c_t, y/c_t, z/c_t) of the blade profile is transformed in to the surface fitted coordinate system (s, c, n), where in general s and c are in the streamwise and crosswise direction and n is perpendicular to the surface - (s, c) plane. See Figure 4.1 for a description of the general coordinate systems used in this investigation including the (x,y,z) cartesian, (x,r,θ) cylindrical, and (s,c,n)

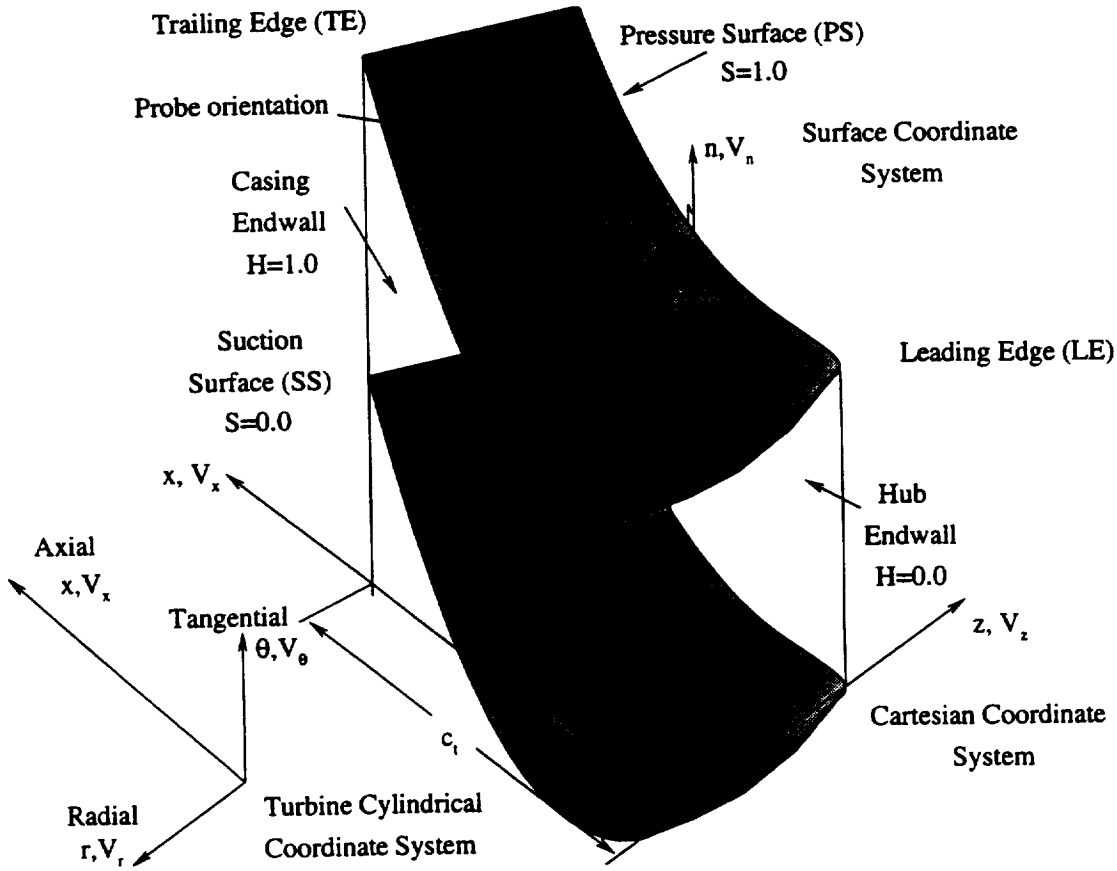

Figure 4. 1 Coordinate System Definitions for the Nozzle Vane Passage. Turbine Cylindrical Coordinate system origin is at the turbine centerline. The orientation of the hot wire probe for a typical pressure surface measurement is also show.

surface coordinate system. The transformation can be written in general as:

$$\frac{x}{c_t}=\frac{x(s,c,n)}{c_t} \qquad \frac{y}{c_t}=\frac{y(s,c,n)}{c_t} \qquad \frac{z}{c_t}=\frac{z(s,c,n)}{c_t} \tag{4.1}$$

The Jacobian of the transformation is defined as $J=\left|\partial x_i/\partial s_i\right|\neq 0$. Therefore the covariant metric tensor of the transformation can be written in the following form:

$$g_{ij}=\frac{\partial x_k}{\partial s_i}\frac{\partial x_k}{\partial s_j} \tag{4.2}$$

The transformation from the physical (x/c_t, y/c_t, z/c_t) to the computational (s, c, n) can now be accomplished.

In the transformed coordinate system it is still difficult to accurately capture the gradients in the boundary layer region, and in the case of a turbulent boundary layer the two different length scales. A suitable transformation for three dimensional boundary layer equations applicable to turbulent flow was developed by Vatsa (1984) as a modification to the Levy-Lees coordinates defined as:

$$\begin{aligned}\xi_1&=\int_0^s q_0 ds\\ \xi_2&=c\\ \xi_3&=\frac{V_{edge_s}H_2}{\sqrt{2\xi_1}}\int_0^n \rho dn\end{aligned} \tag{4.3}$$

Where V_{edge_s} is the local boundary layer edge velocity in the streamwise direction, q_0 is the Levy-Lees length scale parameter at surface leading edge, and $H_2=\sqrt{g_{11}}/c_t$. The independent variables (ξ_1, ξ_2, ξ_3) are used to transform the original system of equations (Appendix D) which are then solved using a finite difference algorithm.

The turbulence model used is based on the two dimensional model developed by Cebeci and Smith (1974). The model divides the boundary layer region into an inner and outer region length scale. A simple laminar/turbulent transition model (Dhawan and Narasimha, 1958) defines the intermittency factor Γ as:

$$\Gamma = 1 - \exp\left[-4.6513\left(\frac{s - s_{tran_1}}{s_{tran_2} - s_{tran_1}}\right)^2\right] \tag{4.4}$$

where s_{tran1} and s_{tran2} are the locations of beginning and end of transition. The presence of non-isotropic turbulence is accounted for by multiplying the eddy viscosity in the cross flow direction by a user specified factor.

The boundary layer edge conditions are defined by solving the Euler equations along the surface from a known surface static pressure distribution (typically experimentally measured).

4.2 Input Grids and Flow Conditions for the Nozzle Passage Calculation

Calculation of the three-dimensional boundary layers requires appropriate specification of the inflow boundary conditions and surface coordinates. The nozzle blade passage surface coordinate grids are shown in Figures 4.2 and 4.3. For the actual computation, the grids are slightly modified by the addition of a flat surface at the trailing edge to account for the variation in chord length in the spanwise direction. The boundary layer on endwall surfaces are computed using a local similarity solution with $\xi_1 > 0$ to allow for sufficient boundary layer development along the inlet endwall surfaces. The starting

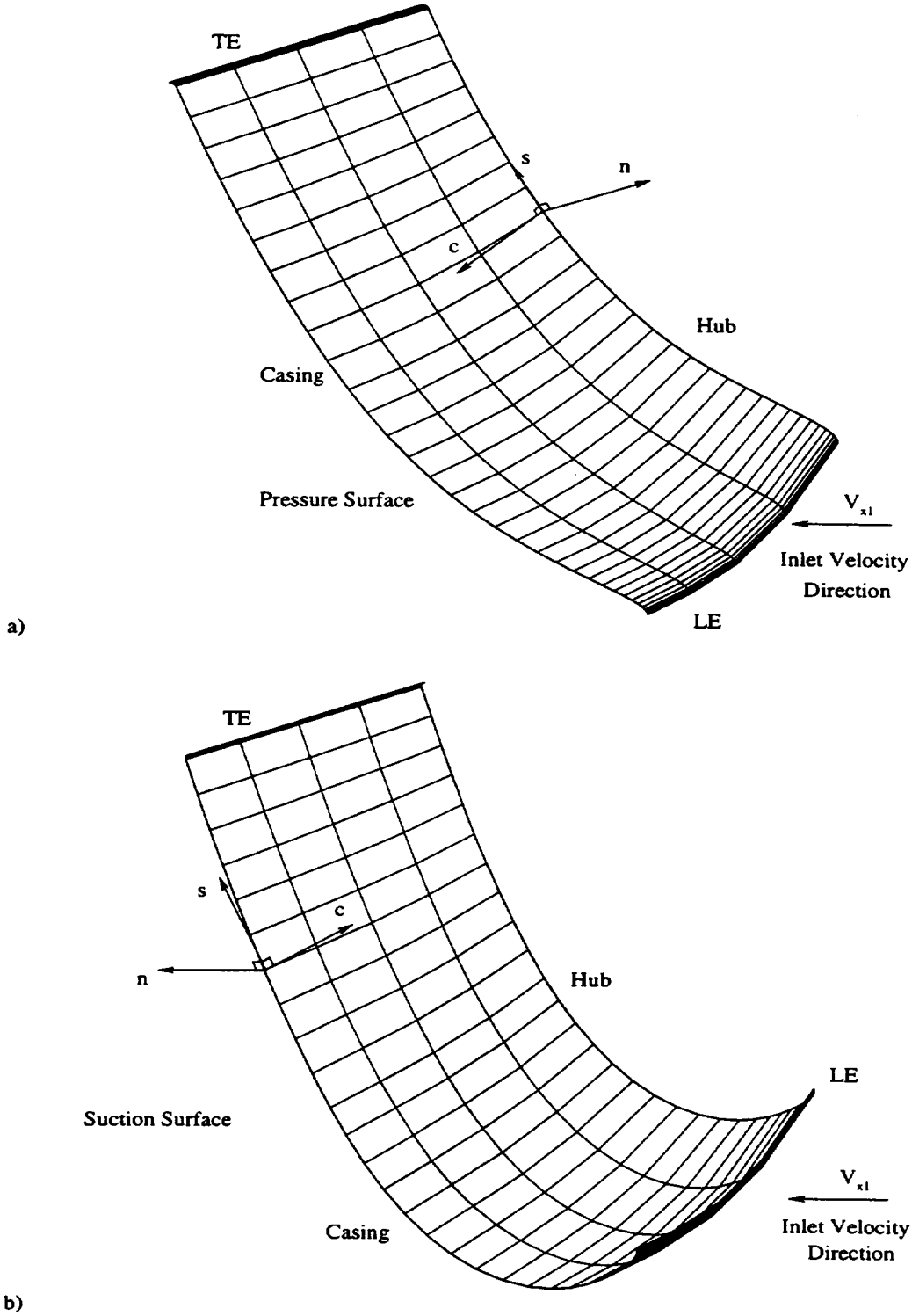

Figure 4. 2 Nozzle vane surface input geometry. a) Pressure surface computational mesh. b) Suction surface computational mesh.

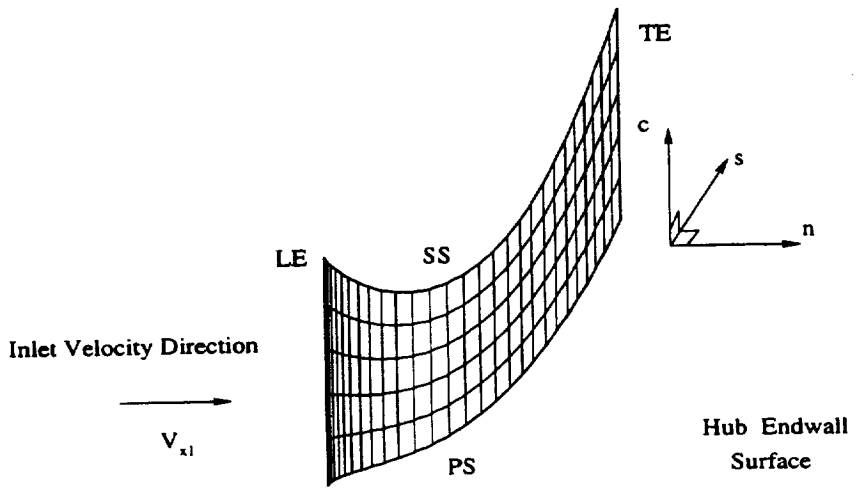

a)

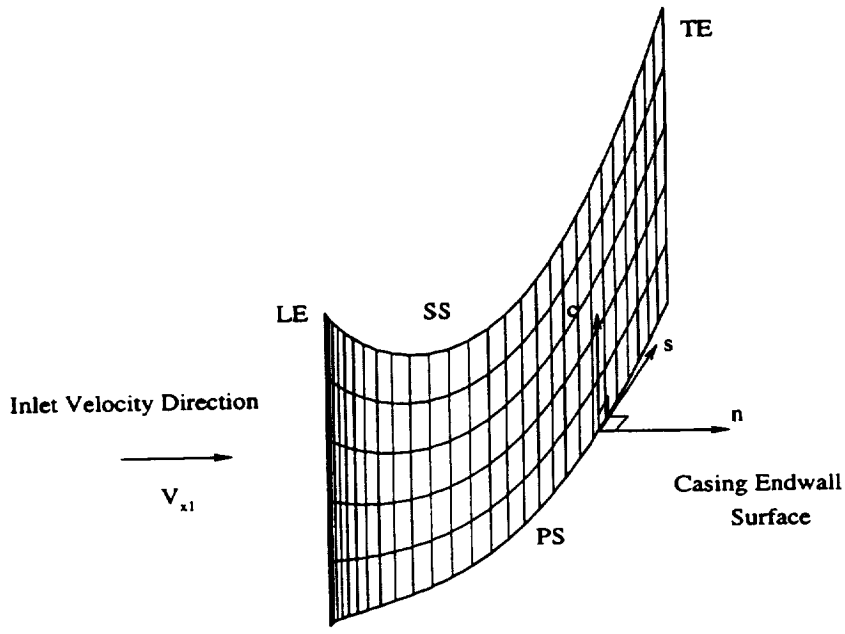

b)

Figure 4. 3 Nozzle passage endwall surface input geometry. a) Hub endwall surface, b) Casing endwall surface.

length ξ_1 was adjusted to match the endwall boundary layer thickness at one chord upstream of the leading edge measured by Zaccaria (1994), 4.5% of the blade span at the hub and 8.7% at the tip. The boundary layers were also found to be fully turbulent along the endwall surfaces and were computed using the turbulent form of the Lees-Levy coordinates.

The experimentally measured static pressure distribution used to compute the boundary layer edge conditions (from Fig. 3.1 and 3.3) was smoothed eight times using an average of the neighboring points. The resulting pressure distribution is shown in Figures 4.4a and 4.5a for the endwall surfaces and in Figures 4.6a and 4.7a for the blade surface. The pressure coefficient for the computation is defined as $C_P = \frac{p - P_0}{\frac{1}{2}\rho V_{x1}^2}$. The surface Euler equations - streamwise and crosswise momentum and energy equation, were integrated from the measured pressure distribution to obtain the edge velocity vectors shown in Figure 4.4b, 4.5b, 4.6b, and 4.7b. In all figures for the passage boundary layer edge velocities, the reference velocity used is the upstream axial velocity V_{x1} (≈29.8 m/s).

The endwall computations were performed using the zero crosswise velocity option across the boundaries of the computational space. The boundary layer edge velocity increased uniformly from pressure to suction surface over most of the endwall surfaces till the region where secondary flow is present. The boundary layer procedure is not valid in the secondary flow region. On the hub endwall, the boundary layer edge vectors exhibit a discontinuity starting at x/c_t=0.7 due to a decrease in the static pressure

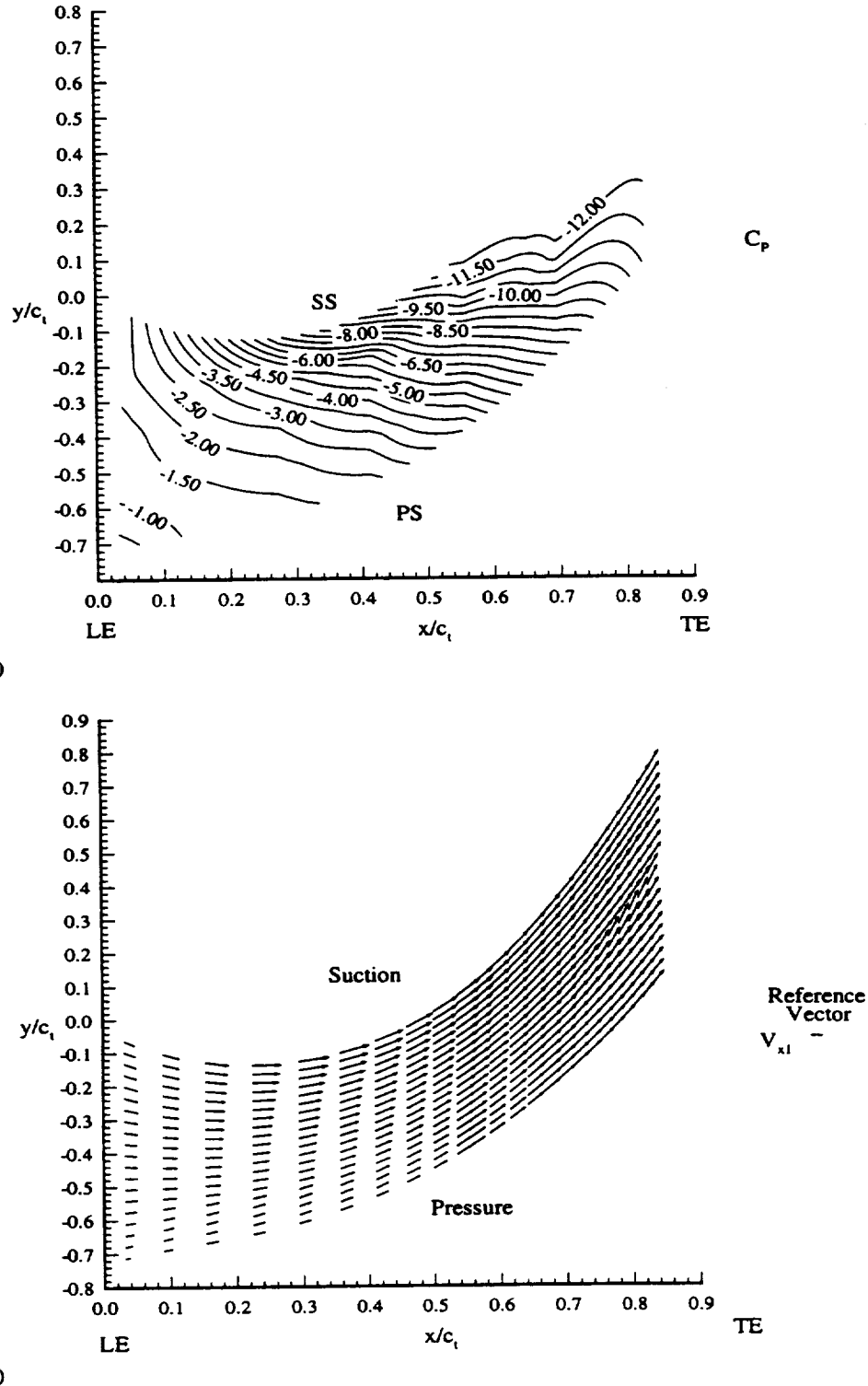

Figure 4. 4 The Euler solution of boundary layer in-flow properties on the hub endwall. a) Smoothed C_P, b) Boundary layer edge velocity vectors (V_{x1} reference).

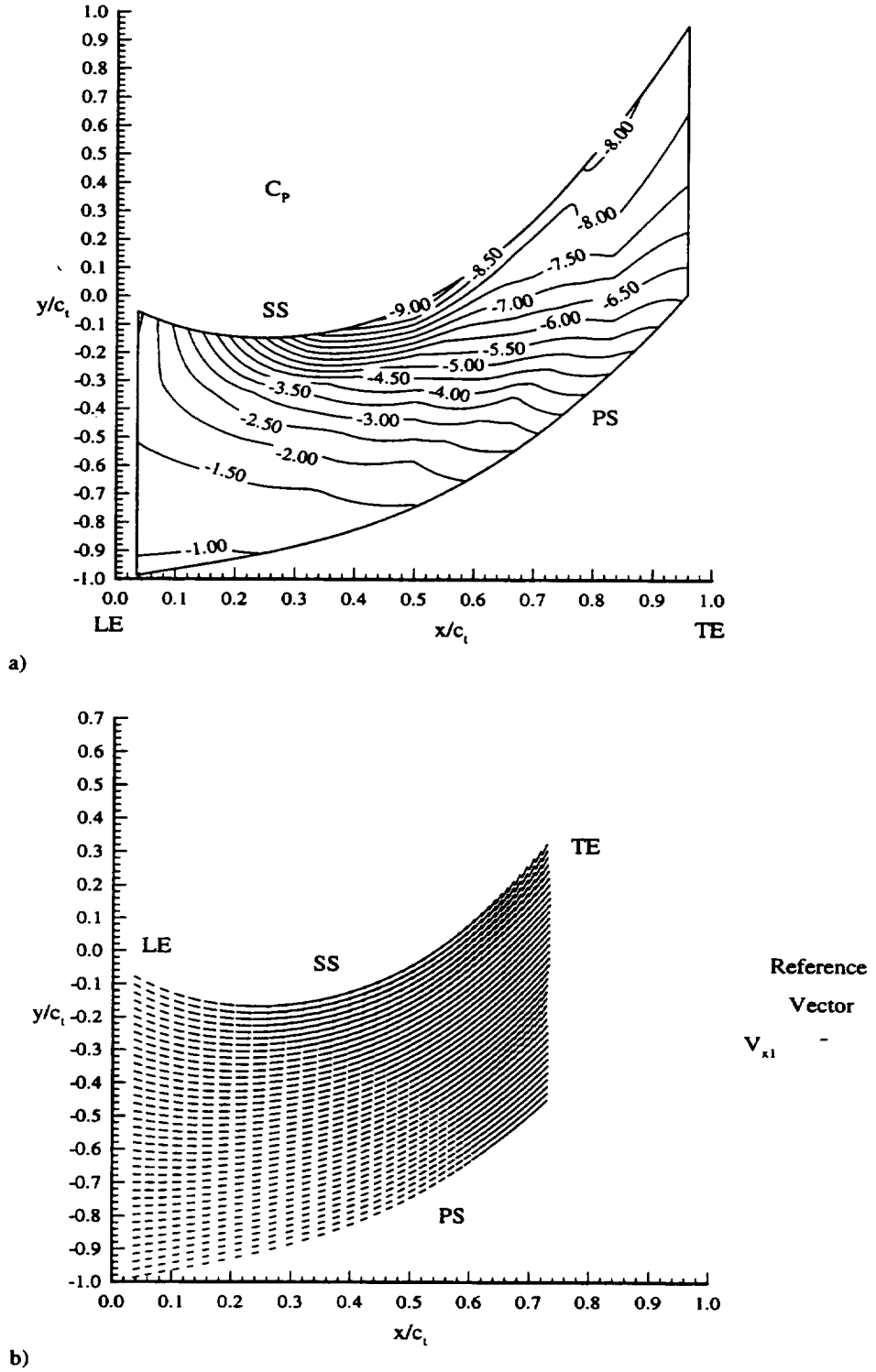

Figure 4. 5 The Euler solution of boundary layer in-flow properties on casing endwall surface. a) Smoothed C_P, b) Boundary layer edge velocity vectors.

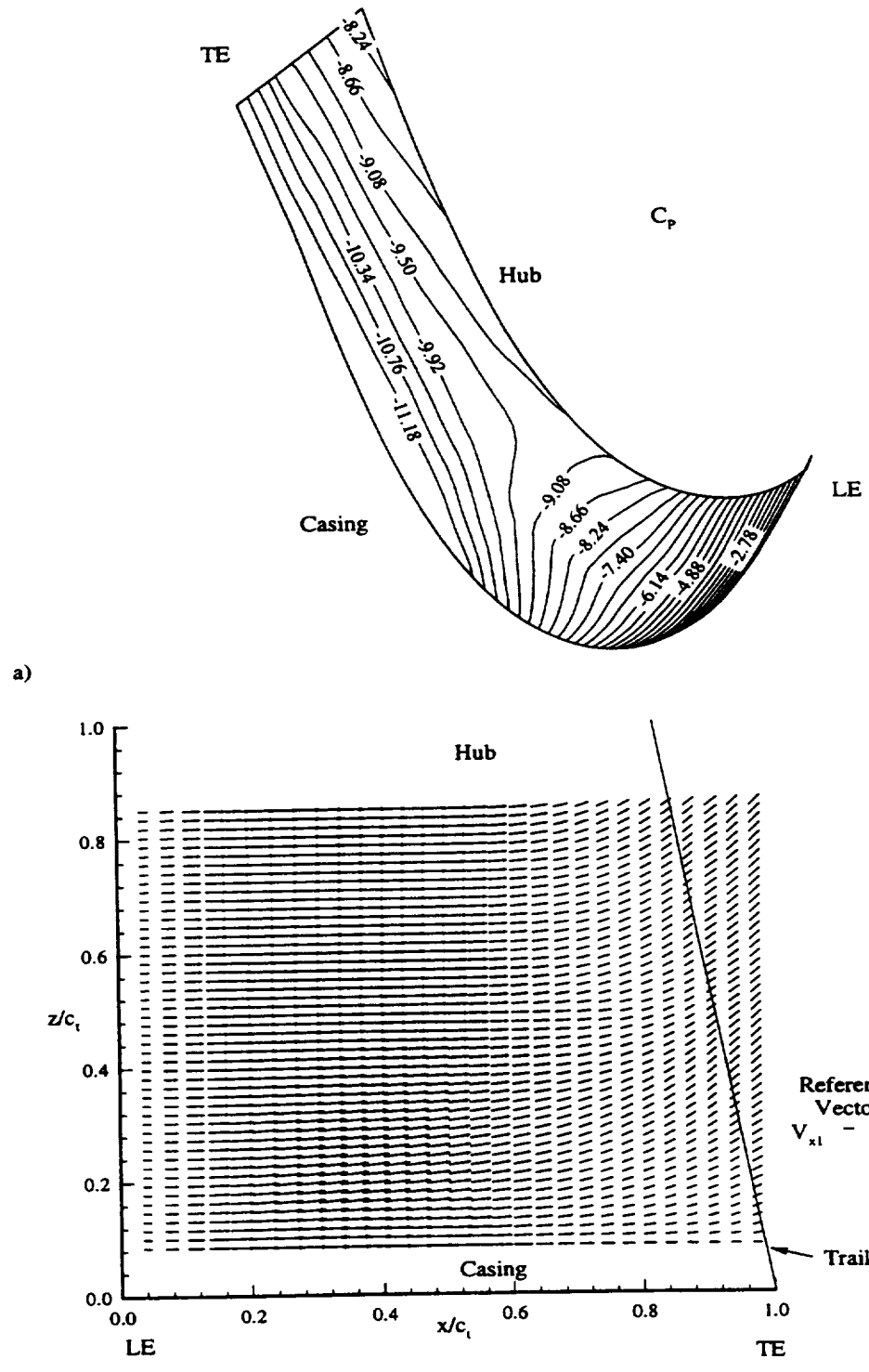

Figure 4. 6 Computed boundary layer in-flow properties on suction surface. a) Smoothed C_P, b) Boundary layer edge velocity vectors.

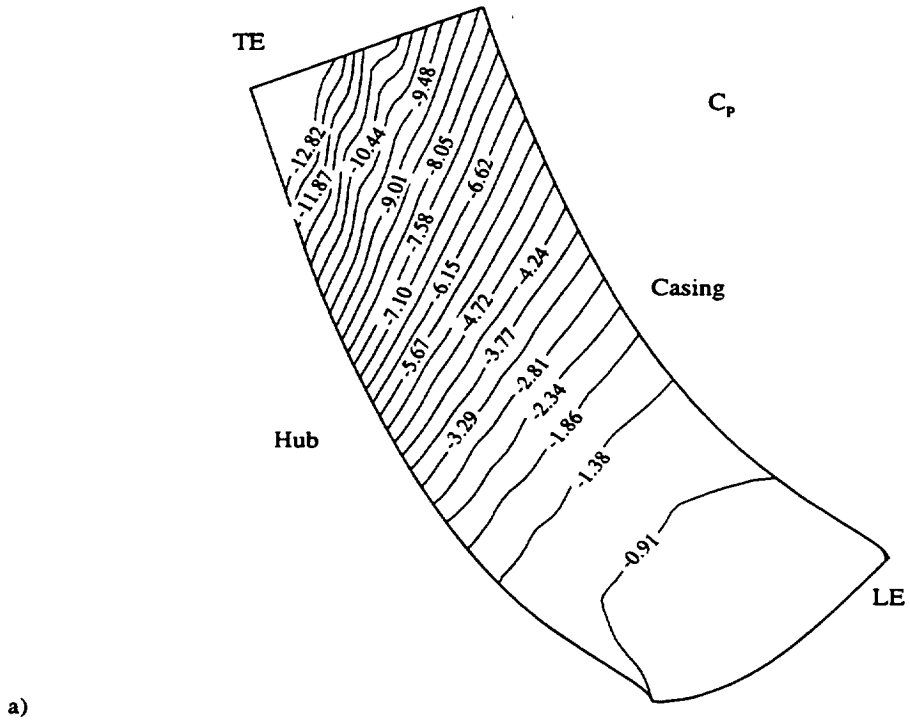

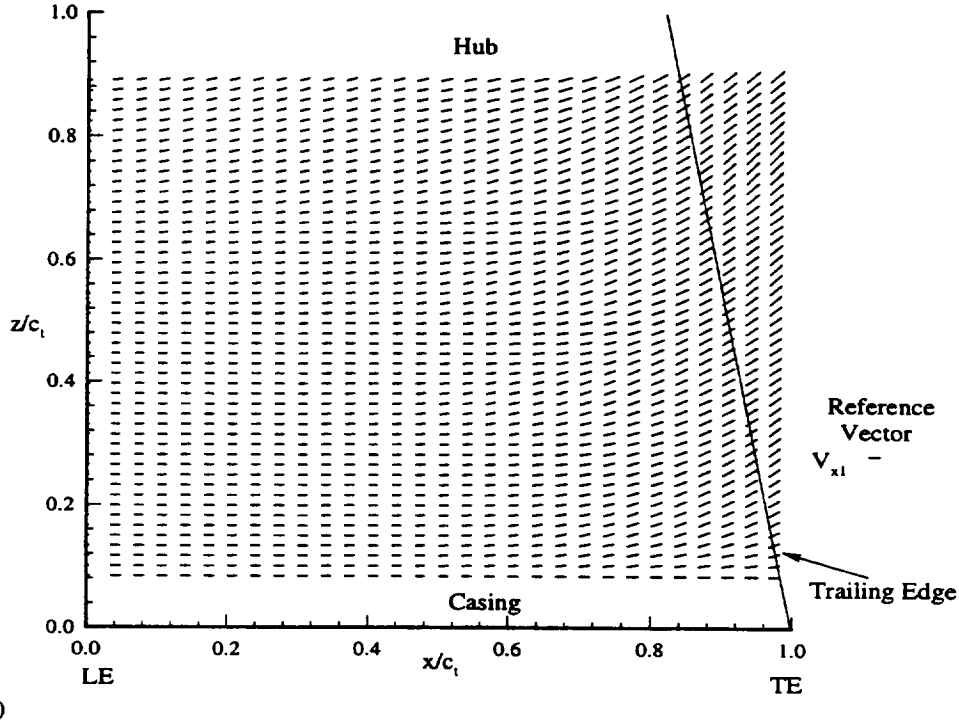

Figure 4. 7 Euler solution of boundary layer in-flow properties on pressure surface. a) Smoothed C_P, b) Boundary layer edge velocity vectors.

in this region (see Figure 3.3b). The prediction in this region, extending from the mid passage to the suction surface, is not very accurate. The flow acceleration is fairly uniform up to the region of strong secondary flow.

On the casing surface the predictions in the region close to the trailing edge and suction surface are not plotted, since the solution is not accurate for the same reasons mentioned above. Along the suction surface boundary layer, the adverse pressure gradient and high curvature tend to deviate the flow from the free stream direction toward the blade beyond the minimum pressure location . This ultimately leads to the divergence of the solution in the downstream region. This effect is due to the difficulty in specifying the inflow conditions along the boundaries.

On the blade surfaces the endwall region (in the hub region up to $z/c_t = 0.085$ and in the casing region from $z/c_t = 0.89$) was excluded from the computation for the reasons mentioned above. The smoothed pressure distribution shown in Figures 4.5a and 4.6a influence the radial inward flow (from casing toward hub) along most of the blade span at the trailing edge. On the suction surface the computed boundary layer edge velocity vectors (Figure 4.5b) exhibited radial inward components, starting at $x/c_t=0.2$ in the casing region. The flow in the mid blade and hub regions is uniform up to $x/c_t=0.65$ where the deviation from the axial direction occurs. This would indicate that up to this region, the boundary layers are essentially two-dimensional in nature and any deviation can be attributed mainly to the influence of surface curvature.

4.3 Computed Boundary Layer Properties

The computed properties on the passage endwalls and blade surfaces are calculated in the intrinsic coordinate system - oriented with respect to the streamwise and cross flow direction. The local edge total velocity (V_{edge}) is considered to be the free stream value. The integral properties are computed from the velocity profiles in the boundary layer. Displacement thickness in the streamwise and crosswise direction (δ_s^* and δ_c^*) can be defined for the vane boundary layer as (see Figure 4.1):

$$\delta_s^* / c_t = \int_0^{h>\delta} \left[1 - \frac{\rho V_s}{\rho_{edge} V_{edge}} \right] d(n / c_t) \tag{4.5}$$

$$\delta_c^* / c_t = \int_0^{h>\delta} \left| \left[\frac{\rho V_c}{\rho_{edge} V_{edge}} \right] \right| d(n / c_t) \tag{4.6}$$

The momentum thickness in the stream wise (θ_s) and crosswise (θ_c) direction is:

$$\theta_s / c_t = \int_0^{h>\delta} \frac{\rho V_s}{\rho_{edge} V_{edge}} \left[1 - \frac{V_s}{V_{edge}} \right] d(n / c_t) \tag{4.7}$$

$$\theta_c / c_t = \int_0^{h>\delta} \left| - \frac{\rho V_s}{\rho_{edge} V_{edge}} \frac{V_c}{V_{edge}} \right| d(n / c_t) \tag{4.8}$$

In addition the wall friction coefficient C_{fs} based on the streamwise wall shear stress τ_{sw} can be defined as:

$$C_{fs} = 2 \frac{\tau_{sw}}{\rho_{edge} V_{edge}^2} \tag{4.9}$$

An additional boundary layer property is the thickness of the boundary layer (δ),

determined at the location where the local velocity is equal to 99% of the free stream velocity.

4.3.1 Boundary Layer Prediction on Suction Surface

The computation of the suction surface boundary layer was performed using 100 grid points in the direction normal to the surface within the boundary layer (results are shown in figures 4.8, 4.9,4.10 and 4.11). The computational starting location was the leading edge stagnation point. On the surface of the blade, 90 grid lines in the chordwise and 70 grid lines in the pitch wise grid were used with very little stretching.

The intermittency transition model described earlier (Equation 4.4), requires specification of the starting and ending location of transition. Based on the flow visualization of the suction surface (Figure 3.8 and 3.9), the transition region was positioned starting from x/c_t=0.7 and ending at x/c_t=0.8. The model does not allow spanwise variation of the transition location, therefore the transition occurs at different chordwise positions along the spanwise and this can be seen from the variation of C_{fs} in Figure 4.8a. The transition region extended from x/c=0.64 to 0.76 at the tip to x/c=0.74 to 0.85 at the root of the blade. The wall skin friction coefficient C_{fs}, presented in Figure 4.8a, decreases rapidly from a maximum at the leading edge (due to the high curvature and rapid acceleration) to the transition location at x/c_t=0.7. The values of C_{fs} decreased in the laminar region up to the transition location, and the change is smooth across the transition region increasing to a constant value of 0.005 toward the trailing edge. The shape factor

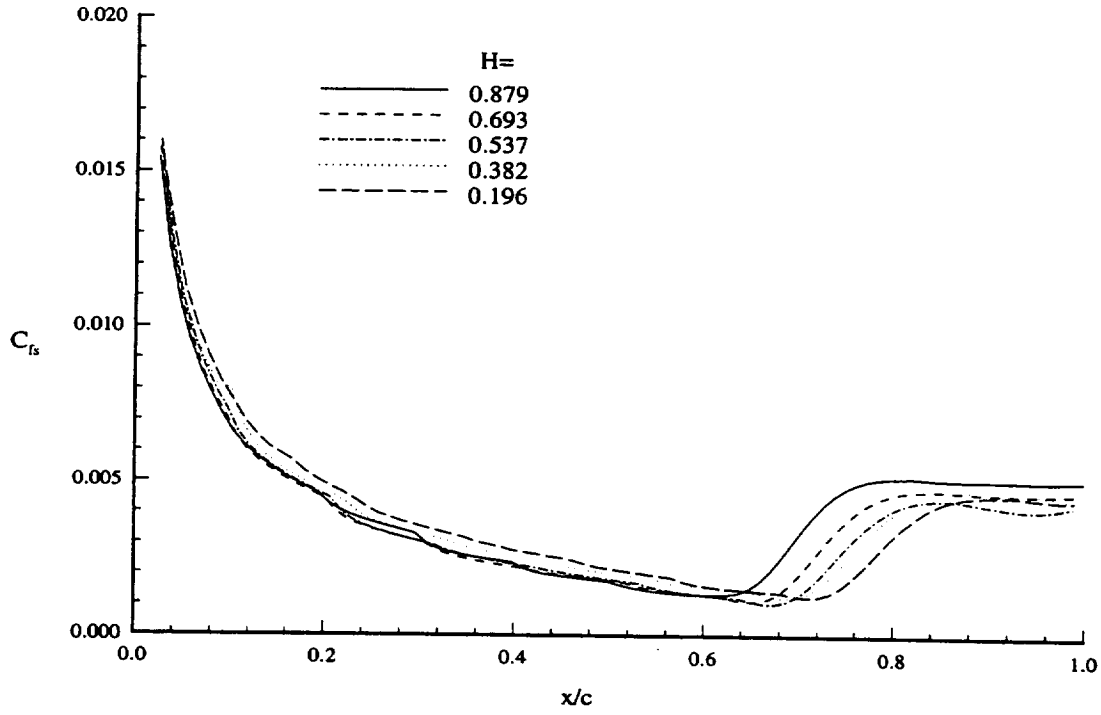

a)

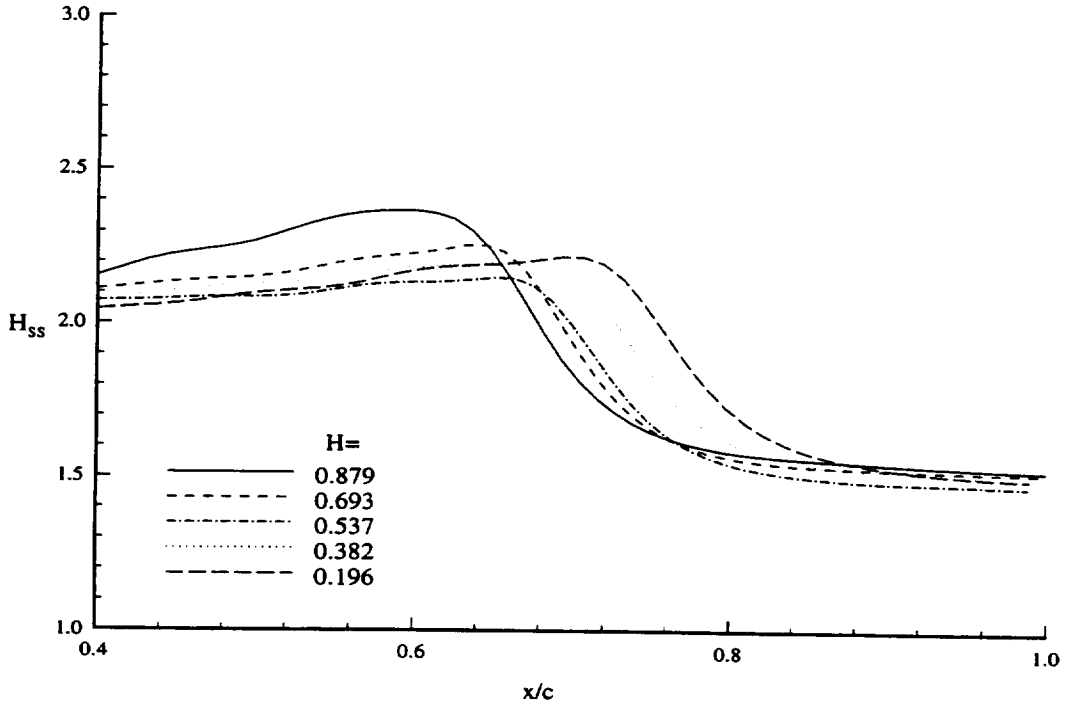

b)

Figure 4. 8 Predicted a) Wall friction coefficient $C_{fs}=2\tau_{sw}/(\rho_{edge}V_{edge}^2)$ and b) Shape factor H_{SS} ($H_{SS}=\delta^*_s/\theta_s$) on the suction surface.

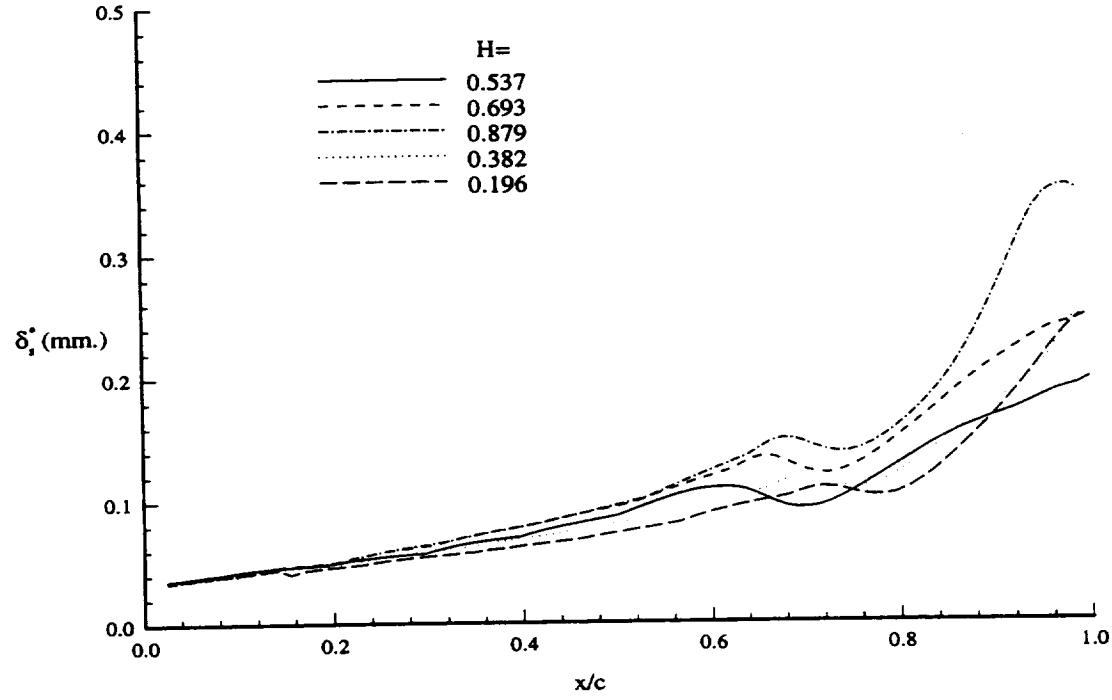

a)

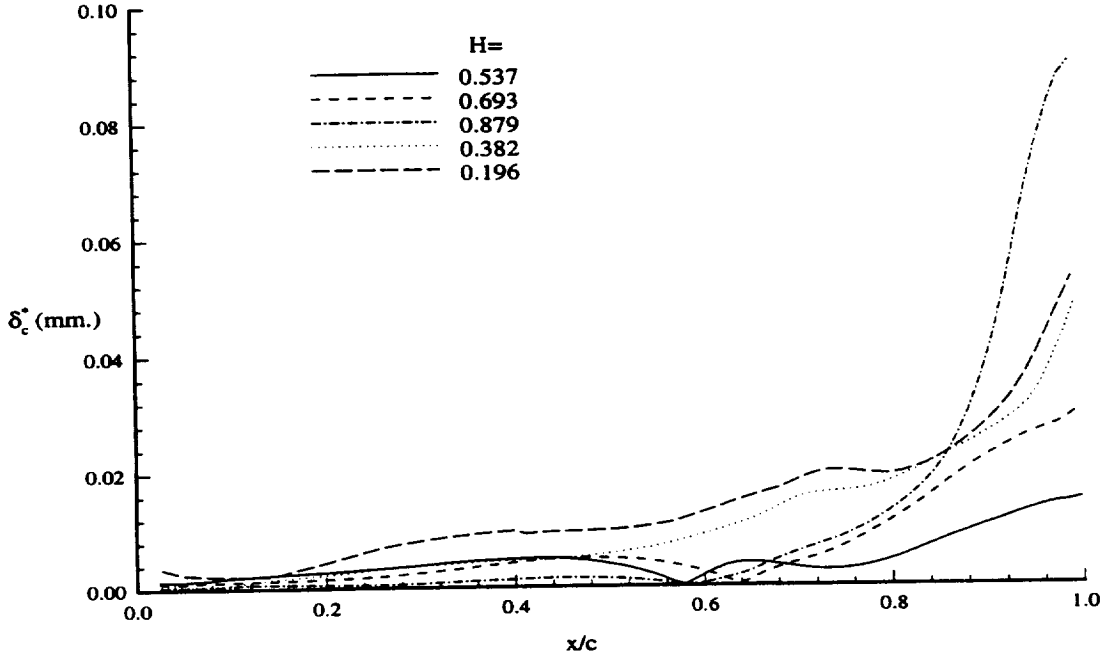

b)

Figure 4. 9 Computed displacement thickness on suction surface. a) Streamwise displacement thickness (δ_s^*), b) Crosswise displacement thickness (δ_c^*).

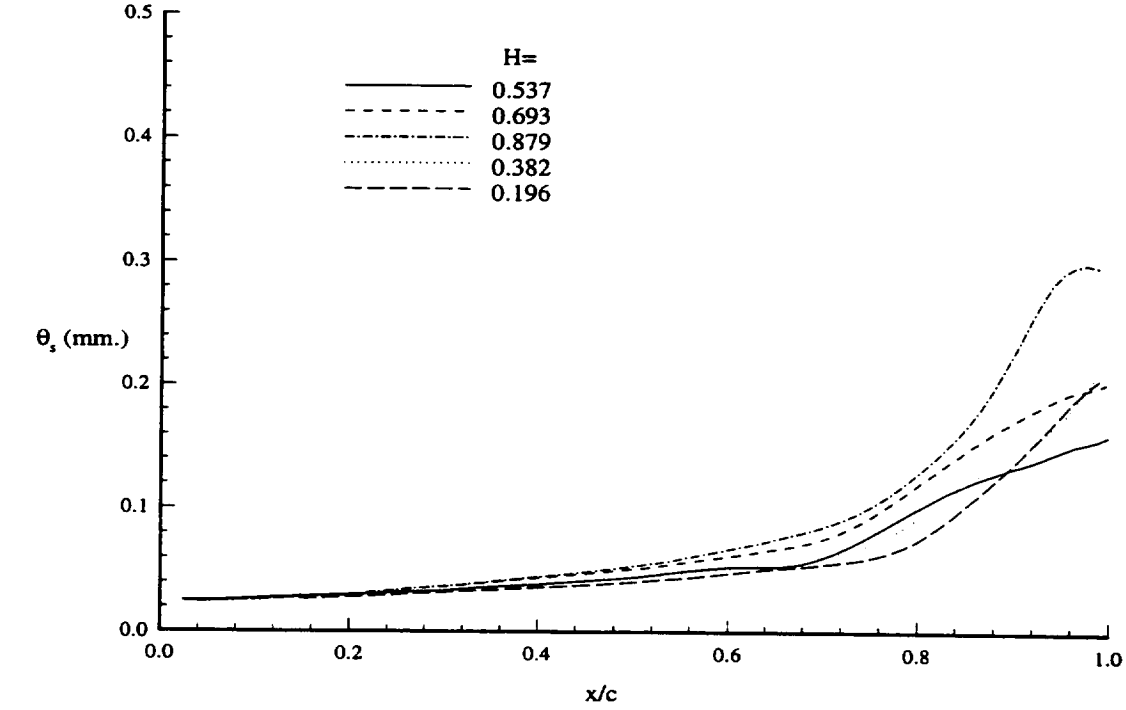

a)

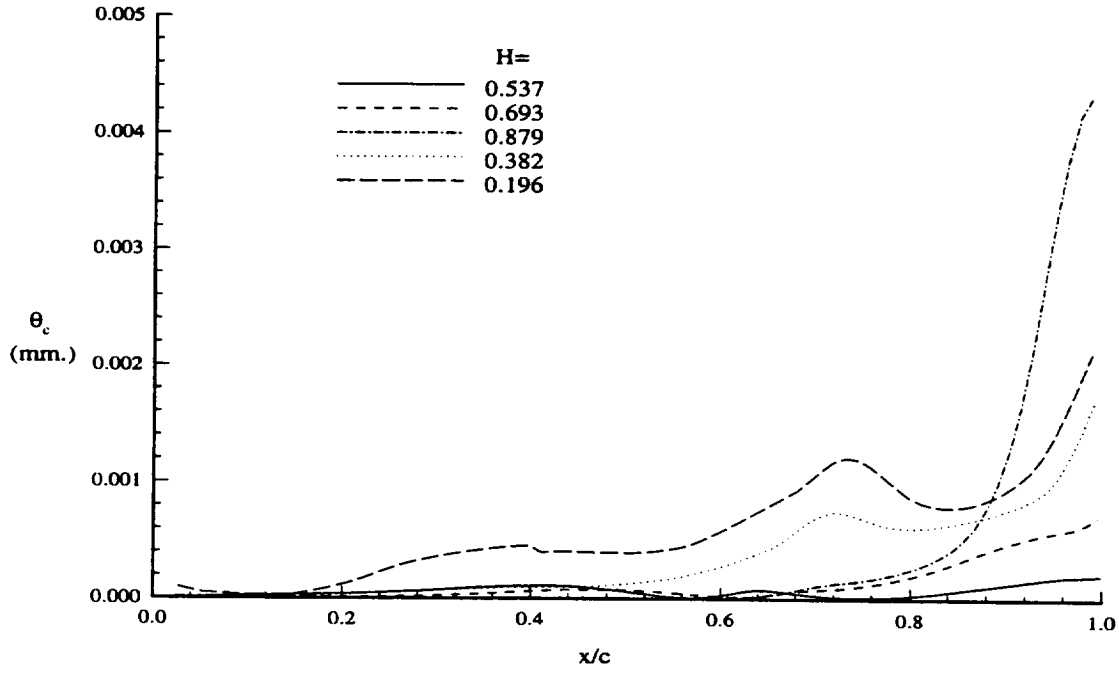

b)

Figure 4. 10 Predicted momentum thickness on suction surface. a) Streamwise momentum thickness (θ_s) , b) Crosswise momentum thickness (θ_c).

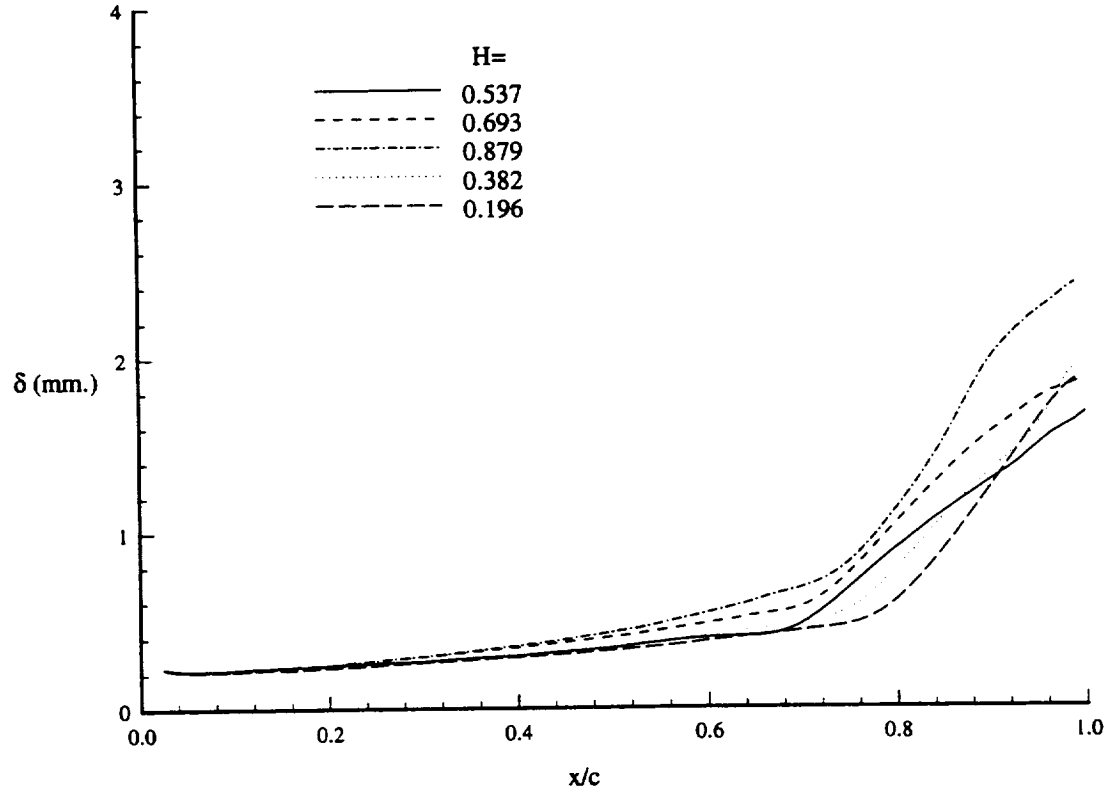

Figure 4. 11 Predicted boundary layer thickness (δ) on suction surface.

H_{SS}, (ratio of momentum and displacement thickness in the streamwise direction) presented in Figure 4.8b, exhibits a characteristic decrease from the laminar region (H_{SS} $\approx$2.1) to a level of $H_{SS} \approx 1.5$ in the turbulent region.

The variation in displacement thickness along the blade surface increased uniformly in the laminar region up to the transition region (Figure 4.9a). The decrease in δ_s^* and the increase in the transition region is due to entrainment of the free stream fluid in the turbulent boundary layer. Again, the maximum increase in δ_s^* occurs in the tip region due to the adverse pressure gradient caused by the secondary flow. In the cross wise direction (Figure 4.9b), the overall level of the displacement thickness δ_c^* was very close to zero indicating very small three dimensionality of the boundary layers up to x/c=0.6, due to the small radial pressure gradient. Along the tip region of the suction surface, the boundary layer thickness (δ) and displacement thickness (δ_s^*) start to increase appreciably at approximately x/c=0.75 to a maximum at the trailing edge.

The momentum thickness on the suction surface in the streamwise direction (θ_s), shown in Figure 4.10a, starts to increase rapidly after the transition location with the maximum value occurring again in the tip region. The momentum thickness (θ_s) in the cross flow direction (Figure 4.10b) is almost zero at the mid span location. In the tip region the increase is higher at H=0.879, occurring only in the aft 20% of the blade chord.

The boundary layer thickness shown in Figure 4.11, increased most rapidly in the region close to the casing due to the adverse chordwise pressure gradient imposed by the secondary flow. The maximum value at the trailing edge was calculated to be 2.41 mm. at

H=0.879. The boundary layer growth was smallest in the mid span region where the calculated value was found to be about 1.9 mm. at the trailing edge.

4.3.2 Boundary Layer Prediction on Pressure Surface

The boundary layer on the pressure surface was computed assuming laminar boundary layers (based on flow visualization) over the entire chord length and span of blade. The grid used consisted of 90x70 computational points on the blade surface and 100 grid points in the normal direction.

The predicted three dimensionality of the pressure surface boundary layer was lower compared to that of the suction surface. The distribution of skin friction coefficient and the boundary layer thickness on the pressure surface is shown in Figure 4.12. The predicted values of the momentum and displacement thickness, in the streamwise and crosswise directions, are shown in Figures 4.13 and 4.14.

The wall skin friction coefficient C_{fs} (presented in Figure 4.12a), reached a maximum value at locations ranging from x/c=0.49 at the root to x/c=0.63 at the tip, slightly downstream of the location of maximum values of the integral properties. The magnitudes of C_{fs} on the pressure surface are lower than those on the suction surface, especially in the leading edge region. The growth of boundary layer thickness (Figure 4.12b) is almost uniform in the spanwise direction up to approximately x/c=0.35, due to the small variation in the blade profile geometry up to that location. Downstream of the maximum boundary layer thickness location (varies in the spanwise direction, i.e. x/c=0.41

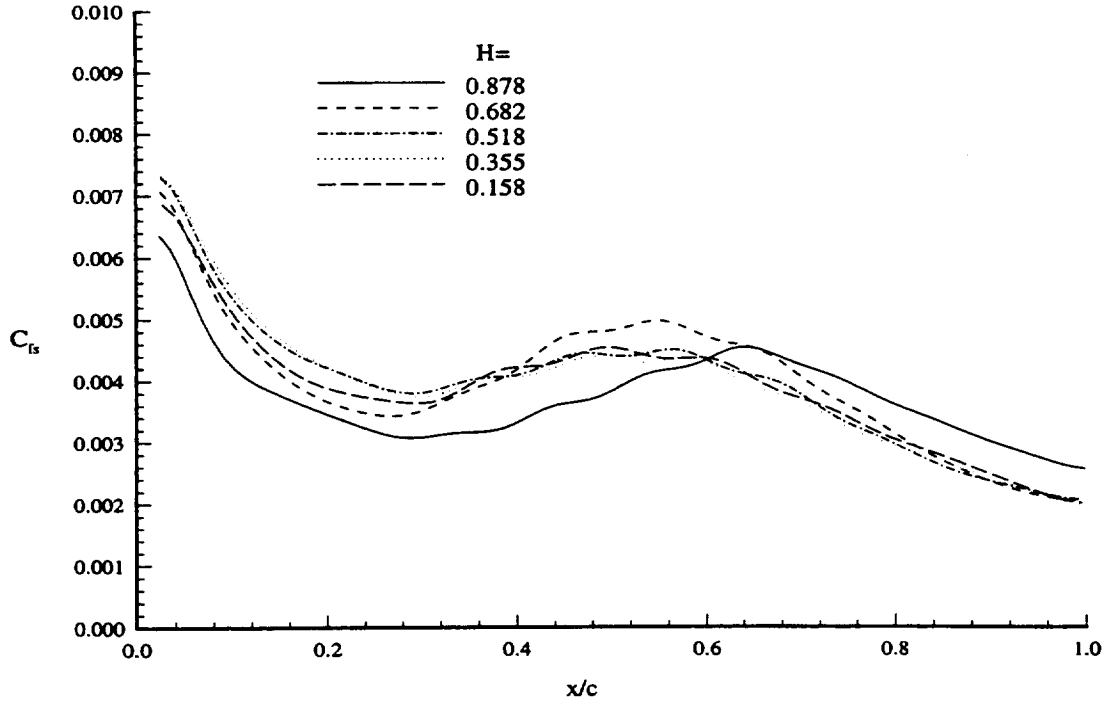

a)

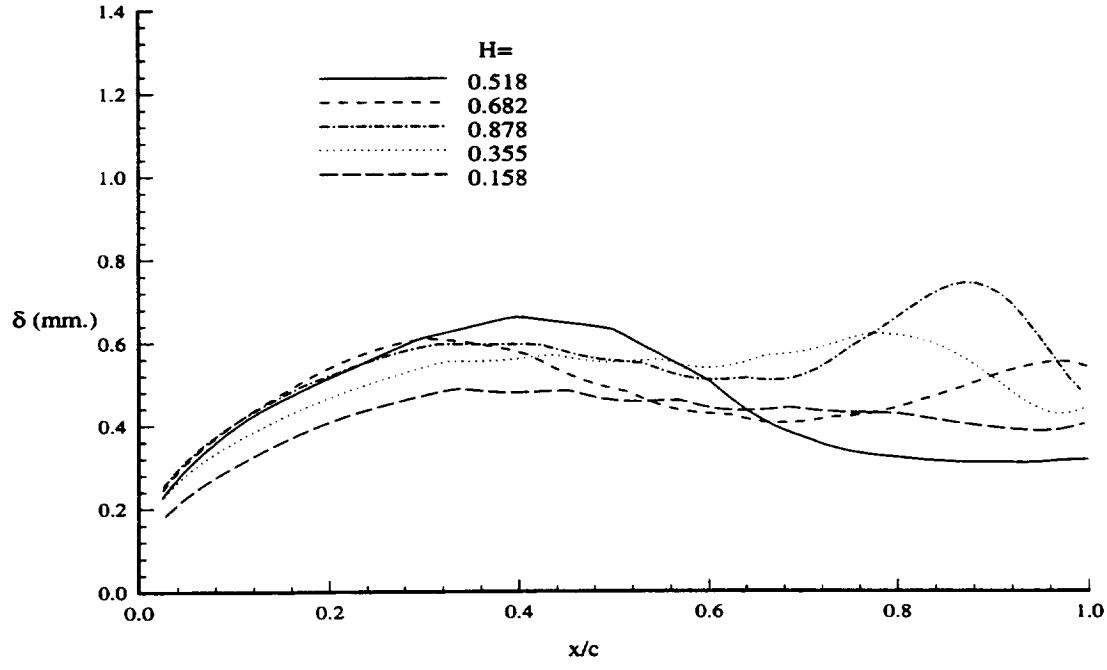

b)

Figure 4. 12 Computed a) Wall friction coefficient, and b) Boundary layer thickness on pressure surface.

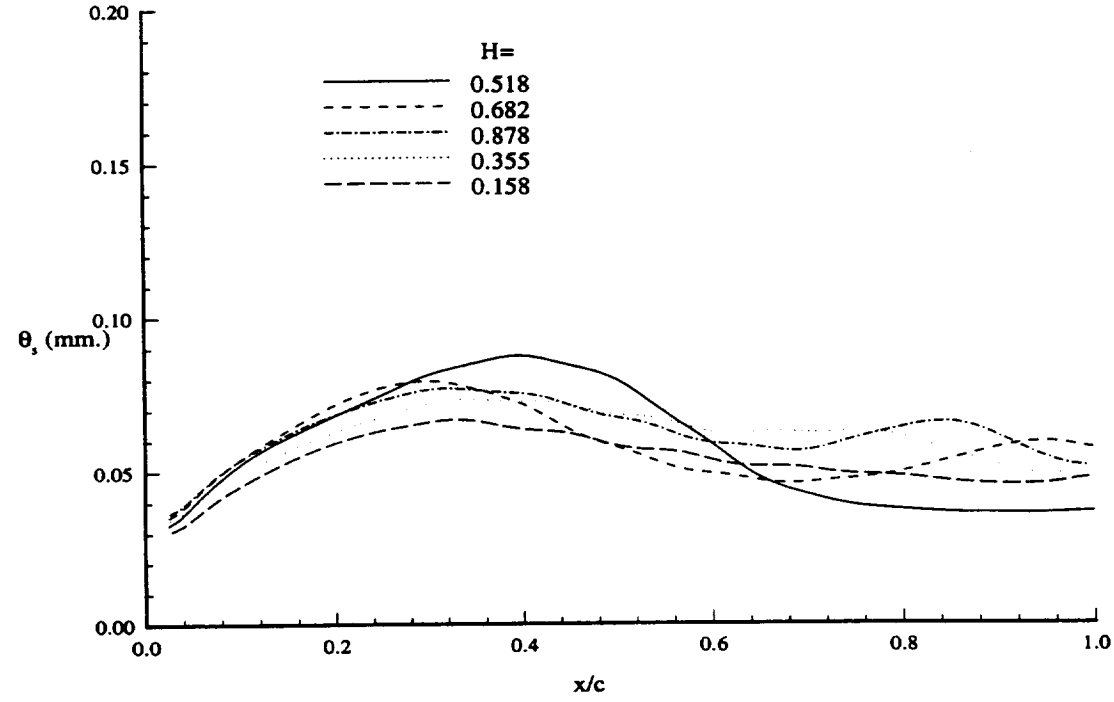

a)

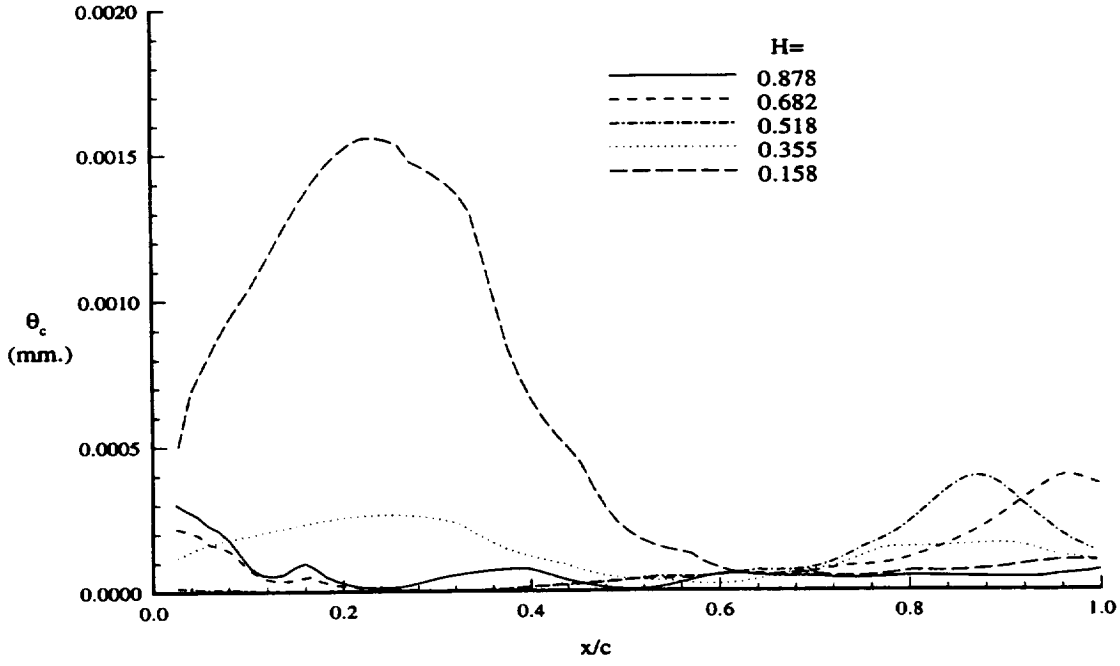

b)

Figure 4. 13 Computed momentum thickness on pressure surface. a) Streamwise, b) Crosswise.

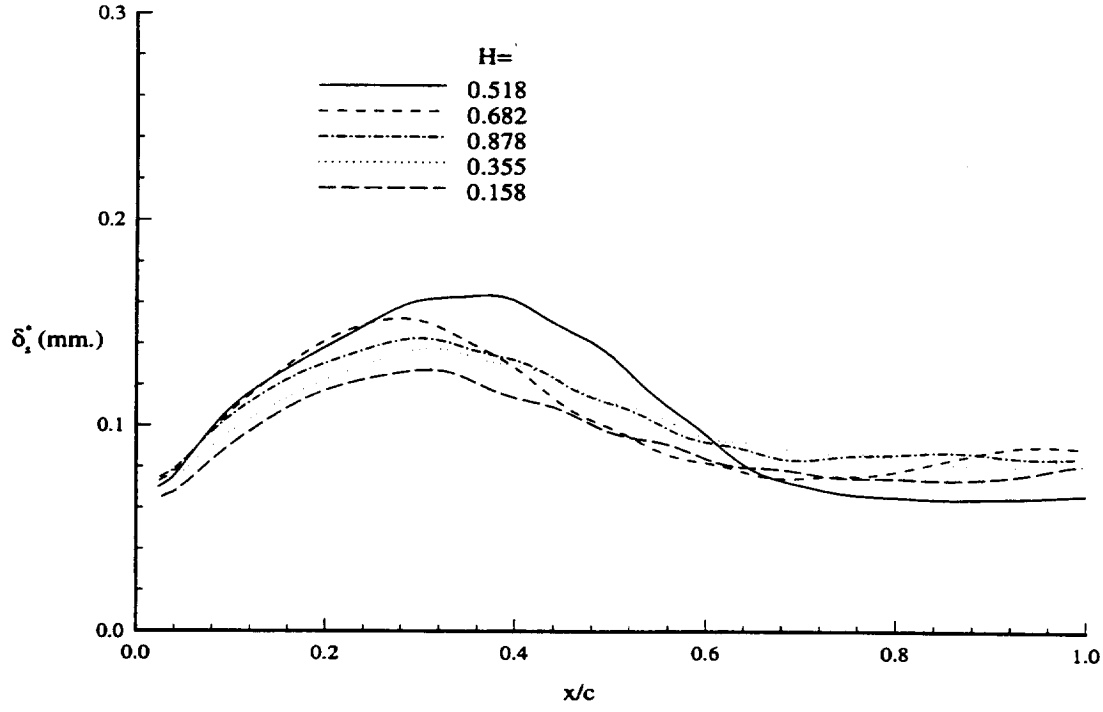

a)

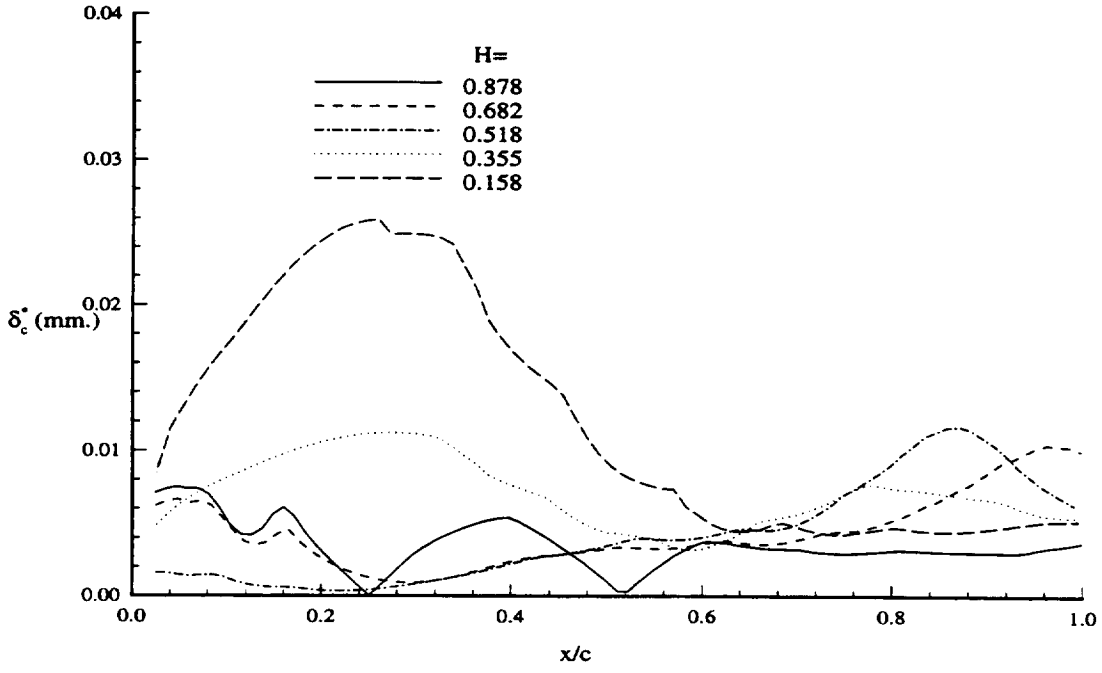

b)

Figure 4. 14 Predicted displacement thickness on pressure surface. a) Streamwise, b) Crosswise

at midspan, x/c=0.3 at H=0.158, etc.), the boundary layer thickness decreased due to the presence of a favorable pressure gradient. In the endwall regions, the boundary layer thickness increased again toward the trailing edge.

The computed momentum thickness in the crosswise direction (θ_c) (Figure 4.13b), is much smaller than the θ_s indicating small cross flow near the pressure surface. The influence of the hub wall boundary layer at the leading edge increased the calculated momentum thickness in the streamwise direction (H=0.158) up to x/c=0.25. Further downstream of this location, the favorable pressure gradient and thinning of the hub boundary layer in the downstream direction decreased the crossflow. The predicted displacement thickness in the streamwise (Figure 4.14a) and crosswise (Figure 4.14b) directions exhibited similar trends as the momentum thickness, increasing at the leading edge to a local maximum, and then tapering off to a fairly constant level toward the trailing edge.

The large curvature of the pressure surface, occurring in the region x/c=0.2 through x/c=0.45, increased the integral boundary layer properties in this region. Down stream of this location, the favorable pressure gradient and absence of blade curvature decreased the boundary layer integral properties thickness'.

In general the three dimensionality of the boundary layers along the pressure surface are much lower than that on the suction surface. Most of the deviations from two dimensional boundary layers occur in the leading edge region due to the dominant

curvature effects. One interesting feature of the computation is the increase in the crosswise flow momentum and displacement thickness in the hub region.

4.3.3 Hub and Casing Endwall Surface Prediction

The prediction of the boundary layer properties on the endwall surfaces proved to be much more difficult than the predictions on the blade surfaces. The major difficulty is in accurately specifying the required inflow velocity distribution, and the presence of a low pressure region associated with the secondary flow, which is beyond the scope of the boundary layer assumption.

For the computation of the endwall surfaces, the edge velocities on the suction and pressure surface boundaries are assumed to be tangent to the local streamlines (i.e. no cross wise flow). The boundary layer solution was started using a local similarity solution to account for the turbulent boundary layer present upstream of leading edge. The solution became unstable at approximately x/c=0.6 on both endwall surfaces. The skin friction coefficient started to oscillate wildly, especially on the casing endwall. The reason for this instability is due to the fact that negative velocities are predicted by the code requiring an implicit step in the computation. The computation scheme described earlier, can perform the implicit step as long as the stability criterion for the finite difference equations is satisfied. In the case of the endwall flow computation, this criterion could not be satisfied even with much finer grids.

In view of this instability, no attempt at this time is made to present and interpret these predictions near the endwall.

CHAPTER 5

THREE-DIMENSIONAL BOUNDARY LAYER MEASUREMENTS IN NOZZLE PASSAGE

Measurement of the boundary layer properties and secondary flow characteristics in the nozzle passage were performed using a two sensor hot wire probe described in Chapter 2. Measurements were taken at various stations along the blade passage at two different axial stations. The measurement locations are shown in Table 5.1. All measurements were taken with the plane of the sensors oriented parallel to the surface with the transformation from the probe coordinate (see Figure 4.1 and 5.1) system (x_p,y_p,z_p) in to the cylindrical turbine coordinate system (x,θ,r) being:

$$\begin{aligned} V_x &= (U_p \cos\alpha_p + V_p \sin\alpha_p)\cos\beta_p - W_p \sin\beta_p \\ V_\theta &= (U_p \cos\alpha_p + V_p \sin\alpha_p)\sin\beta_p + W_p \cos\beta_p \\ V_r &= V_p \cos\alpha_p - U_p \sin\alpha_p \end{aligned} \tag{5.1}$$

The angles α_p and β_p are the angles of the hot wire probe coordinate system relative to the turbine coordinate system in the yaw and pitch direction respectfully. The orientation of the probe during calibration is shown in Figure 2.2. The measurements presented in Chapter 5 are all accomplished by orienting the probe parallel to the surface at all stations in the nozzle blade passage (Figure 4.1 includes the orientation of the probe on the blade pressure surface. The velocity components measured in the probe coordinate system (U_p, V_p, W_p), are defined as: U_p and V_p in the plane of the crossed wires, W_p normal to the plane of the wires. The normal component of velocity is assumed to be equal to zero

Table 5. 1 Hot Wire Measurement Locations

Suction Surface (x/c_m=0.85) H	Casing Surface (x/c_m)=0.85 S	Hub Surface (x/c_m=0.94) S	Pressure Surface (x/c_m)=0.945 H
0.05	0.065	0.416	0.05
0.10	0.088	0.554	0.10
0.20	0.132	0.740	0.30
0.30	0.179	0.786	0.50
0.50	0.219	0.832	0.70
0.70	0.439	0.878	0.90
0.80	0.702	0.924	0.95
0.825	0.833		
0.85	0.877		
0.875			
0.9			
0.95			

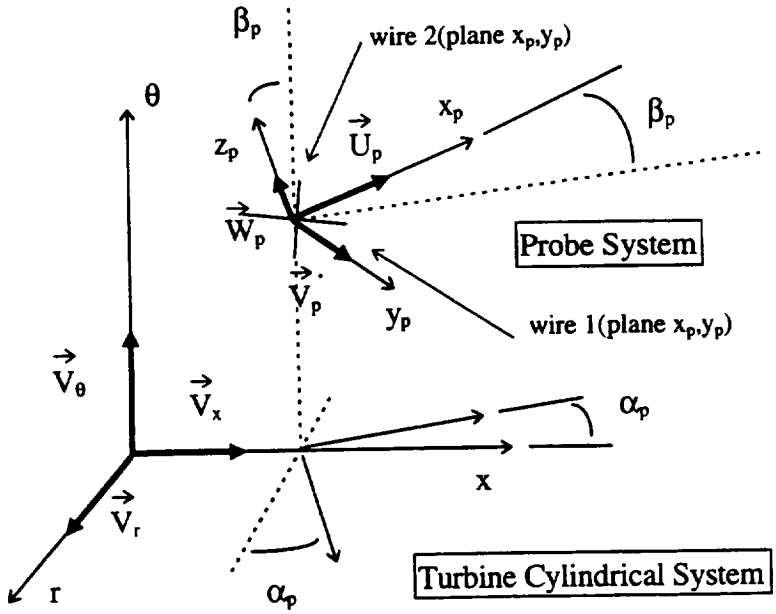

Figure 5. 1 Transformation of probe coordinate system to turbine cylindrical coordinate system. The probe plane is defined by plane (x_p,y_p) at the surface parallel with plane (s,c).

(W_p=0) since the probe is oriented parallel to the surface and Equ. 5.1 becomes:

$$V_x = U_p \cos\alpha_p \cos\beta_p + V_p \sin\alpha_p \cos\beta_p$$
$$V_r = -U_p \sin\alpha_p + V_p \cos\alpha_p \qquad V_\theta = U_p \cos\alpha_p \sin\beta_p + V_p \sin\alpha_p \sin\beta_p \tag{5.2}$$

The two sensor hot wire probe was able to resolve instantaneous velocities in two directions within the boundary layer region. Outside of this region, where the velocity normal to the surface is no longer zero, the measurement obtained correct total velocity measurements but the individual resolved components are no longer accurate.

The data acquired was sampled at a 10 kHz sampling frequency with an low pass filter set at 9.7 kHz to avoid aliasing from the higher frequencies. Simultaneous acquisition of two channels was accomplished using an data acquisition board that used the computer memory as storage. The data was averaged over a 25.6 sec. interval to allow accurate averaging of the flow properties.

5.1 Time Averaged Measurements in Nozzle Passage

Using the method described earlier measurements in the nozzle passage where obtained at selected locations. These could be resolved into total, axial, tangential and radial velocity components where applicable. In general the time averaged measured velocity (V or $\overline{V}$) can be obtained from:

$$V = \overline{V} = \frac{1}{N}\sum_{i=1}^{N} V_i \tag{5.3}$$

where N is the number of measurements and V_i is the instantaneous measured velocity.

5.1.1 Suction Surface Boundary Layer (x/c_m=0.85)

Along the suction surface, the data were taken at 12 radial stations (see Table 5.1). A tangential survey was accomplished by traversing the probe toward the surface. At the moment of contact an electrical connection was established and the surface location was recorded. The results of this survey are presented in Figures 5.2 through 5.6. All velocities are normalized by the upstream axial velocity V_{x1}. S is the normalized blade to blade distance with S=0.0 corresponding to the blade suction surface and S=1.0 corresponding to the blade pressure surface.

In Figure 5.2, the measured free stream total velocity V uniformly decreases from a maximum in the hub region to a minimum near the casing region due to the presence of the radial pressure gradient. Measurements indicate a nearly inviscid flow over most of the blade passage (H=0.1 through 0.7) with a very thin boundary layer region (≈2% of blade spacing). The calculated inviscid surface velocity derived from the measured static pressure distribution, shown in Figure 5.2, compares well with the hot wire data in the free stream. The boundary layers in this region are three dimensional and are pressure driven.

Appreciable boundary layer growth and deviation from typical blade boundary layer profiles occur only in regions close to the endwalls due to secondary flow. These interaction regions are near the hub (H=0.05) and from H=0.8 to 0.95 near the casing. The influence of the secondary flow at H=0.05 results in a large increase in the radial angle (39.5°) at the surface (Fig. 5.3), indicating strong radial outward flow along the blade

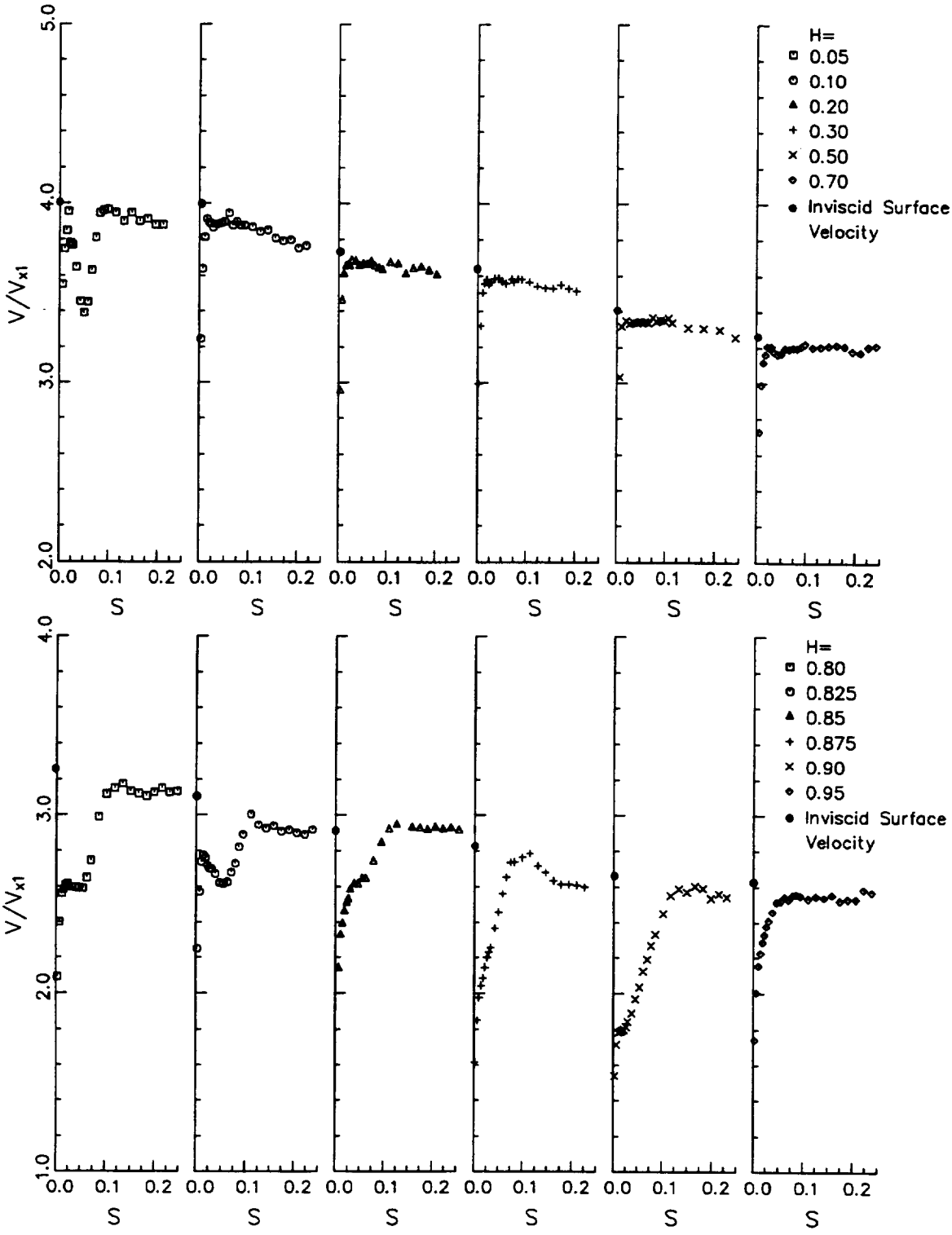

Figure 5. 2 Measured Total Velocity ($V=\sqrt{V_x^2 + V_r^2}$) on Suction Surface. Top plot - hub surface to H=0.7, Bottom plot - H=0.8 to casing surface .

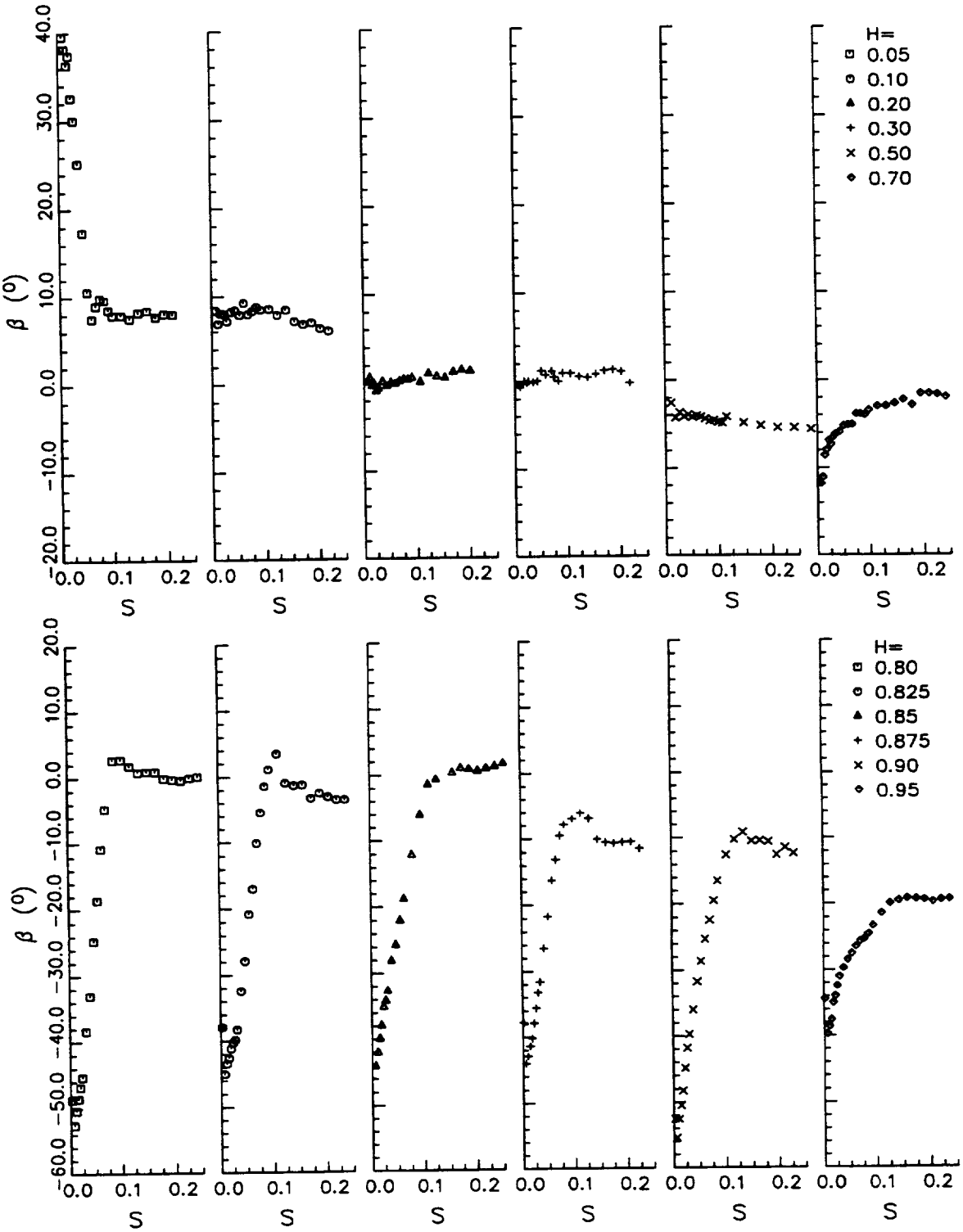

Figure 5. 3 Radial Angle (β) Measurement on Suction Surface (x/c_m=0.85). Top plot - hub surface to H=0.7, Bottom plot - H=0.8 to casing surface. Positive β is radialy outward.

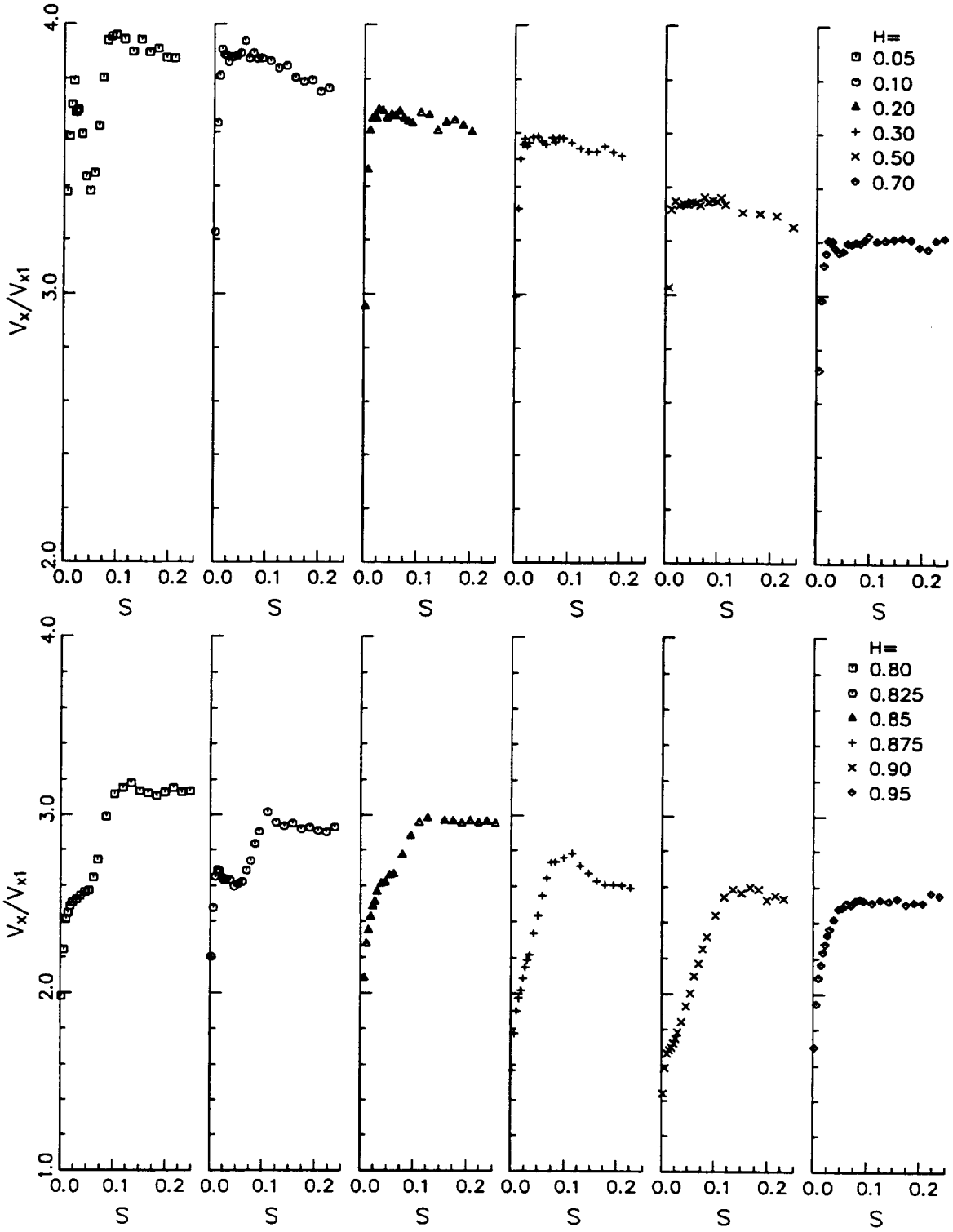

Figure 5. 4 Measured Axial Velocity Component (V_x/V_{x1}) on Suction Surface of Nozzle Vane (x/c_m=0.85). Top plot - hub surface to H=0.7, Bottom plot - H=0.8 to casing surface.

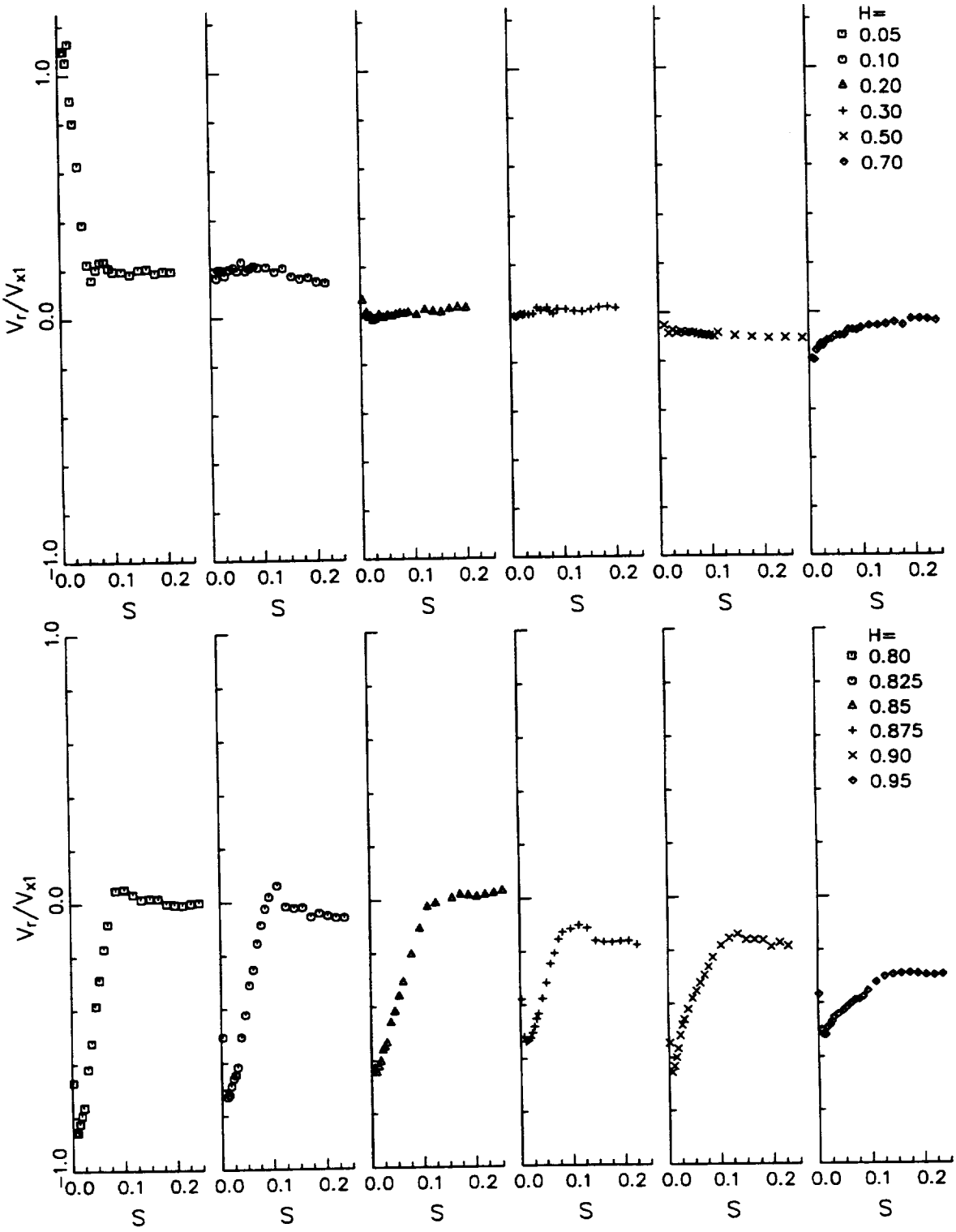

Figure 5. 5 Radial Velocity (V_r/V_{x1})Distribution Along Suction Surface (x/c_m=0.85). Top plot - hub surface to H=0.7, Bottom plot - H=0.8 to casing surface. Positive V_r is radialy outward.

suction surface. The existence of a dip in the measured total velocity profile close to the surface (Fig. 5.2) is an indication of the hub-suction passage vortex. This is also indicated by a similar feature in the radial flow angle at H=0.05 location.

In the casing suction corner (Fig. 5.2), the center of the passage vortex is located approximately at H=0.825 indicated by reversal of the radial velocity at S=0.125 as well as by the perturbed boundary layer, indicated in Figure 5.5. The vortex region extends from H=0.8 to the H=0.90, where the secondary flow, blade and casing boundary layer interaction occurs. In the regions influenced by secondary flow, the total and axial velocity decreases and this can be clearly seen in Figures 5.2 and 5.4. The strongest influence can be seen at the H=0.825 location, indicating close proximity to the vortex core. The increase in the measured radial angle or overshoot at the H=0.825 location is due to reversal of radial flow across the vortex, even though the magnitude of outward velocity is small. The location closest to the casing endwall surface (H=0.95) is completely within the viscous layer of the endwall surface (indicated by an increase in turbulence intensity discussed later).

The measured axial velocity (V_x) decreases in the freestream in a fashion similar to the total velocity (Figure 5.2). In the secondary flow region the axial velocity decreases due to the presence of secondary flow and the vortex.

The velocity hodograph plot for selected locations, shown in Figure 5.6 (V_c and V_s are the crosswise and streamwise velocity components, V_{edge} is the boundary layer edge velocity Figure 5.2), indicates large variations in regions influenced by the secondary flow,

a)

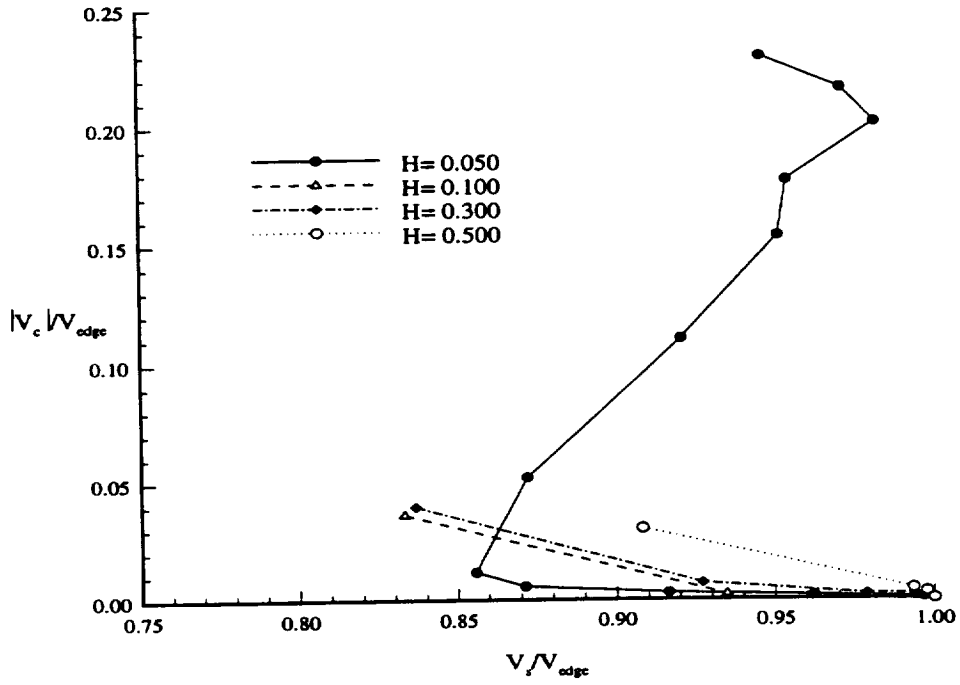

b)

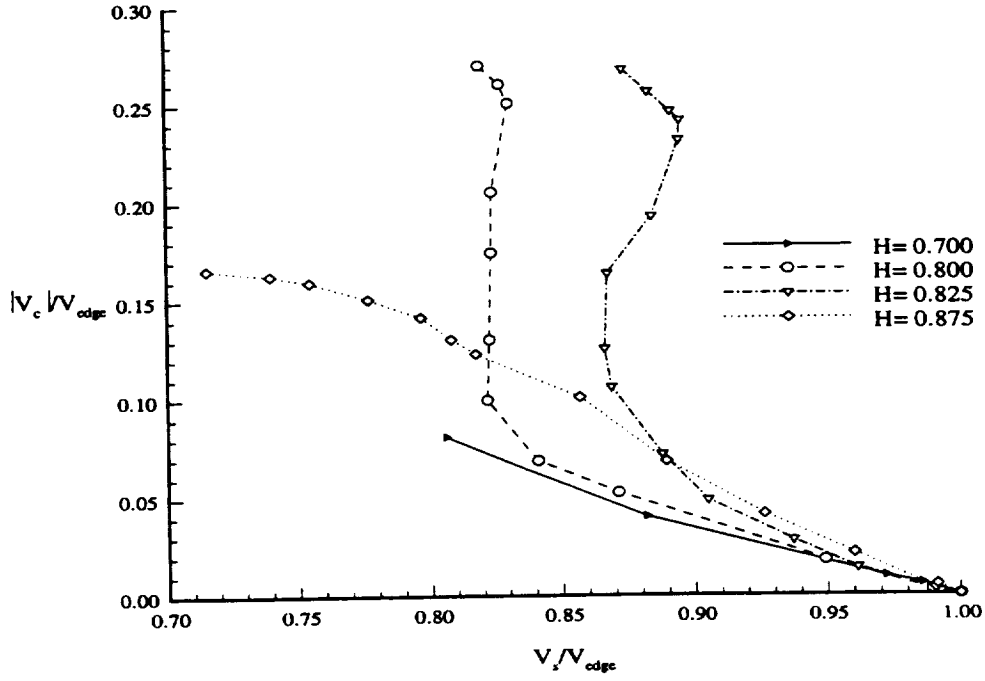

Figure 5. 6 Hodograph plot on suction surface at x/c_m=0.85. a)Hub, b)Casing region. V_s- streamwise, V_c-crosswise, and V_{edge}-edge velocity.

especially at H=0.05 and in the casing corner passage vortex region. The velocity component in the crosswise direction increases dramatically (H=0.05, 0.8, 0.825) when compared to the typical three dimensional boundary layer distribution in the mid passage region (H=0.1 and 0.7). The influence of the passage vortex near H=0.825 (Figure 5.6b) can clearly be seen in the dip in the streamwise velocity component while the cross wise velocity is still appreciable. The measurement locations at H=0.7 and 0.875 do not exhibit a strong influence of the passage vortex.

The flow is radialy inward over most of the blade surface (Figure 5.3), extending from H=0.3 to the tip of the blade, with maxima occurring at H=0.80 where the radial flow angle close to the surface has a value of -52°. The result is consistent with the flow visualization experiments presented in Chapter 3 indicating that the radial pressure gradient dominates the flow field along the suction surface at the trailing edge location. The three dimensionality in the boundary layer is present only in the secondary flow region located in the casing corner (H=0.8 to 0.95) and in the hub region at H=0.05. The boundary layers are nearly two dimensional over most of the blade surface (from H=0.1 to 0.7).

The data clearly reveals the effect of interaction between the casing boundary layer with the secondary flow. The secondary flow region produces a defect in total, axial, and tangential velocity resulting in a wake type of velocity profile in the buffer region of the boundary layer. The maximum defect in total velocity caused by the secondary vortex and flow is found to be as high as 20% of the free stream velocity, indicating the presence of a

strong vortex.

5.1.2 Casing Surface Boundary Layer (x/c_m=0.85)

Boundary layer data on the casing surface at x/c_m=0.85 are shown in Figures 5.7 through 5.10. The measurements were performed at nine locations across the passage, including locations inside the secondary flow region of the suction-casing corner. The total velocity measured near the casing surface is shown in Figure 5.7. Outside the boundary layers and the secondary flow regions, the total velocity increases uniformly toward the inner radius due to the presence of radial pressure gradient. Comparison between the calculated inviscid surface velocity derived from the blade static pressure distribution (Figure 3.3a) and the extrapolated velocities from the hot-wire data (assuming a linear velocity profile) are found to be very good. The blade to blade pressure gradient is responsible for the decrease in total velocity from the suction surface (S=0.0) toward the pressure surface. The total velocity profiles at S=0.065 through 0.219 again indicate wake like velocity profiles in the secondary flow regions due to a decrease in total velocity in the passage vortex core as explained earlier. At two measurement locations (S=0.132 and 0.175), in the near wall region, the measured total velocity increases due to the interaction of the passage vortex and the endwall boundary layer.

The measurement location positioned closest to the passage vortex core is located at S=0.132. This is apparent from the large wake like velocity deficit compared to the free stream. Measurements in the mid-passage region (S=0.439) and close to the pressure

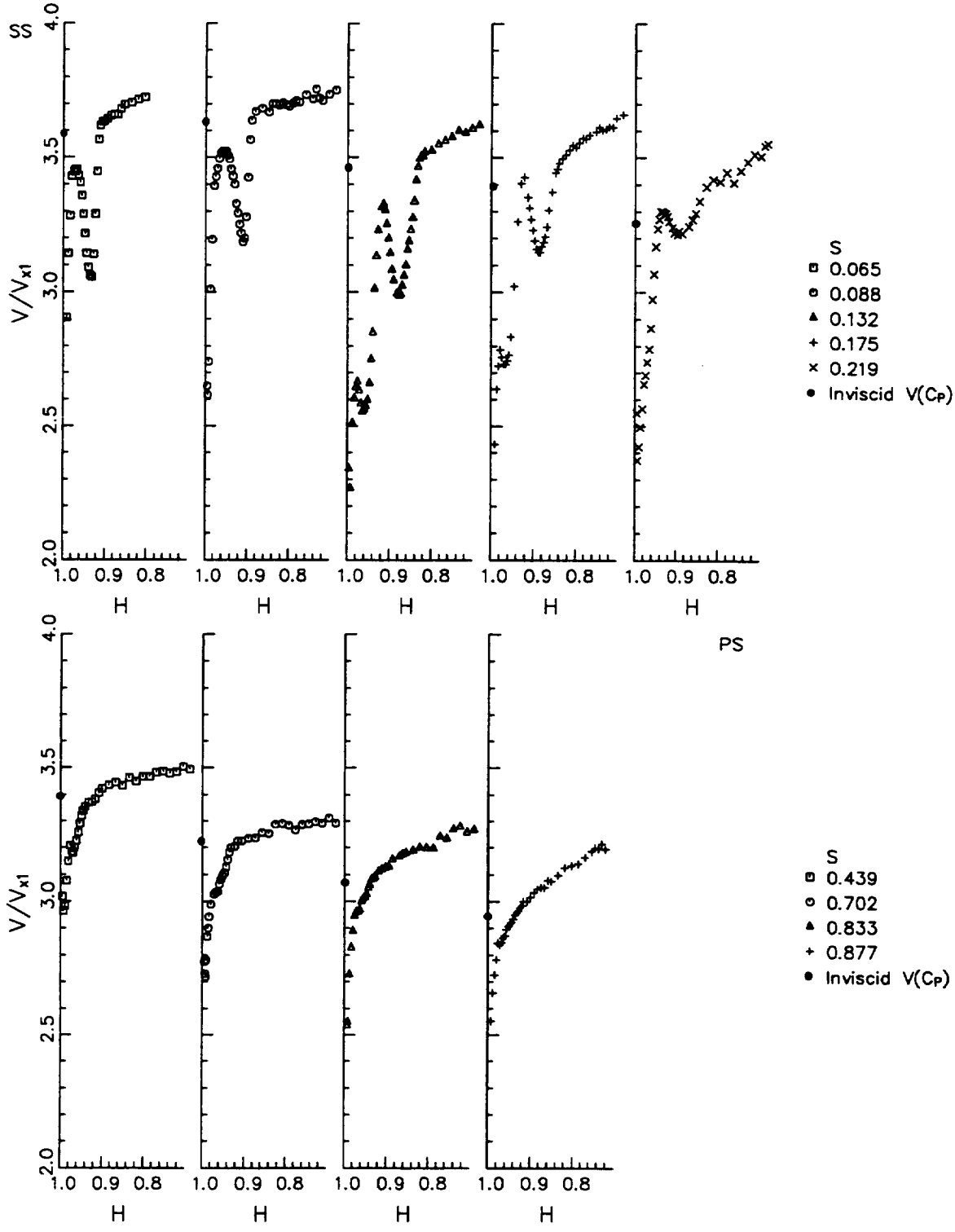

Figure 5. 7 Measured total velocity (V/V_{x1}) where $V = \sqrt{V_x^2 + V_\theta^2}$, on the Casing surface at x/c_m=0.85. SS - Suction surface (S=0.0), PS - Pressure surface(S=1.0).

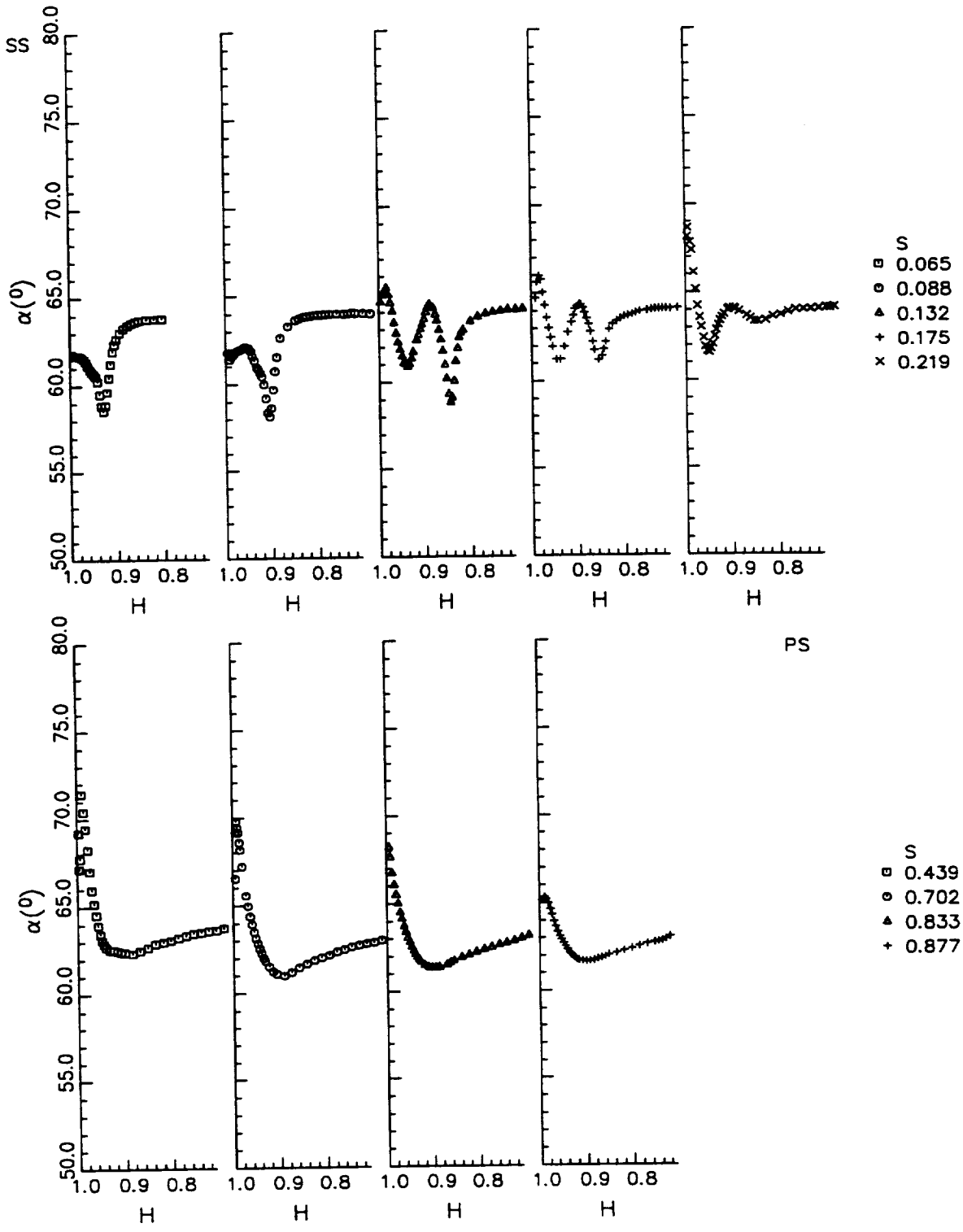

Figure 5. 8 Measured Tangential Angle or Cross Flow (α) on the Casing Surface at x/c_m=0.85. SS - Suction surface(S=0.0), PS - Pressure surface(S=1.0).

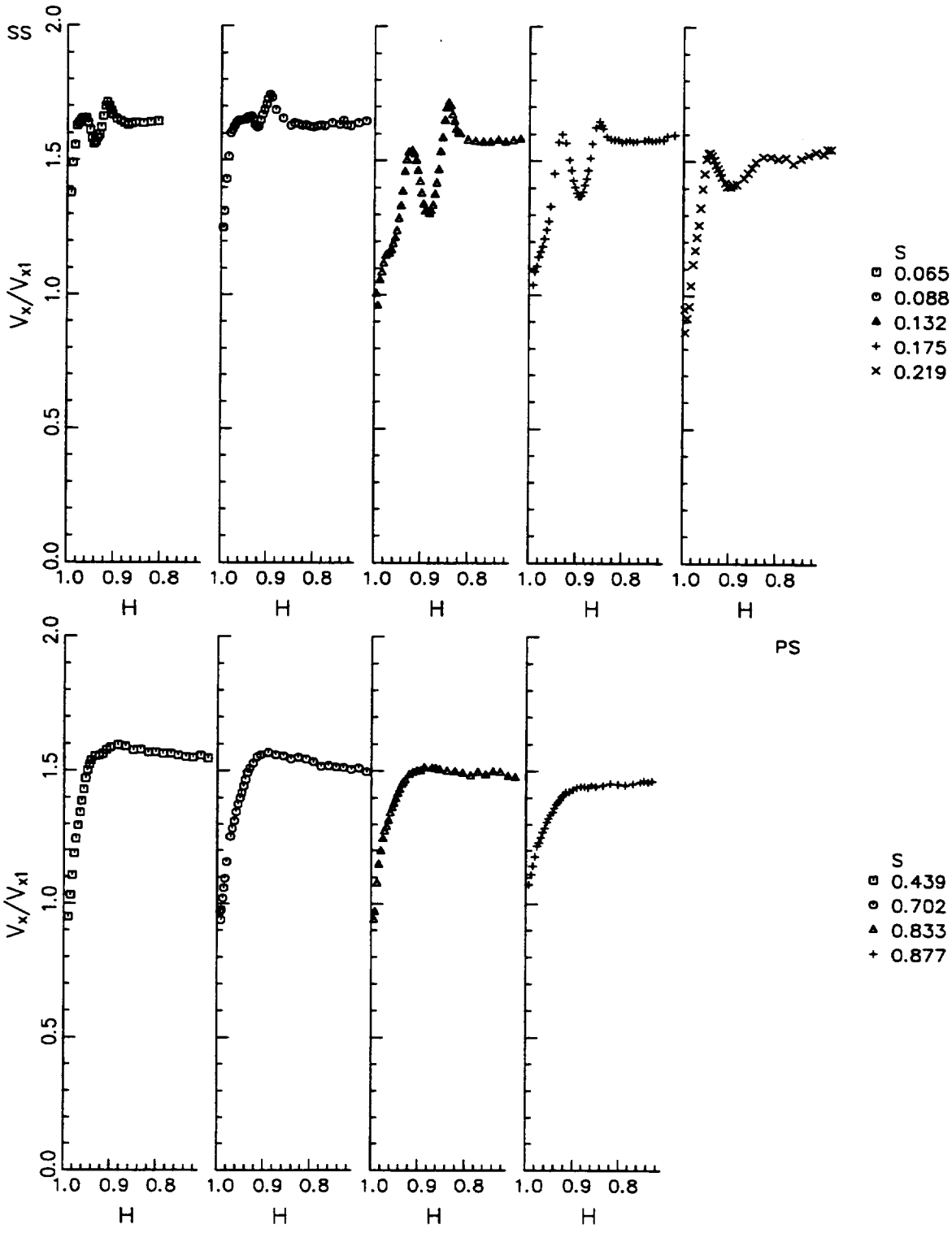

Figure 5. 9 Axial Velocity (V_x/V_{x1}), Casing Surface at x/c_m=0.85. SS - Suction surface (S=0.0), PS - Pressure surface (S=1.0).

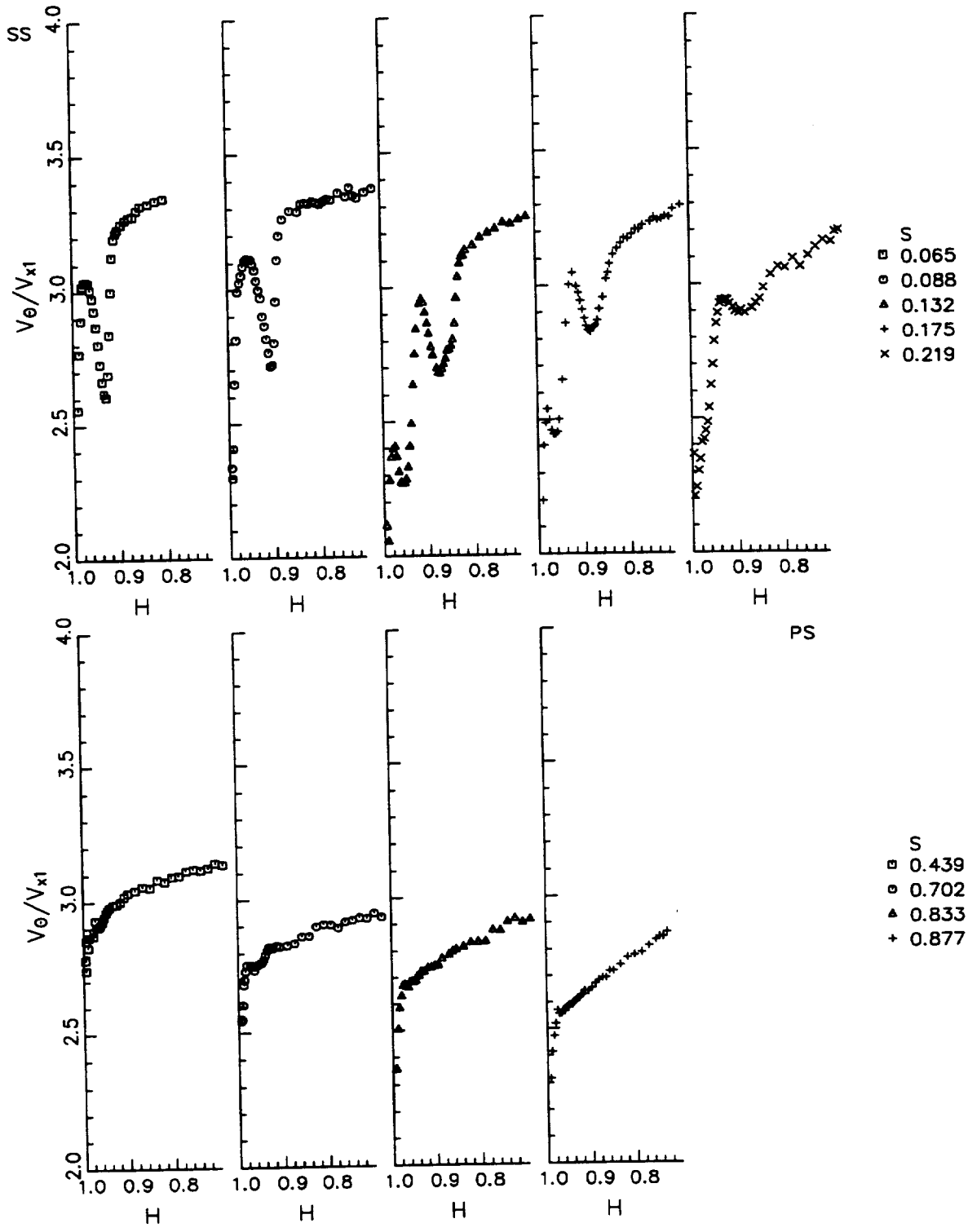

Figure 5. 10 Measured Tangential Velocity (V_θ/V_{x1}) on Casing Surface at x/c_m=0.85. SS - Suction surface (S=0.0), PS - Pressure surface (1.0).

surface (S=0.702 to 0.877) of the blade indicates conventional three dimensional boundary layer characteristics. The boundary layer thickness is largest near the suction surface and decreases toward the pressure surface of the blade reaching a minimum at S=0.877. Measurements closer to the pressure surface could not be accomplished due to accessibility.

The measured cross flow angle α, Figure 5.8, increases dramatically in the near wall region from approximately 61° to a maximum of 72° at the S=0.439 location. The increase is due to the turning of the boundary layers toward the suction surface caused by the strong transverse pressure. The crossflow velocity decreases at locations closer to the pressure surface corner. The underturning caused by the passage vortex is as much as 6° at the S=0.132 location. In the boundary layer close to the casing surface the crossflow angle increases toward the suction surface. The influence of the passage vortex is dominant in the region S=0.065 to 0.219 with maximum influence occuring near S=0.132.

At the edges of the passage vortex, the local axial velocity increases (Figure 5.9, S=0.088 through 0.175) from the freestream value. The measured axial velocity decreased in the vortex core, increased again on the casing side of the vortex and finally decreased in the viscous layer close to the endwall.

The measured tangential velocity (V_θ) presented in Figure 5.10, indicates similar behavior as the measured total velocity shown in Figure 5.7. The tangential velocity distribution indicates that the flow turning is smaller toward the pressure surface corner. The measurements aquired in the casing-suction corner and on the suction surface are

combined to generate contour plots of total velocity, total turbulence, and radial angle, and this is covered in section 5.5.

5.1.3 Hub Surface Boundary Layer (x/c_m=0.94)

Due to poor accessibility, measurements on the hub endwall surface were restricted to locations from S=0.416 to S=0.924, which are well away from the secondary flow regions. The measurements at the x/c_m=0.94 are shown in Figures 5.11, 5.12, 5.13, and 5.14.

In general, the measurements reveal the general characteristics of three dimensional boundary layers, with a very thin viscous region compared to those on the casing endwall surface. Measurements of the total velocity ($V = \sqrt{V_x^2 + V_\theta^2}$) shown in Figure 5.11 indicate very thin boundary layers. The boundary layer thickness decreases as the pressure surface (S=1.0) is approached. The boundary layer thickness on the hub surface is much lower than that on the casing surface (more than 50% lower outside of the secondary flow region). The total velocity just outside the viscous region increases by approximately 4% from the free stream value (at the mid span measurement locations, S=0.416 and 0.554).

The measured crossflow angle α (Figure 5.14) changes rapidly in the near wall region. The angle increases dramatically in the mid passage region (by as much as 14° at

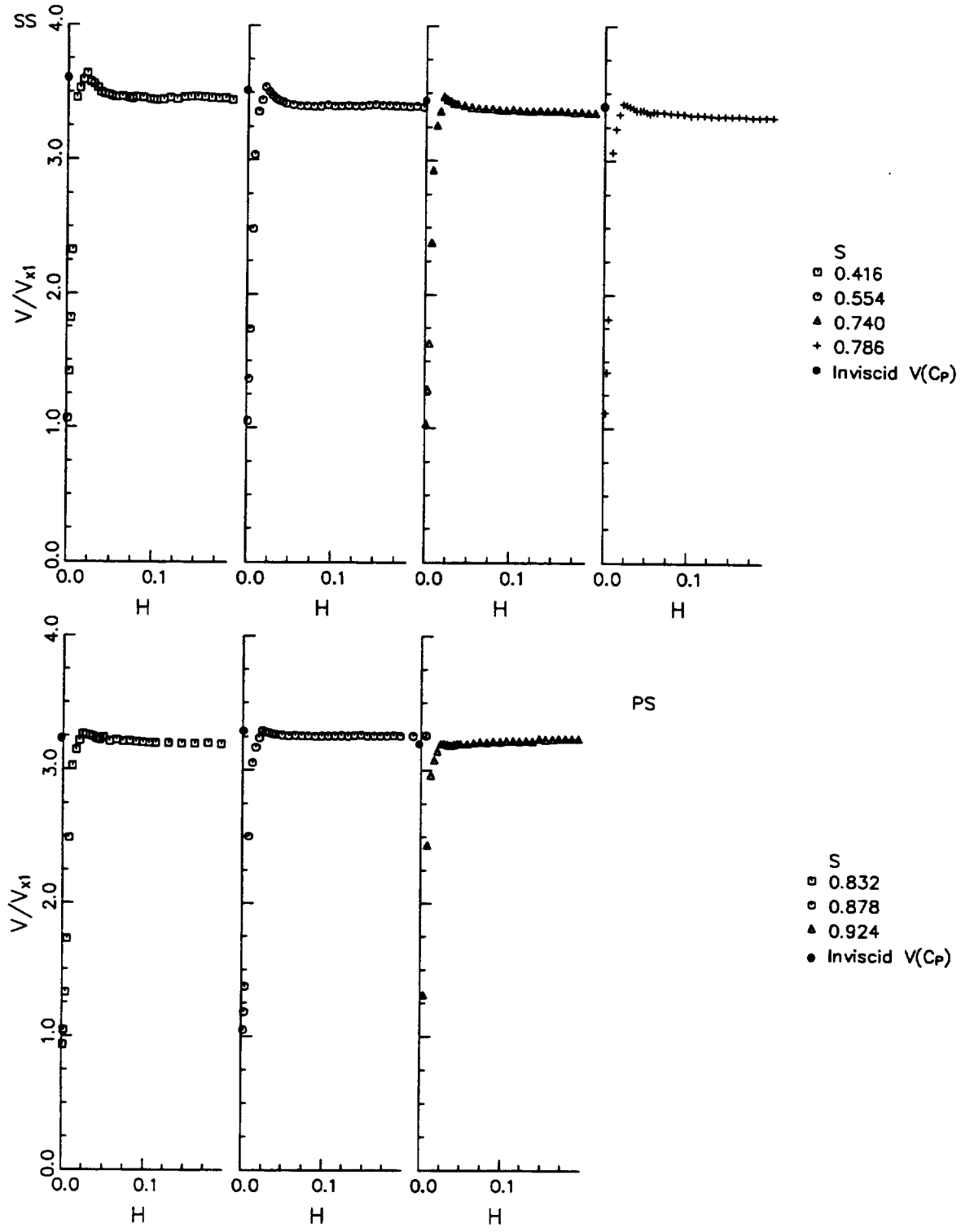

Figure 5. 11 Measured Total Velocity (V/V_{x1}) on Hub Surface at x/c_m=0.94. SS - Suction surface (S=0.0), PS - Pressure surface (S=1.0).

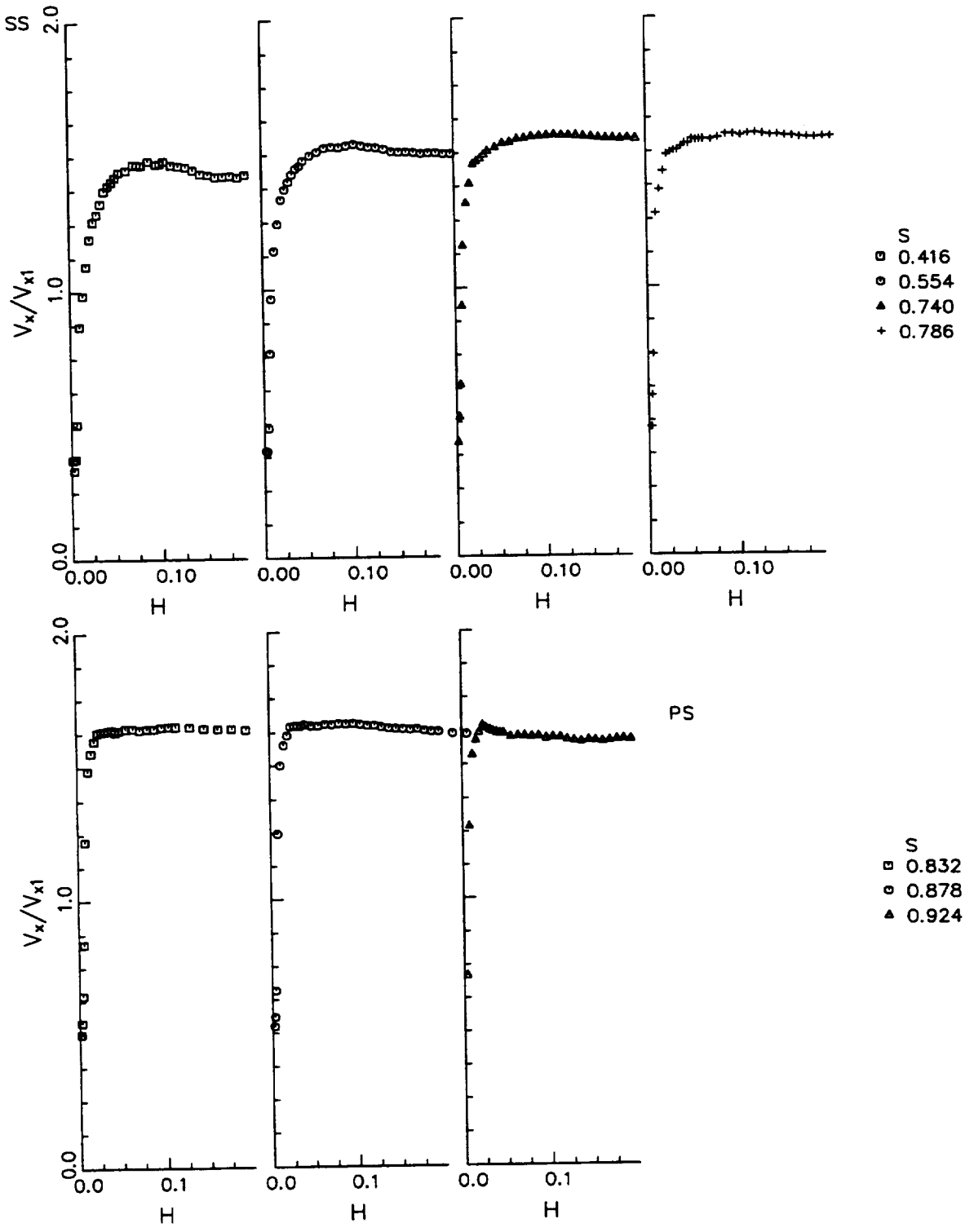

Figure 5. 12 Measured Axial Velocity (V_x/V_{x1}) on Hub Endwall Surface at x/c_m=0.94. SS - Suction surface (S=0.0) , PS - Pressure surface (S=1.0).

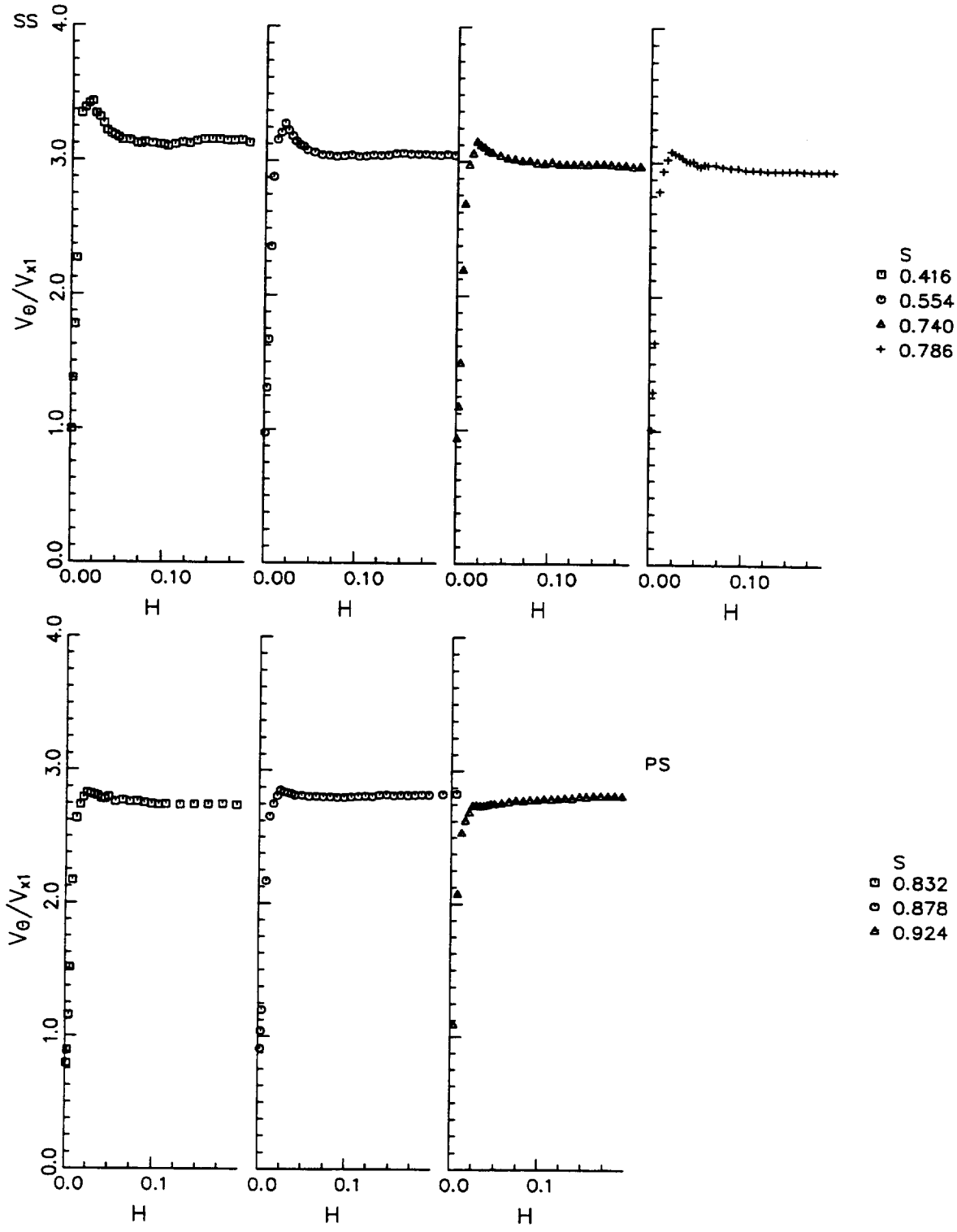

Figure 5. 13 Tangential Velocity (V_θ/V_{x1}) along Hub Endwall Surface at x/c_m=0.94. SS - Suction surface (S=0.0), PS - Pressure surface (S=1.0).

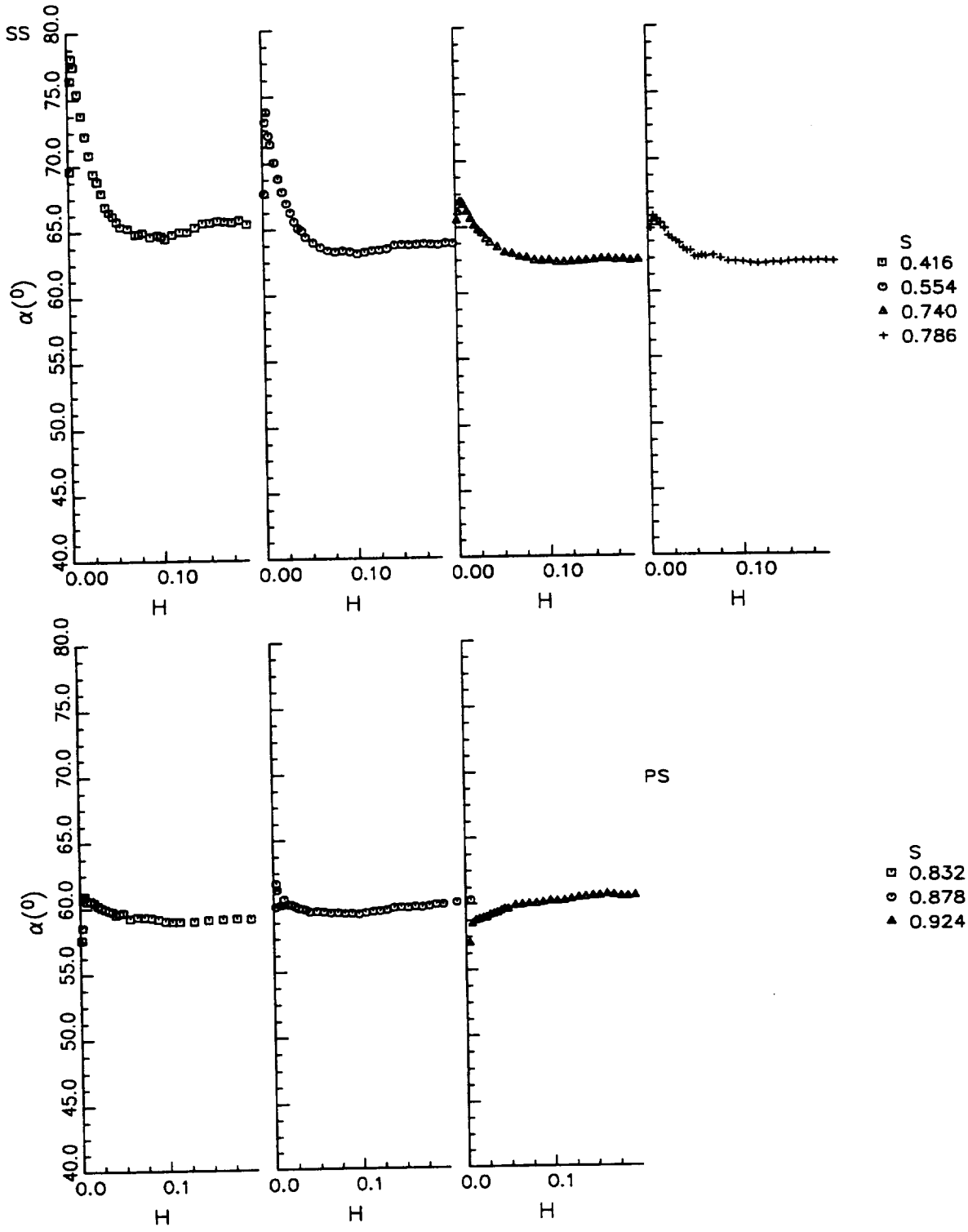

Figure 5. 14 Measured Tangential Angle (α) on Hub Surface at x/c_m=0.94. SS - Suction surface (S=0.0), PS - Pressure surface (S=1.0).

the S=0.416 location) due to the high flow turning toward the hub-suction surface corner caused by a strong transverse pressure gradient. The maximum deviation in the crossflow angle decreases as the pressure surface is approached due to the transverse pressure gradient. The boundary layer thickness and the integral properties of the boundary layer decrease from the suction to the pressure surface corner due to the reasons mentioned earlier. The comparison to predicted values is presented in section 5.2.

The measured tangential velocity distribution, shown in Figure 5.13, indicates a small increase in V_θ from the free stream value in the near wall region. Outside the viscous region V_θ is fairly constant over the measurement range.

The axial velocity profiles shown in Figure 5.12 are very uniform in the free stream, almost constant due to the relatively small static pressure variation in this region. The boundary layers are fairly thick near the mid passage, caused by overturning due to secondary flow. The influence of the secondary flow region, located in the hub-suction corner, can also be seen from the V_θ distribution at S=0.416 (Figure 5.13) indicated by an increase in tangential velocity close to the endwall surface.

In general the hub endwall boundary layers are much thinner than the casing endwall boundary layers due to higher acceleration of the flow at the downstream location (x/c_m=0.94) . Due to accessibility problems measurements in the hub-suction corner could

not be accomplished.

5.1.4 Blade Pressure Surface Boundary Layers at x/c_m=0.945

The measurements were taken at the trailing edge of the blade (x/c_m=0.945) at seven radial stations on the blade pressure surface. The distribution of mean velocities and angles are shown in Figures 5.15 through 5.18. Comparison with the inviscid surface velocity, based on the surface static pressure measurement, agree very well with the extrapolated values from the hot-wire data (Figure 5.15). The measured total velocity distribution increases from the pressure surface toward the suction surface due to the blade to blade pressure gradient. Locations close to the hub endwall indicate a slight increase in the total velocity just outside the viscous region. The local velocity increase is not significant at the mid span and tip locations (from H=0.5 to 0.95). The boundary layer thickness is gradually decreasing toward the tip due to the radial pressure gradient but the variation is much smaller when compared to the suction surface.

The measured radial flow angle variation (Figure 5.16) indicates inward flow inside the boundary layer, which is in agreement with the measurements by Zaccaria et. al. (1993) acquired with a five hole pneumatic probe. The free stream radial angle decreases from -7° at H=0.10 to -3° at H=0.90. Inside the boundary layers the radial inward velocity increases (Figure 5.18), especially in the blade tip region, indicating greater skewing of the

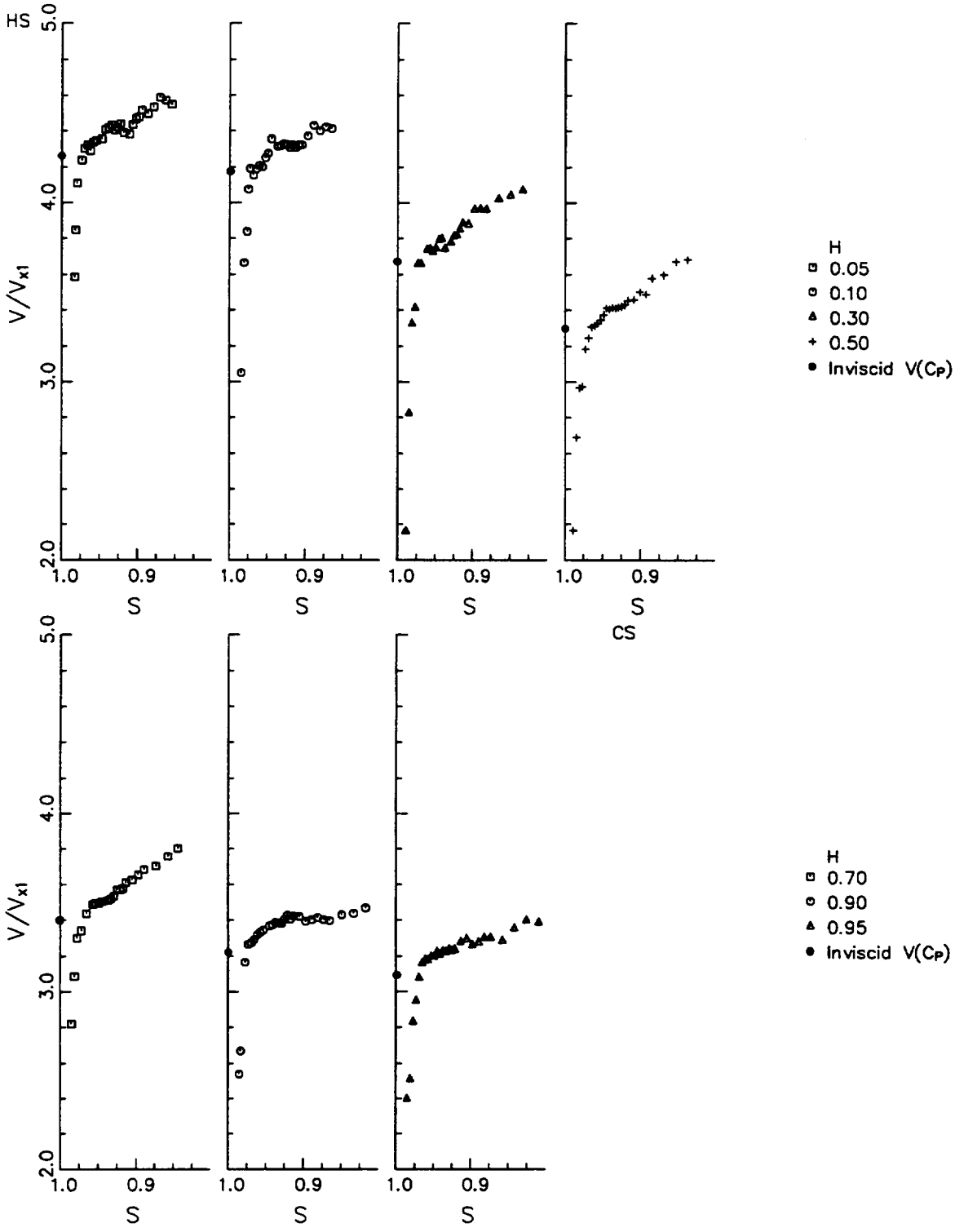

Figure 5. 15 Measured Total Velocity (V/V_{x1}) on Pressure Surface at x/c_m=0.945. HS - Hub surface (H=0.0), CS - Casing surface (H=1.0).

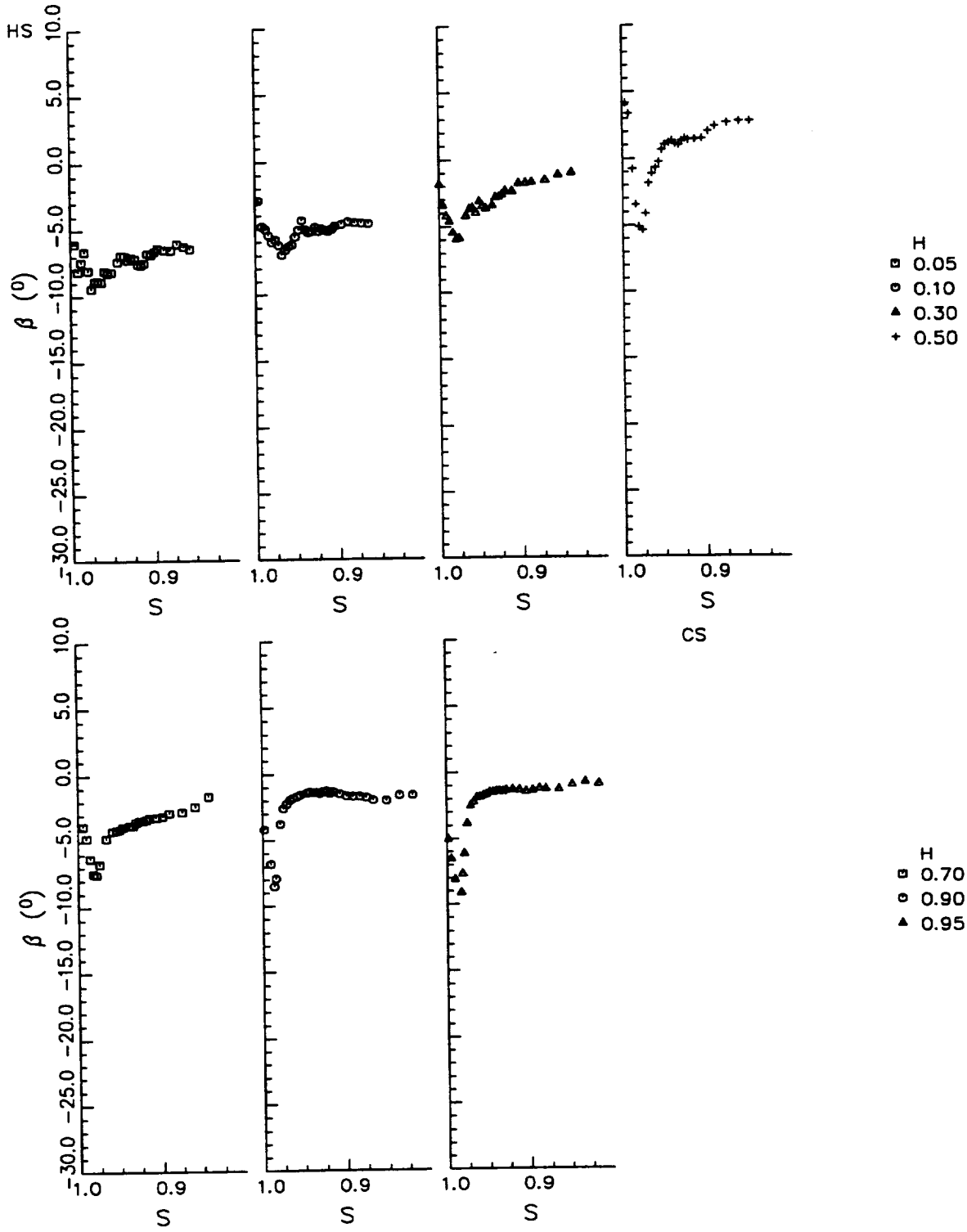

Figure 5. 16 Measured Radial Angle (β) on Pressure Surface at x/c_m=0.945. HS - Hub surface (H=0.0), CS - Casing surface (H=1.0).

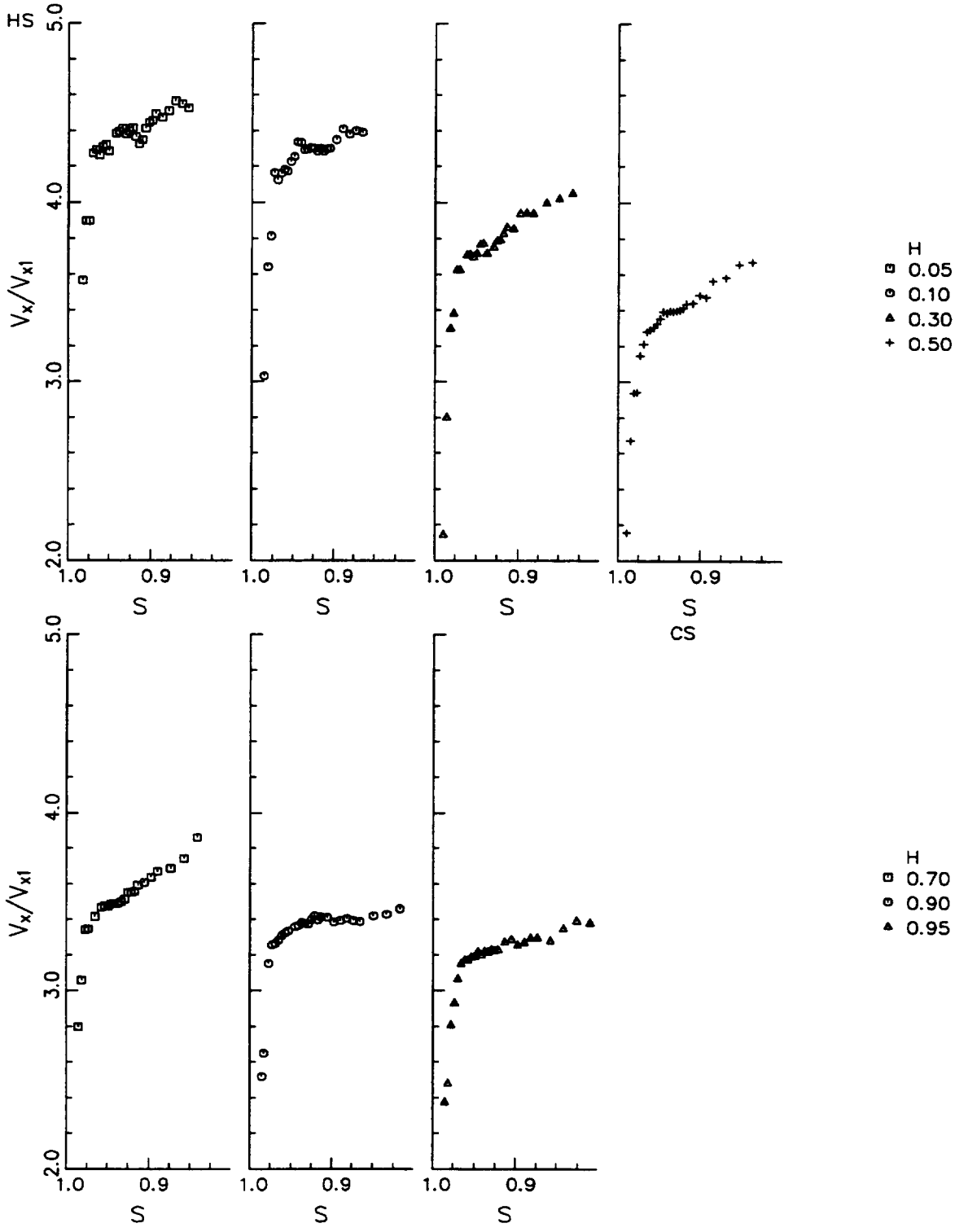

Figure 5. 17 Pressure Surface Axial Velocity (V_x/V_{x1}) Distribution at x/c_m=0.945. HS - Hub surface (H=0.0), CS - Casing surface (H=1.0).

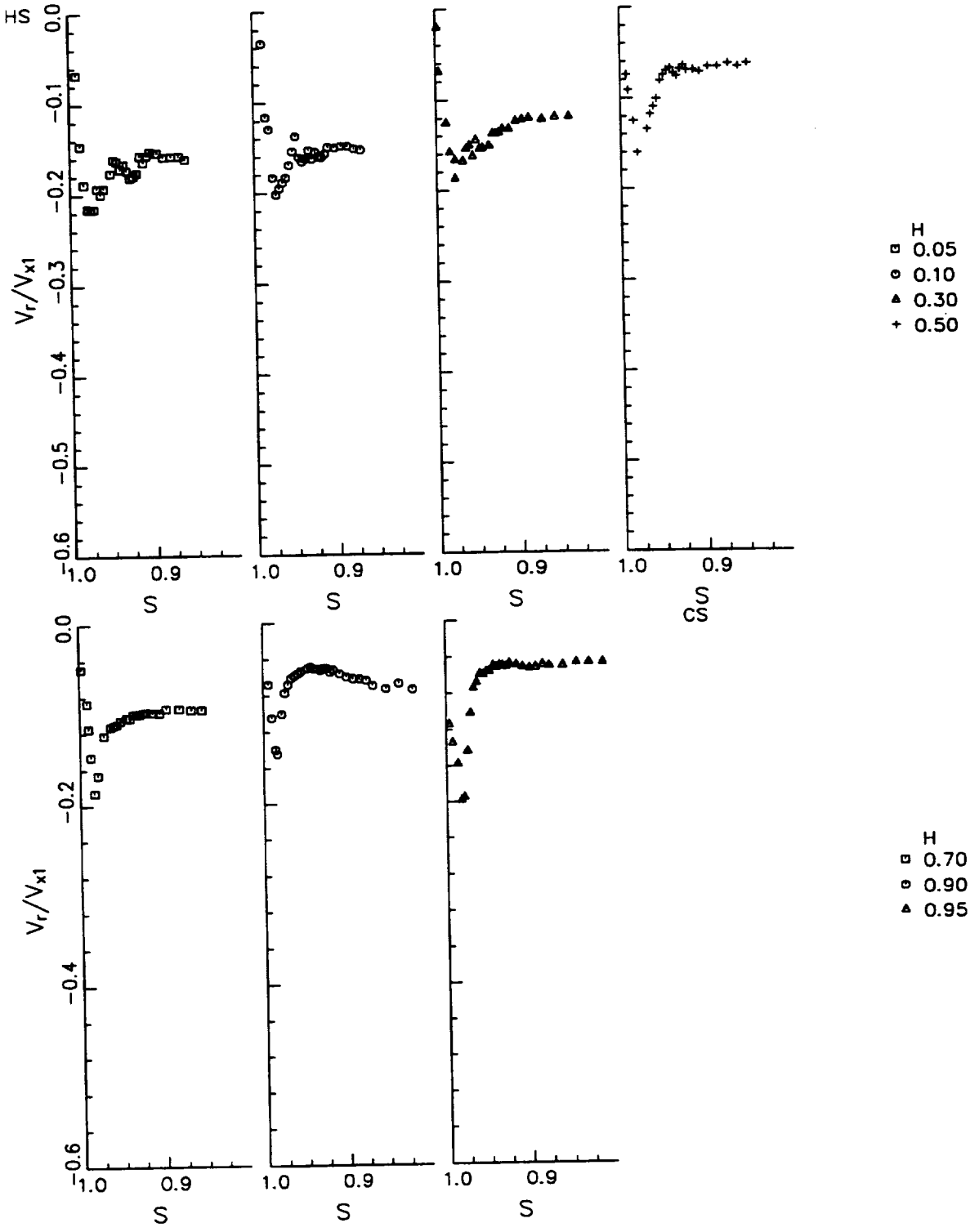

Figure 5. 18 Radial Velocity Measurement (V_r/V_{x1}), Pressure Surface at x/c_m=0.945. HS - Hub surface (H=0.0), CS - Casing surface (H=1.0).

three dimensional blade boundary layers toward the hub. The boundary layer turning is especially strong in the tip region (H=0.9 and 0.95) due to large influence of the casing endwall surface boundary layer. Outside the thin boundary layers the radial angle variation is very small and close to zero. The axial velocity distribution outside of the endwall regions is uniform and typical of turbine blade velocity profiles.

Overall, the pressure surface measurements indicate that the boundary layer thickness is fairly uniform in the spanwise direction. The three dimensionality is mostly due to the radial pressure gradient. The viscous region is very thin (less than 2% of the pitch) and skewed toward the hub endwall, gradually decreasing from the hub to the tip.

The total velocity just outside of the boundary layer region in the hub-pressure surface corner was influenced by the rotor gap and the endwall boundary layers. The boundary layer integral properties and turbulence measurements will also be discussed in the subsequent sections.

5.2 Analysis of Three Dimensional Boundary Layer Data and Comparison with Predictions

Measured velocity profiles presented in the previous section were used to determine the boundary layer integral properties and are compared with predictions from the three dimensional boundary layer code (BL3D) described in section 4.1 and Appendix D. The velocity at the edge of the local boundary layer (V_{edge}) was based on 99% of the extrapolated linear portion of the inviscid velocity profile. In regions of secondary flow, the boundary layer edge was determined by inspection, since a reasonable method of separating the boundary layer viscous region from the secondary flow region does not exist. Comparison of the data with the computation is not accurate in these regions. The following discussion will concentrate on the regions away from the endwall surfaces where three dimensional boundary layers are not influenced by the secondary flow.

5.2.1 Boundary Layer Velocity Profiles

The measured velocity profiles are compared with predictions at a few selected locations along the suction and pressure surfaces in Figures 5. 19 and 5.20. On the suction surface, the computed velocity profiles were specified to be turbulent at the x/c_m=0.85 location (section 4.3.1), based on flow visualization experiments presented in section 3.3. The prediction compares well with the experimental data.

In the cross flow direction (V_c/V_{edge}) (Figure 5.19a, V_{edge} is the velocity at the boundary layer edge) the agreement between data and predictions is quite good (outer regions of the viscous layer) even through there are very few measured points within the boundary layer. The closest measurement location is at $n/\delta \approx 0.4$, H=0.7 where the boundary layer thickness is larger than those at the midspan. Measurements in the near wall regions could not be obtained due to the very small thickness of the viscous layer, but in general the measurements do indicate the validity of the near wall corrections.

The measurements are very close to the predicted value (Figure 5.19b) for the streamwise velocity profile. The measurement closest to the blade surface at H=0.5 is slightly higher than the predicted value (about 3%), but in the outer regions the comparison is much more accurate. The prediction indicates very small variation in the streamwise velocity profiles in the spanwise direction.

Similar agreement is observed on the pressure surface(Figure 5.20), except in the endwall region (H=0.90). Large deviation from the predicted crossflow velocity in the casing - pressure surface corner is due to the influence of the endwall boundary layer. The crossflow velocity is much lower on the pressure surface (less than 5% of V_{edge}) at all measurement locations.

Agreement is good on both surfaces and this demonstrates that the boundary layer procedure described earlier is capturing the blade boundary layer development accurately in regions away from the endwalls. In these regions, the specification of the boundary layer edge conditions is critical.

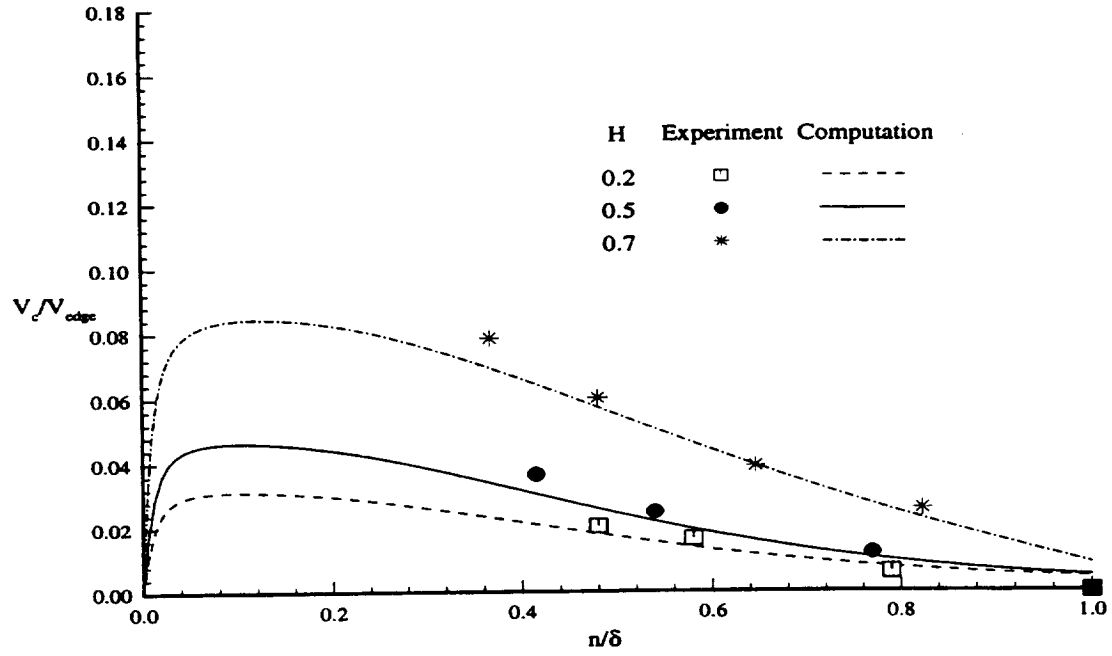

a)

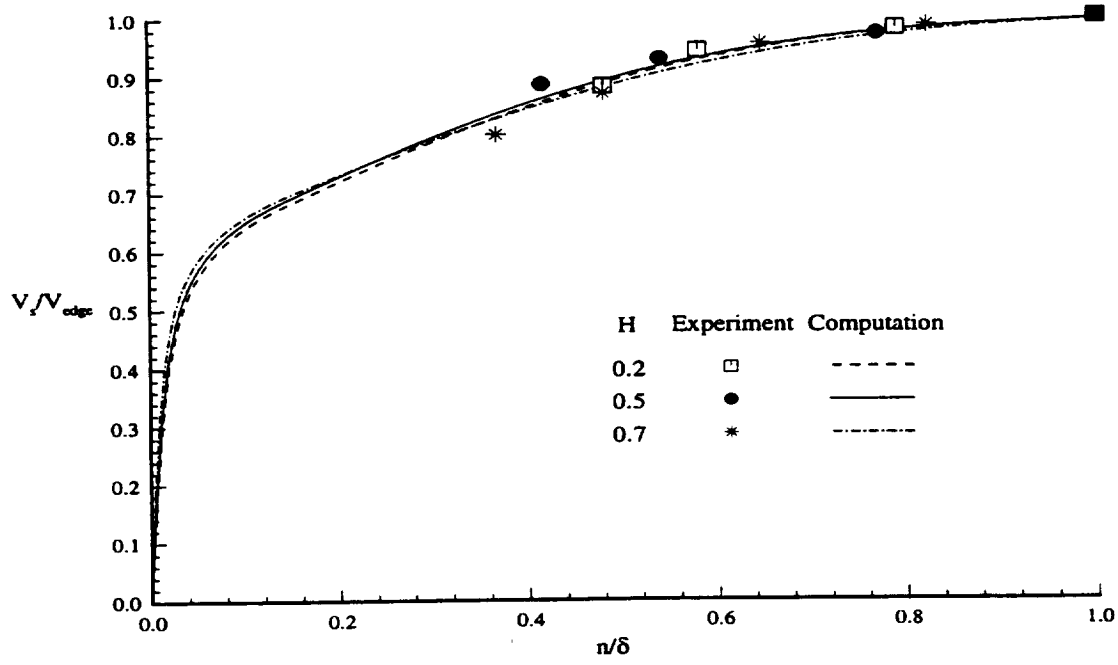

b)

Figure 5. 19 Predicted and Measured Boundary Layer Velocity Profiles on Suction Surface. a) Cross wise (V_c/V_{edge}), b) Stream wise (V_s/V_{edge}), velocity profiles.

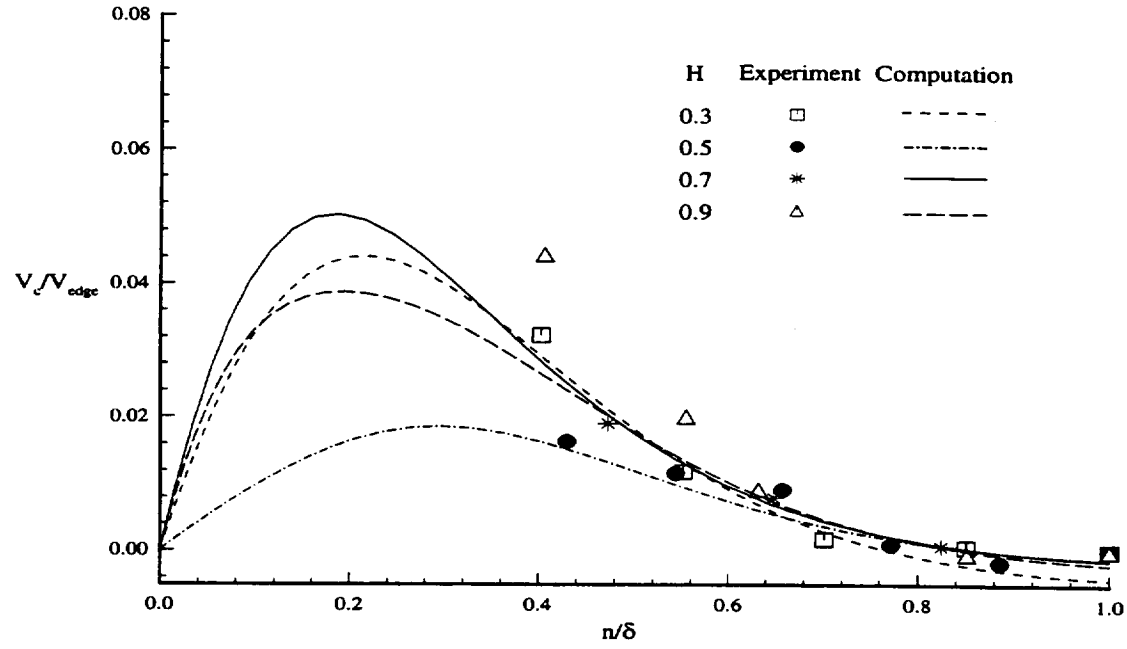

a)

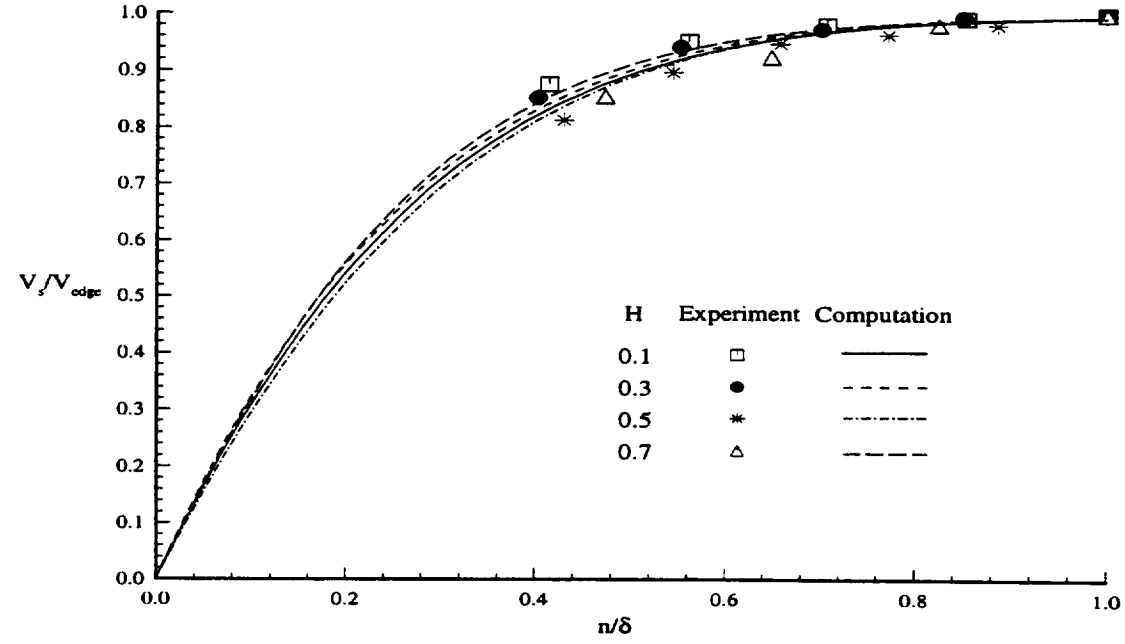

b)

Figure 5. 20 Pressure Surface Predicted and Measured Boundary Layer Velocity Profiles. a)Cross wise (V_c/V_{edge}), b)Stream wise (V_s/V_{edge}), velocity profiles.(V_{edge} - edge vel.)

5.2.2 Hodograph Velocity Profiles in Measurement Plane

Early researchers (Johnston,1960) suggested a simple model for three dimensional boundary layer velocity profiles, known as hodograph or triangular plot for the distribution of cross flow or radial velocity. The results for the current investigation are shown in Figures 5.21a and 5.21b, for the suction and pressure surface, respectfully.

On the suction surface, the agreement between the computation and the measurement is fairly accurate, especially at the H=0.7 location, where the appreciable boundary layer thickness allowed for finer resolution of the velocity profile. In the secondary flow region (H=0.825) the deviation is very large, and the boundary layer code severely underpredicts the cross flow velocity distribution. From the hodograph plots, it is clearly evident that the measurements obtained in this investigation and the boundary layer code prediction agree only in regions away from the endwalls and the secondary flow region. The complex flow including the presence of a casing-suction corner passage vortex, blade and endwall boundary layer interaction and the difficulty in accurately specifying the edge boundary conditions requires the use of Navier-Stokes code.

The computed profiles (Figure 5.21a) indicate a fairly small limiting streamline angle close to the suction blade surface in the mid span region. The measured crossflow component in the secondary flow region increases dramatically (see Figure 5.5 and 5.6) at the H=0.825 location. On the pressure surface (Figure 5.21b) the agreement is very good in the mid span region (H=0.3 to 0.7) with increasing deviation in the endwall region

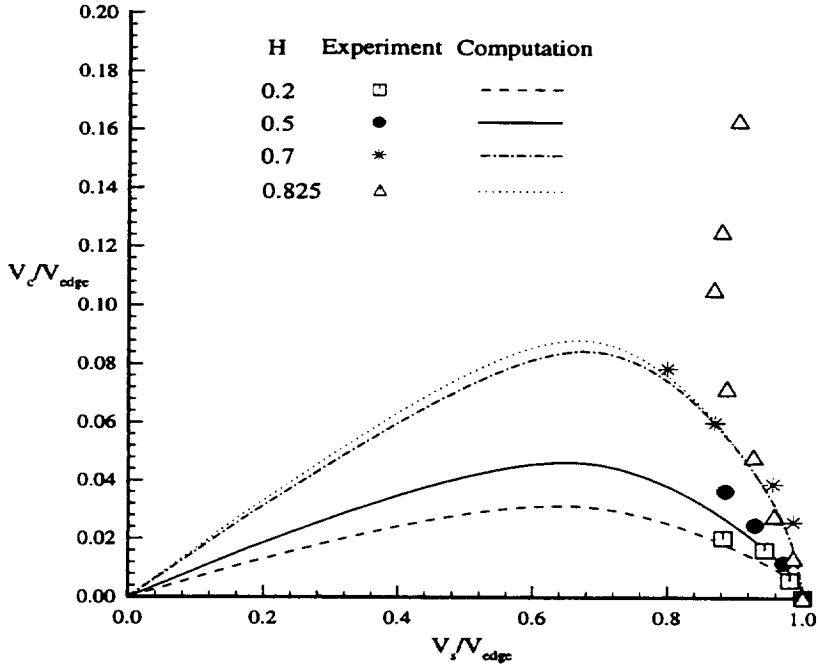

a)

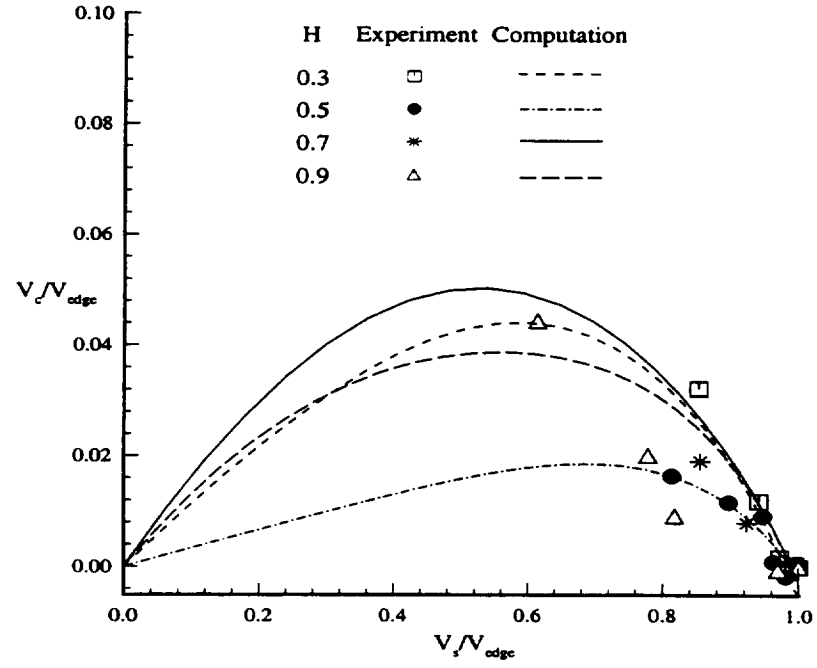

b)

Figure 5. 21 Velocity Profile Hodograph Plot. a) Suction Surface (x/cm=0.85), b) Pressure Surface (x/cm=0.945).

(H=0.9). At the H=0.9 location the boundary layer code over predicts the crossflow velocity component (V_c/V_{edge}) (see section 4.3.1).

5.2.3 Integral Properties

The integral properties were calculated by fitting a fifth order polynomial through the measured data points. From the flow visualization experiment, the boundary layers were determined to be laminar on the pressure surface of the blade and partially or fully turbulent on the suction, hub, and casing surfaces. The computed and measured integral properties of the boundary layers, defined in section 4.3, are presented in Figures 5.22, 5.23, 5.24 and 5.25. The Shape factor H_{SS} is defined as the ratio of the displacement and momentum thicknesses ($H_{SS}=\delta_s^*/\theta_s$).

On the suction surface (Figure 5.22), the displacement and momentum thickness are almost constant away from the endwalls (slight decrease in the hub-to-tip direction due to the radialy inward pressure gradient). Close to the hub-suction surface corner, the values of δ_s^* and θ_s increase rapidly due to the influence of the hub wall boundary layer. Very good agreement between the measured and computed properties is observed in the regions away from the endwalls and secondary flow (H=0.2 to H=0.7). In the casing-suction corner, the passage vortex and casing boundary layer increases the momentum and displacement thicknesses substantially. The boundary layer prediction is obviously

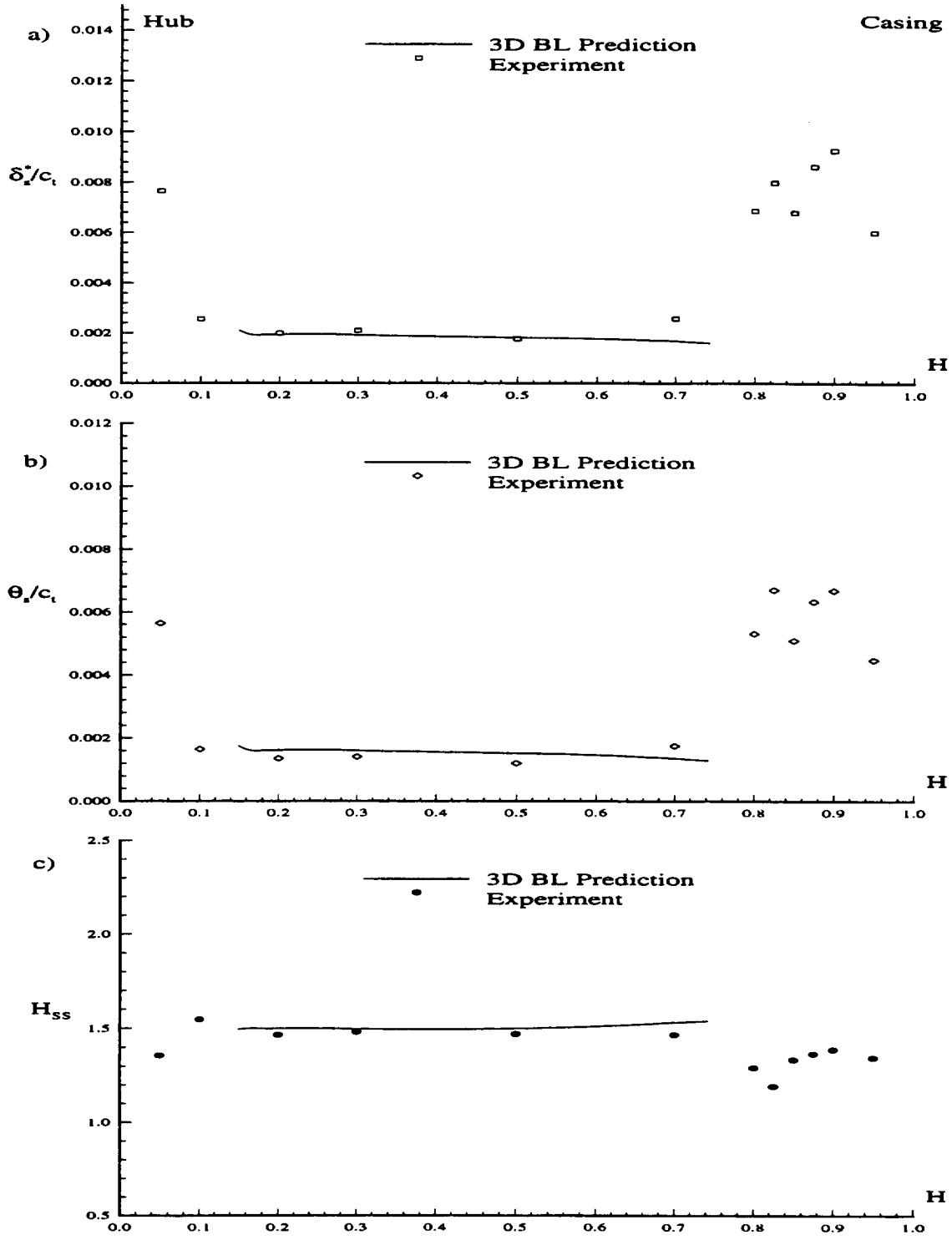

Figure 5. 22 Measured and Computed Integral Properties of Boundary layers. Suction Surface, x/c_m=0.85. a) Displacement Thickness, b) Momentum Thickness, c) Shape Factor.

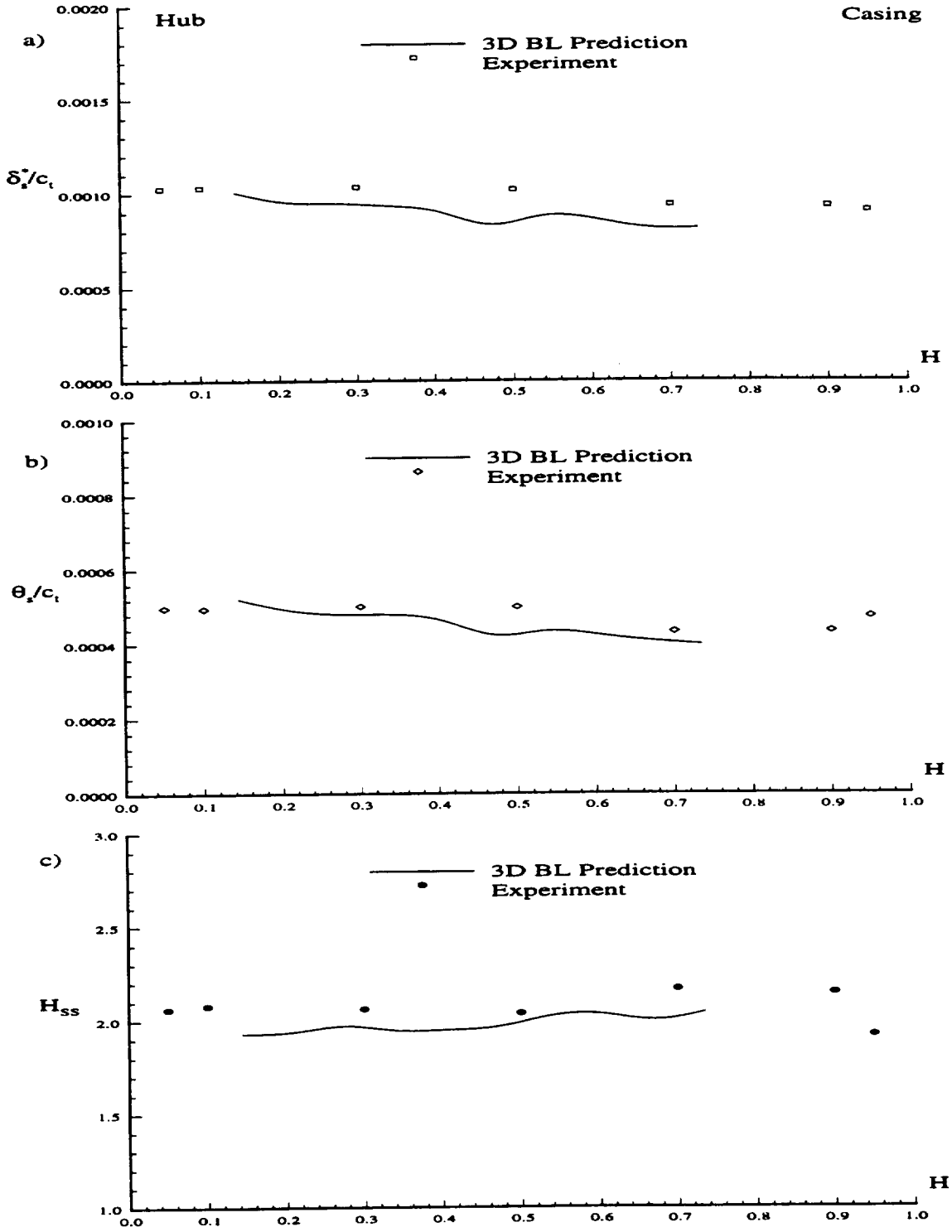

Figure 5. 23 Measured and Computed Boundary Layer Integral Properties. Pressure Surface, x/c_m=0.945. a) Displacement Thickness, b) Momentum Thickness, c) Shape Factor.

inaccurate in this region. The measured shape factor H_{SS} remained constant (around 1.5) indicating a turbulent boundary layer. A decrease in the shape factor in regions close to the endwalls is probably due to the difficulty in computing the boundary layer thickness accurately in the secondary flow region.

On the pressure surface, Figure 5.23, the computed integral boundary layer properties are in good agreement with measured data in most of the regions, away from the endwalls, where secondary flow effects are small. The reason for the discrepancy at a few locations is the assumption of a flat plate extending down stream of the trailing edge of the nozzle vane, required by the boundary layer code input grid design. The flat plate has a specified zero pressure gradient which may affect the boundary layer growth. The three dimensional boundary layer solution at x/c_m=0.945 is fairly accurate in predicting the integral properties, with a maximum deviation of 14% from the measured values, in regions away from the endwall surfaces. The momentum thickness decreases in the radial direction to a much lesser extent than that on the suction surface of the blade. The shape factor H_{SS} remaines constant over the pressure surface indicating that the boundary layer is laminar.

Comparison of the predicted and measured integral properties on the hub endwall surface, shown in Figure 5.24, indicate fairly good agreement away from the suction surface of the blade (from S=0.4 toward the pressure surface). The displacement and momentum thicknesses decrease from the suction to the pressure surface due to the presence of strong transverse pressure gradient. Since measurements

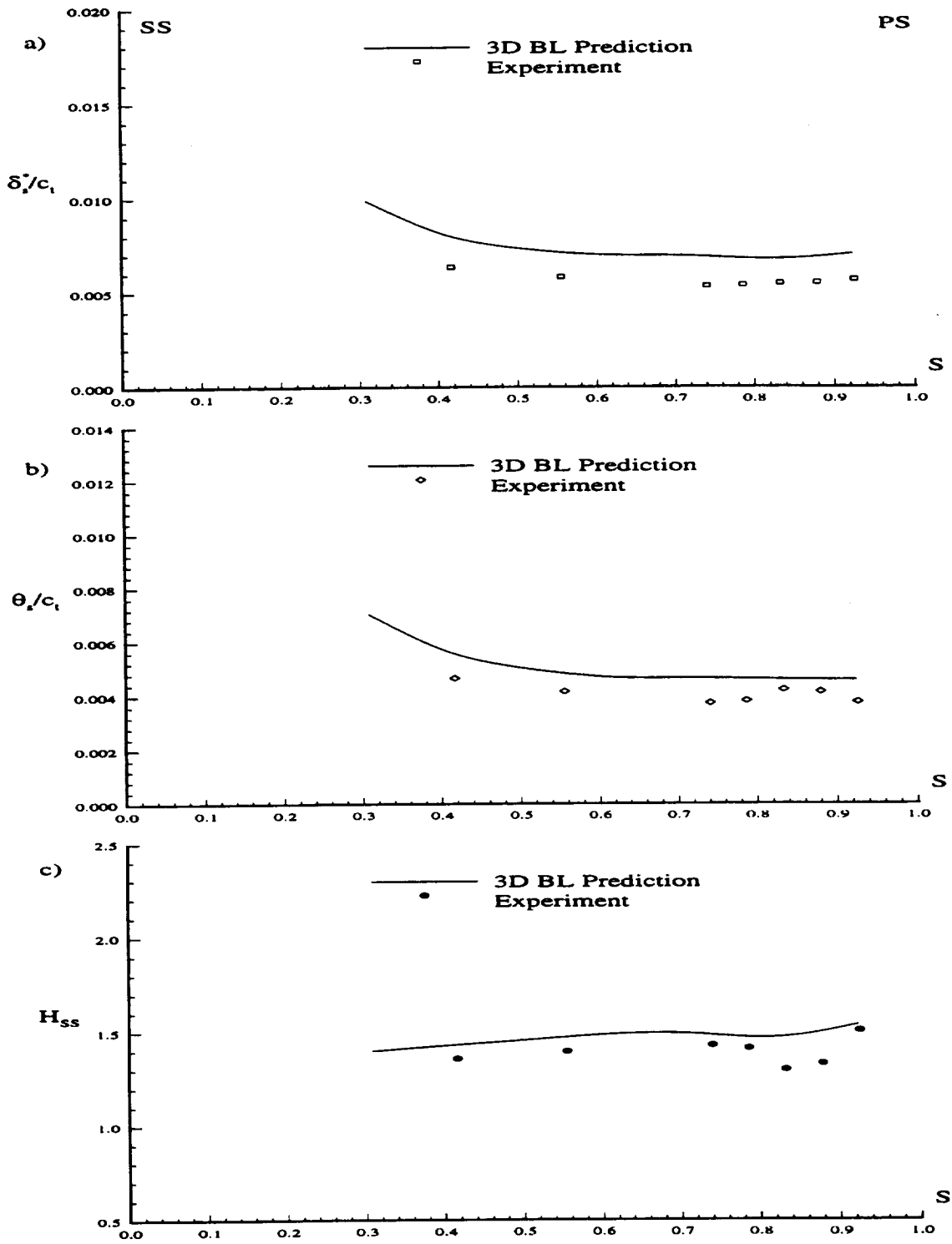

Figure 5. 24 Measured and Computed Boundary Layer Integral Properties. Hub Surface, x/c_m=0.94. a) Displacement Thickness, b) Momentum Thickness, c) Shape Factor.

could not be accomplished in the suction-hub surface corner, due to access problems, the applicability of the 3D boundary layer code could not be confirmed at this location. In the mid pitch and close to the pressure surface regions, the prediction and measurement agree fairly well. The momentum and displacement thicknesses are much higher compared to those on the blade (Figures 5.22 and 5.23) due to the existence of a upstream wall boundary (casing and hub endwalls extend more than ten axial chords upstream of the blade leading edge) .

The measured properties on the casing endwall, shown in Figure 5.25, demonstrate the inability of the boundary layer code to accurately predict the viscous layer properties in regions of a secondary vortex, present in the suction-casing surface corner. The computation could not be carried out in this region. From mid-pitch to the pressure surface, the computation agrees well with the measured properties, accurately predicting a decrease in the boundary layer momentum and displacement thicknesses in the blade-to-blade direction (from suction to pressure). Very high values of δ_s^* and θ_s are present in the corner formed by the suction and casing surfaces due to the presence of secondary flow vortex and entrainment of fluid by the vortex in this region (extending from H=0 to 0.4).

In the secondary flow region, the classical definition of the boundary layer integral properties are no longer applicable due to the difficulty in delineating the boundary between the viscous layer and the external flow. In these cases, a three dimensional Navier-Stokes prediction is essential in accurately predicting both the local and integral properties. Outside the secondary flow region, the boundary layer approach is valid,

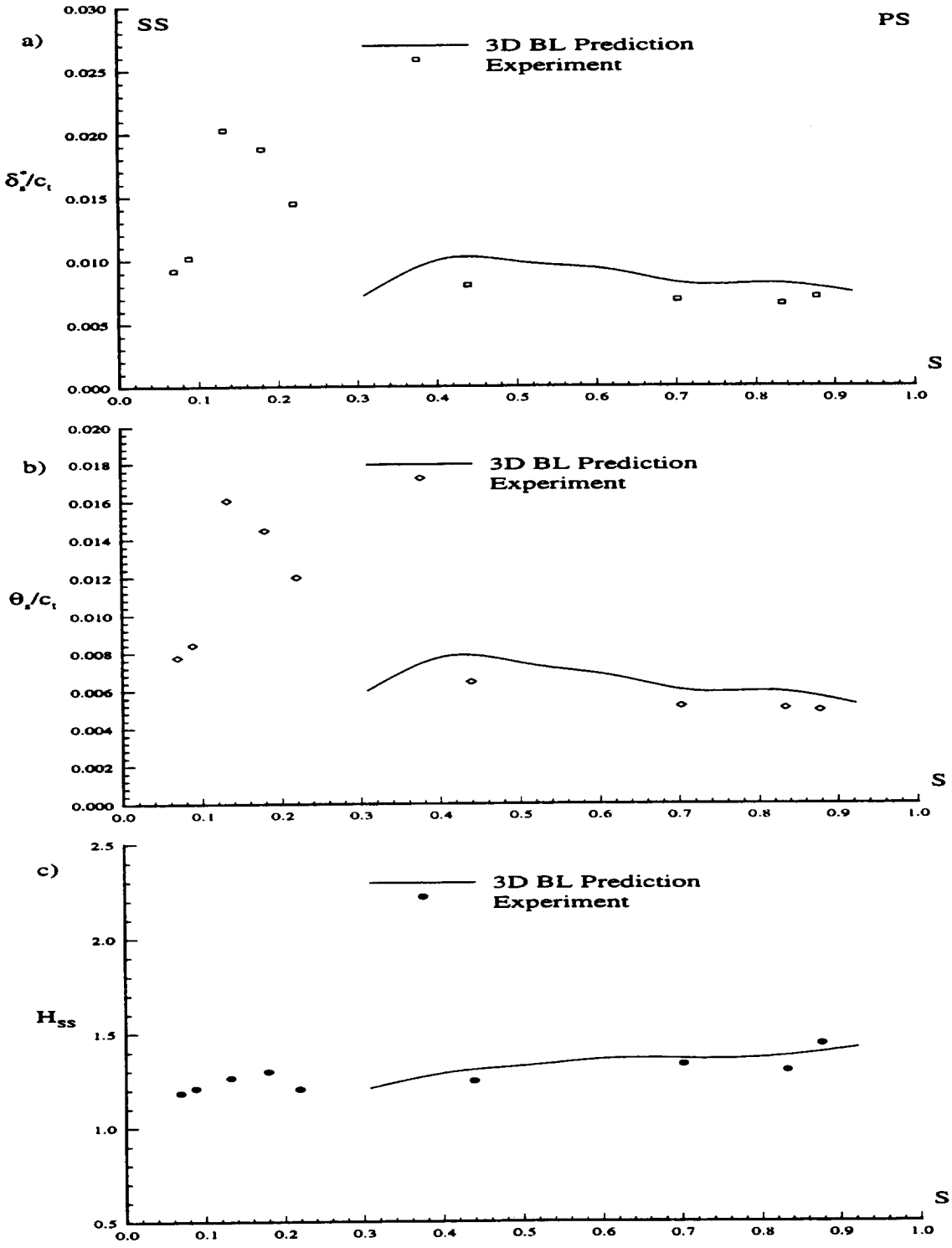

Figure 5. 25 Measured and Computed Boundary Layer Integral Properties. Casing Surface, x/c_m=0.85. a) Displacement Thickness, b) Momentum Thickness, c) Shape Factor.

requiring only an accurate pressure distribution, and much simpler to implement.

5.3 Influence of Downstream Rotor

The presence of a rotor very close to the nozzle blade passage influences the boundary layer development and behavior of the endwall and vane surface boundary layers inducing earlier transition and increasing unsteadiness in the free stream, through the introduction of an unsteady pressure field. In the AFTRF, the auxiliary fans used for generating the through flow also have an influence on the unsteadiness in the nozzle vane passage. The following section will investigate the potential interaction of the downstream turbine rotor and auxiliary fans on nozzle vane boundary layer measurements at H=0.50 radial location on the pressure surface.

5.3.1 Turbulence Spectra

The turbulence spectra, one inside the boundary layer (S=0.983) and one in the free stream (S=0.85) of the nozzle vane passage are shown in Figures 5.26 and 5.27 respectfully. The measurements were taken at the mid span location (H=0.5). The spectrum was derived by implementing an FFT transformation of the instantaneous total velocity data. The two peaks occurring at 473 and 653 Hz coincide with the blade passing frequencies of the auxiliary fans and rotor. Acoustic field measurements (Appendix A) indicate that the dominant source of noise in the facility are the auxiliary fans operating at a constant of 1807 RPM.

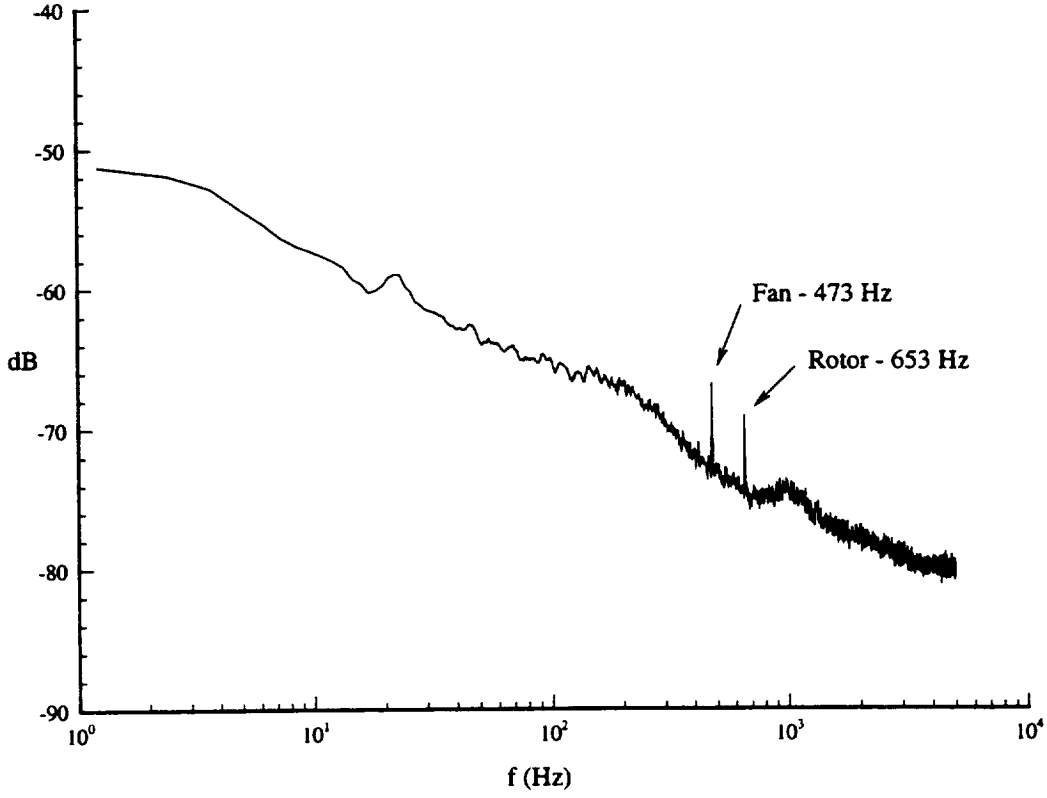

Figure 5. 26 Turbulence spectra (256 averages, square window FFT). Pressure Surface, free stream at x/c=0.945, midspan, S=0.85. Where $dB = 20 \log \sqrt{\overline{v'^2}} / V$.

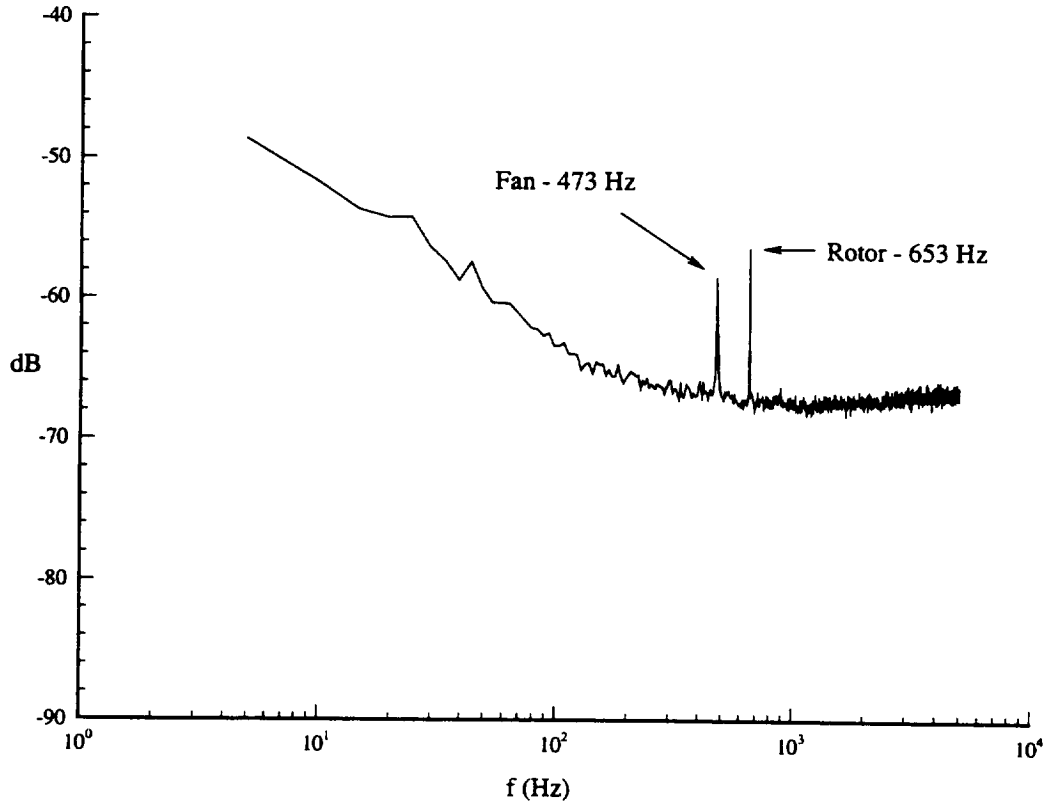

Figure 5. 27 Turbulence spectra close to the surface of the blade (inside the boundary layer). Pressure surface at x/c_m=0.945, mid span, S=0.983.

The periodic component associated with the auxiliary fans is still strong enough to influence the measurements in the nozzle vane passage. Measurements indicate that only the fundamental frequencies are present in any measurable degree. The higher order harmonics of the rotor blade are indistinguishable from the turbulence spectrum in Figures 5.27 and 5.28. The spectrum in the boundary layer indicated broadening of the peaks suggesting a larger influence on the unsteadiness in the viscous layer than in the external flow.

Using a very narrow (7 Hz) square window, the two peaks were filtered out of the original instantaneous signal. A comparison of the filtered and unfiltered spectra in the frequency range of the measurement is shown in Figure 5.28. Performing an inverse FFT transformation, the filtered data set was processed using the same procedure applied to the unfiltered data. The procedure was repeated for each measurement location to optimize the filtering and account for the variations in the rotor RPM during measurements. One drawback of this procedure is the long processing time and storage space required to perform the above transformation.

A comparison of the total turbulence intensity from the filtered and unfiltered data for one boundary layer profile is shown in Figure 5.29. The total turbulence intensity is defined as:

$$Tu = \frac{\sqrt{\overline{v_s'^2} + \overline{v_c'^2}}}{V} \tag{5.3}$$

In the free stream a substantial decrease in the total turbulence intensity (Tu) was observed (from a level of 2.1% to 0.9%) indicating a mild influence of the rotor. The

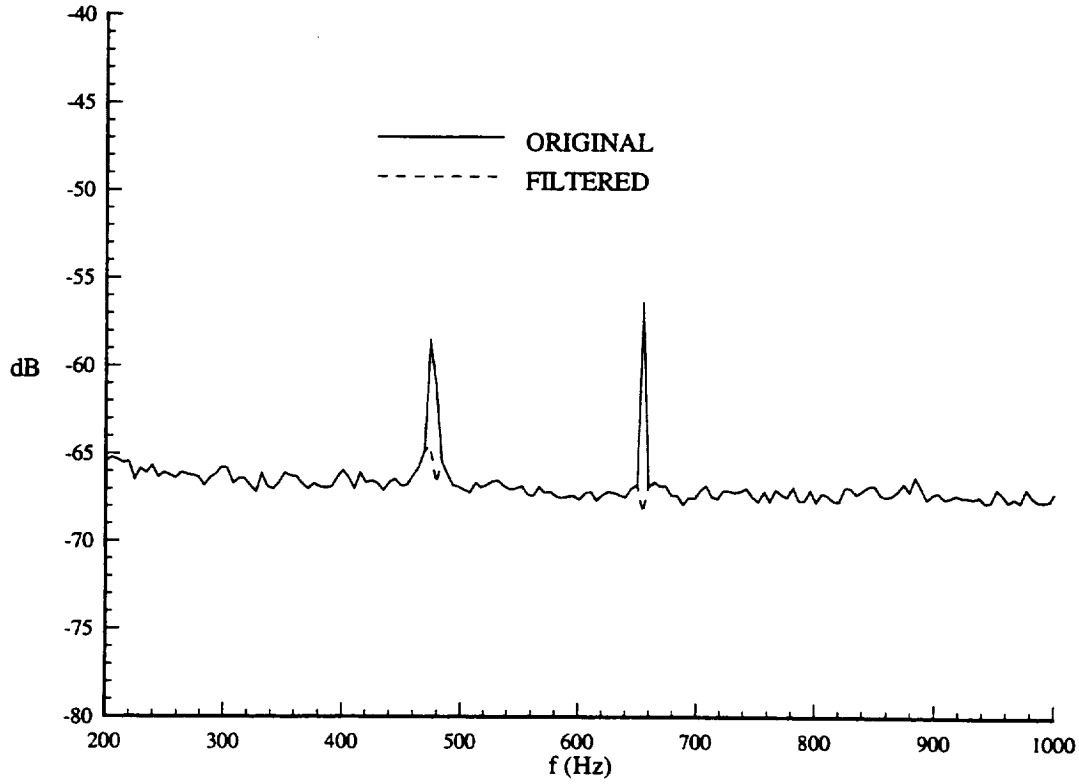

Figure 5. 28 Comparison of filtered and unfiltered signal. Notch filters at 473 and 654 Hz. Pressure Surface, free stream at x/c=0.945, H=0.50 S=0.85. Where $dB = 20 \log \sqrt{\overline{v'^2}} / V$.

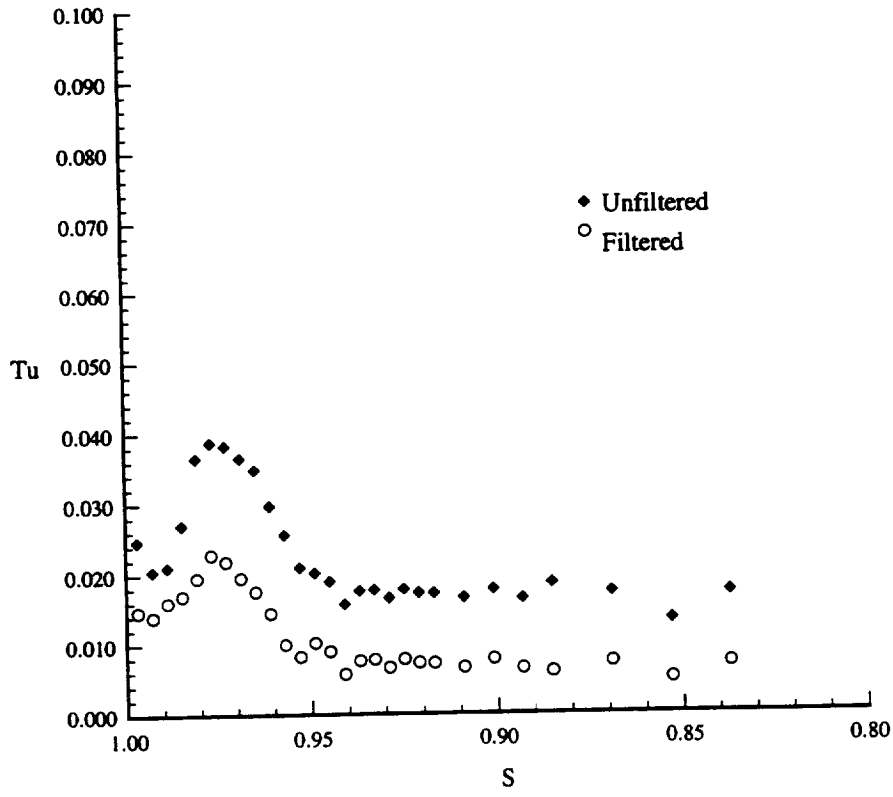

Figure 5. 29 Total turbulence intensity based on filtered and unfiltered signal. Pressure surface, x/c_m=0.945, H=0.5.

pressure surface boundary layers are therefore laminar in nature and the measured turbulence intensity is a result of the potential effect of the downstream rotor fan and the auxiliary fans. In the boundary layer region the effect is even larger, decreasing the maximum measured value from 4.1% to 2.4% at the midspan measurement location. This would indicate that the predominant source of the measured unsteadiness is due to the rotor periodic unsteadiness and that the actual unresolved random turbulence levels are much lower. In the viscous layer the influence of the periodic downstream conditions is even more pronounced. The conclusion that the pressure surface boundary layers are still laminar at the measurement location is valid due to the strong potential effect of the rotor.

5.3.2 Velocity Correlation

Using the previously described procedure for filtering out the periodic influence of the auxiliary fans and turbine rotor, the correlation of the instantaneous velocity fluctuations (u' and v') could be investigated. Determination of the correlated velocity fluctuation is accomplished by:

$$\overline{u'(t)v'(t+\Delta t)} = \frac{1}{T}\int_0^T u'(\tau)v'(\tau+\Delta t)\,d\tau \qquad (5.4)$$

for each value of Δt, where T is the total sample time . The maximum value of term $\overline{u'(t)v'(t+\Delta t)}$ is evaluated over a range of Δt. In Figure 5.30 the influence of the periodic velocity fluctuations are clearly visible. As can be expected, the steady periodic influence

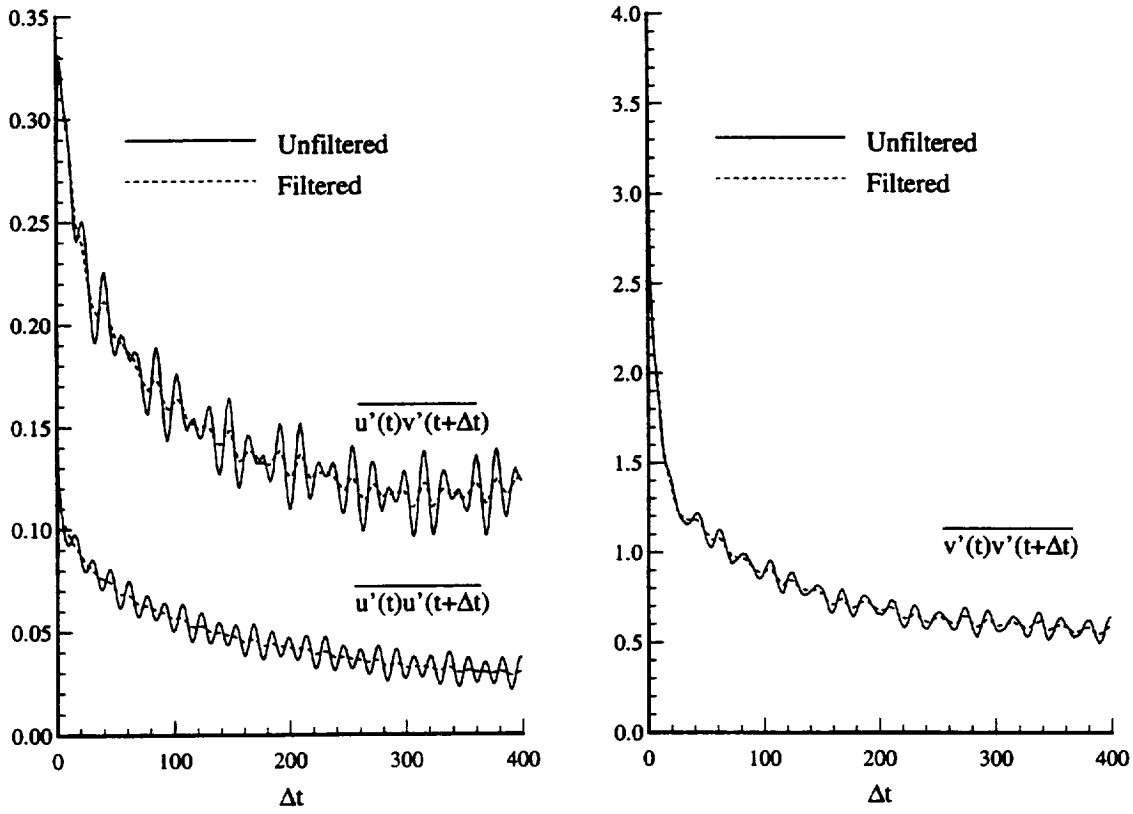

Figure 5. 30 Velocity Correlation with filtered and unfiltered signal.

was removed more efficiently in the two $\overline{u'(t)u'(t+\Delta t)}$ and $\overline{v'(t)v'(t+\Delta t)}$ terms, while in the cross correlation terms the higher order harmonics of the blade passing frequency remained. Acquisition of the data using an encoder-locked data sampling frequency, while removing the influence of the rotor, could not account for the auxiliary fan and higher order periods. The digital filtering approach used here yielded acceptable results in experiments by Cramp and Shin (1994) performed in a multistage compressor.

The time required for the correlation function to reach a constant value is called the Lagrangian integral scale τ (Tennekes and Lumley, 1972), and the resulting Lagrangian integral length scale l_L (defined as l_L=u' τ) can be calculated. In the measurements accomplished here the length scale was calculated to be in the 4.5 to 5.0 mm range for the filtered signal correlation's in the u (stream wise) direction which correspond to measurements by Cramp and Shin (1994) of approximately 3% of the stator chord length in an axial multistage compressor.

5.4 Turbulence Properties

The two sensor probe measurements allowed simultaneous acquisition of the instantaneous velocity fluctuations in two directions. Measurements of the time averaged properties were corrected for the finite displacement between the two sensors but the unsteady properties could not be corrected. A discussion of the error in the turbulence quantities is covered in Appendix B. The instantaneous velocities were resolved into streamwise and crosswise components and averaged over the number of samples acquired. In the previous section (5.3) the effect of the downstream turbine rotor and the auxiliary fans was found to be appreciable and this will account for a portion of the measured turbulence intensity. The effect of downstream rotor and fan on the measured Reynolds stress terms was found to be negligible.

5.4.1 Turbulence Measurements on Suction Surface at x/c_m=0.85

The measured total turbulence intensity profiles, (Tu) defined as:

$$Tu = \frac{\sqrt{\overline{v_s'^2} + \overline{v_c'^2}}}{V} \tag{5.5}$$

at 12 radial stations along the suction surface of the nozzle blade at x/c_m=0.85, is shown in Figure 5.31. In the free stream, the average level of turbulence was found to be 2.2% in the region from H=0.1 to 0.7. Since the boundary layers are thin away from the casing wall, the location and magnitude of peak turbulence intensities in the near wall region

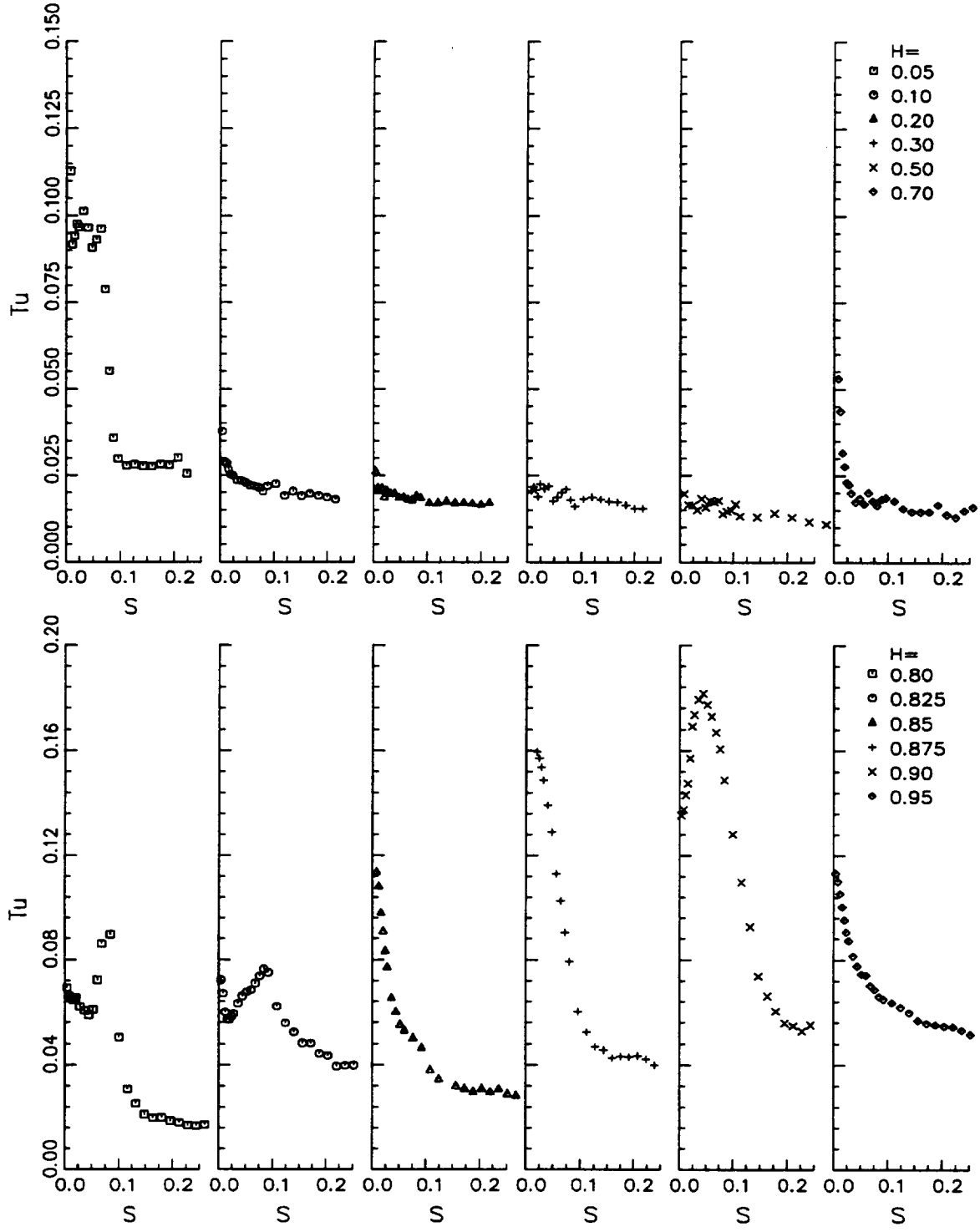

Figure 5. 31 Measured Total Turbulence Intensity (Tu) on Suction Surface at x/cm=0.85. H=0.0 hub, H=1.0 casing surface.

could not be captured. Nevertheless, the data shows increased intensities as the wall is approached. The free stream intensities increased near the casing- suction surface corner to approximately 6% at H=0.95, indicating that this measurement location is all ready within the casing boundary layer region. The measurement in the secondary flow region at H=0.8, 0.825, and 0.85 locations indicate the existence of a secondary peak in the passage vortex region. The turbulence intensity at H=0.8 increases toward the center of the passage vortex reaching a maximum of 8.2% (occurring at the location closest to the vortex core), then decreases toward the blade surface. The maximum measured turbulence intensity occurred at the H=0.90 radial location reaching 18% which is caused by interaction of the blade surface and casing surface (corner flow) boundary layers.

The streamwise and crosswise components of turbulence are defined as:

$$Tu_s = \frac{\sqrt{\overline{v_s'^2}}}{V_s} \qquad Tu_c = \frac{\sqrt{\overline{v_c'^2}}}{V_c} \tag{5.6}$$

The components of the turbulence intensities in the stream wise (Tu_s) and cross wise (Tu_c) direction, plotted in Figure 5.32, shows similar levels of unsteadiness away from the endwall region. This differs from conventional boundary layers, where the cross flow component is smaller than the streamwise component. The fact that the levels are similar indicate the influence of radial inward flow and secondary flow in amplifying the turbulence in the crossflow direction. The components of unsteadiness differed only in the two extreme radial locations (H=0.05 and 0.95) due to the merging of the wall and blade boundary layers and interaction with the secondary flow. In the tip region a decrease in

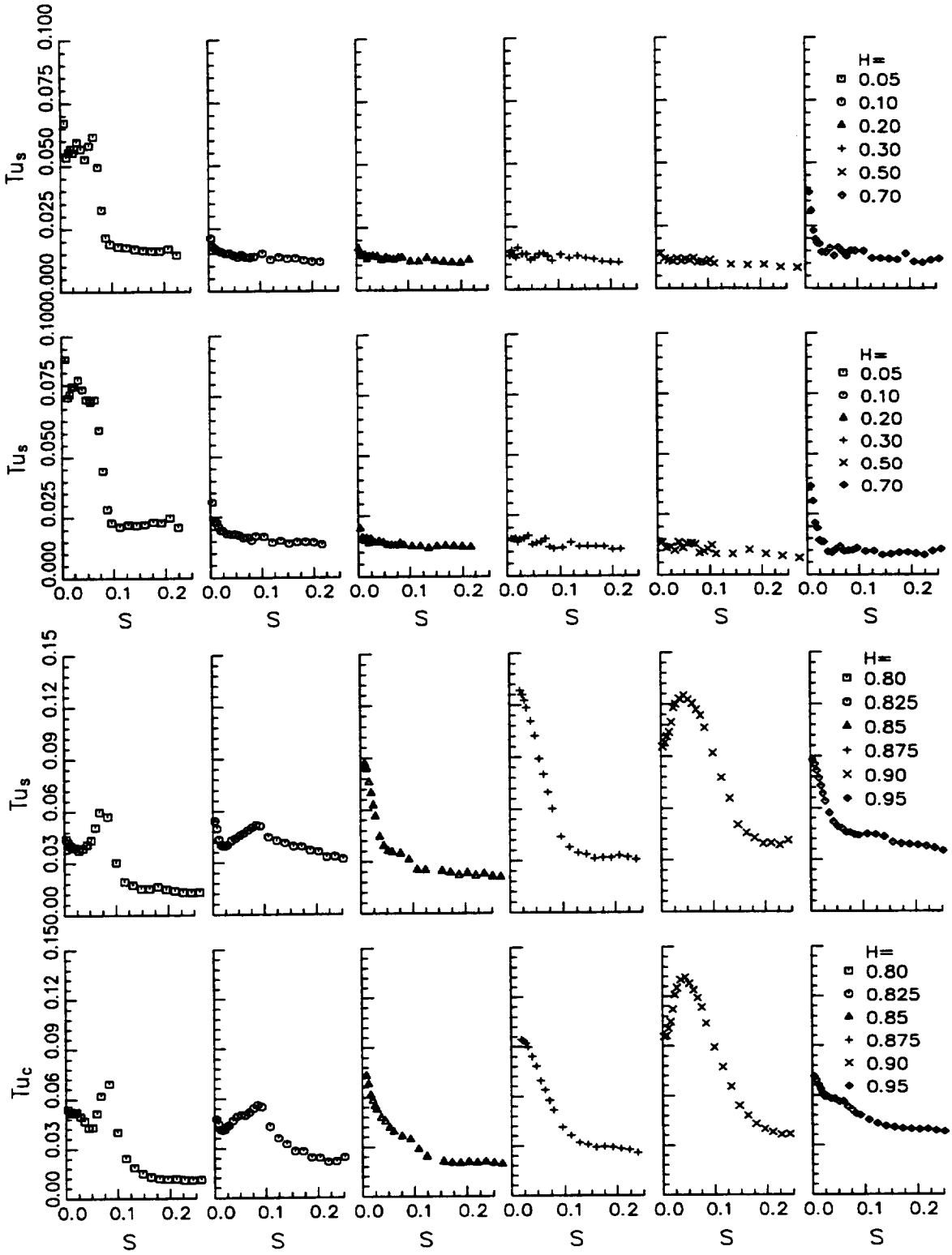

Figure 5. 32 Turbulence Intensity in the stream wise (Tu_S) and crosswise directions (Tu_C). Suction Surface at x/c_m=0.85.

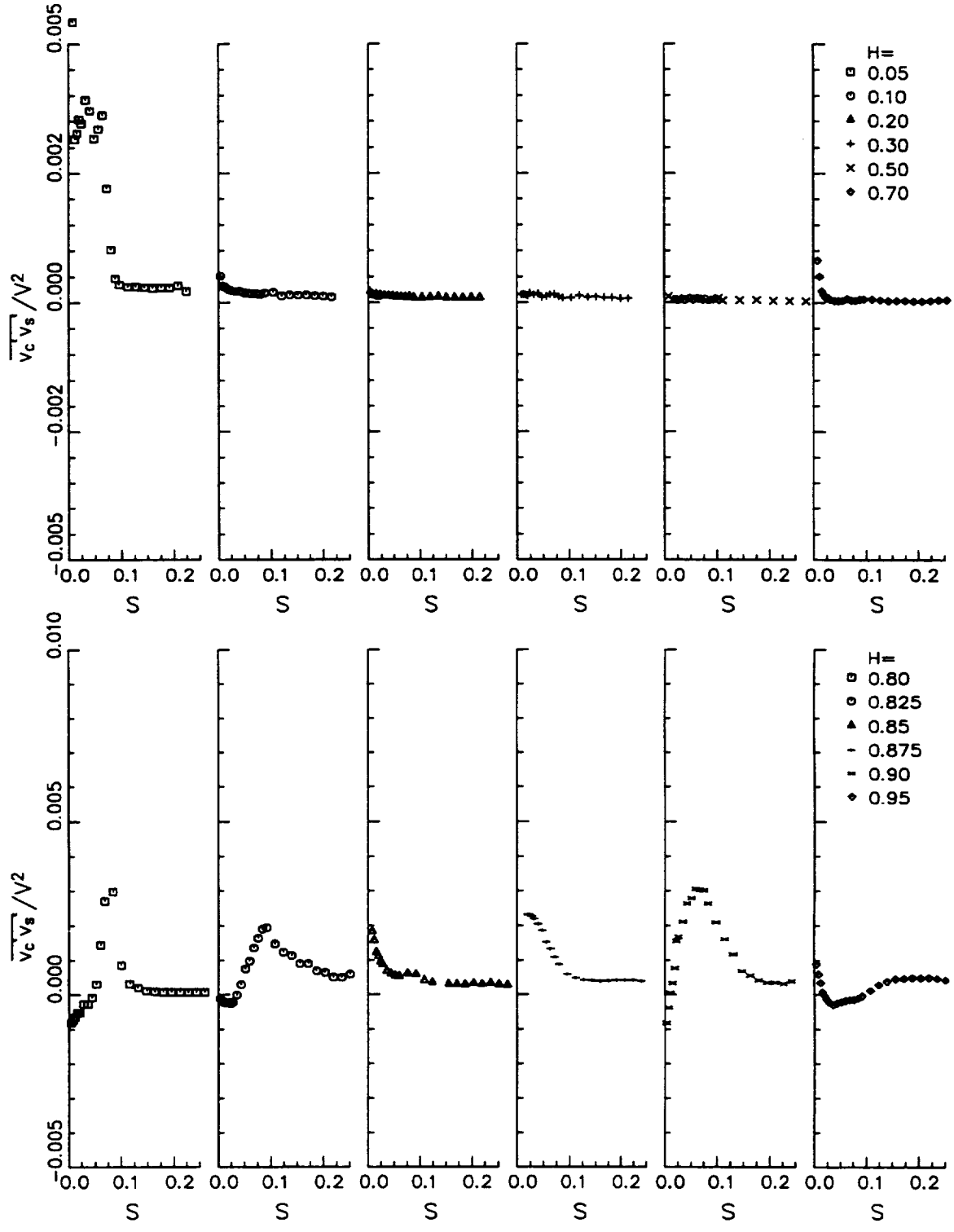

Figure 5. 33 Measured Velocity Correlation on Suction Surface (x/c_m=0.85) .

turbulence properties from location H=0.9 to 0.95 is observed due to reduced influence of secondary flow and vortex as the wall is approached. In the passage vortex region, the relative levels of streamwise and crosswise components of turbulence remained similar. In the tip region the turbulence intensity in the streamwise direction increased due to the influence of the casing endwall boundary layer and the secondary flow region. Locations close to the hub (H=0.05 and 0.10) indicate an increase in the cross wise component of turbulence due to influence of the endwall boundary layer. The overall levels of the turbulence intensity components in the free stream and secondary flow regions (excluding the endwall locations, i.e. H=0.05 and 0.95) indicates isotropic turbulence.

The measured Reynolds stress component $\overline{v_s' v_c'}$ based on the instantaneous velocity measurements, shown in Figure 5.33, varied appreciably in the secondary flow region. As expected the levels of unsteadiness were very low away from the endwall region, increasing only slightly in the viscous region. The presence of the passage vortex is indicated by the peak values of $\overline{v_s' v_c'}$ near the vortex at H=0.8 and 0.825 (Figure 5.33). One side of the passage vortex increases the correlation term due to the shearing stress of the fluid elements moving against the mean flow, reaching a maximum at the core center, and then decreases on the opposite side. In the hub endwall region the increase in the stress term $\overline{v_s' v_c'}$ is due to the interaction of the endwall boundary layer.

5.4.2 Casing Surface

The distribution of turbulence properties on the casing endwall surface are shown in Figures 5.34, 5.35, and 5.36. In the casing-suction surface corner, the characteristic double peak in the turbulence intensity is due to the presence of the passage vortex described earlier. The increase in turbulence intensity close to the wall is due to the interaction of the passage vortex and the casing endwall boundary layer and the peak away from the surface is due to the secondary flow vortex. The total turbulence intensity (Figure 5.34) increased from the free stream value of 0.022 to 0.06 in the vortex core located near S=0.132. The turbulence intensity then decreases through the casing surface side of the vortex interacting with the casing boundary layer. The Turbulence intensity increases toward the wall reaching a maximum of 0.09 decreasing toward the wall. Away from the secondary flow region the boundary layer thickness decreases with a corresponding reduction in the overall level of unsteadiness in the viscous layer.

The individual components of turbulence Tu_s and Tu_c, shown in Figure 5.35, exhibit behavior similar to the suction blade surface data in the corner region. The over all levels of turbulence intensity in the cross flow direction is larger than the level in the streamwise direction due to the high flow turning along the casing endwall. Outside of the viscous and secondary flow regions the unsteadiness in the mean flow is very low and is similar to measurements obtained at the x/c_m=0.56 location (Figure 3.6b).

Figure 5.36 presents the measured velocity correlation term inside the casing endwall flow at 9 tangential stations. In the secondary flow region of the casing - suction

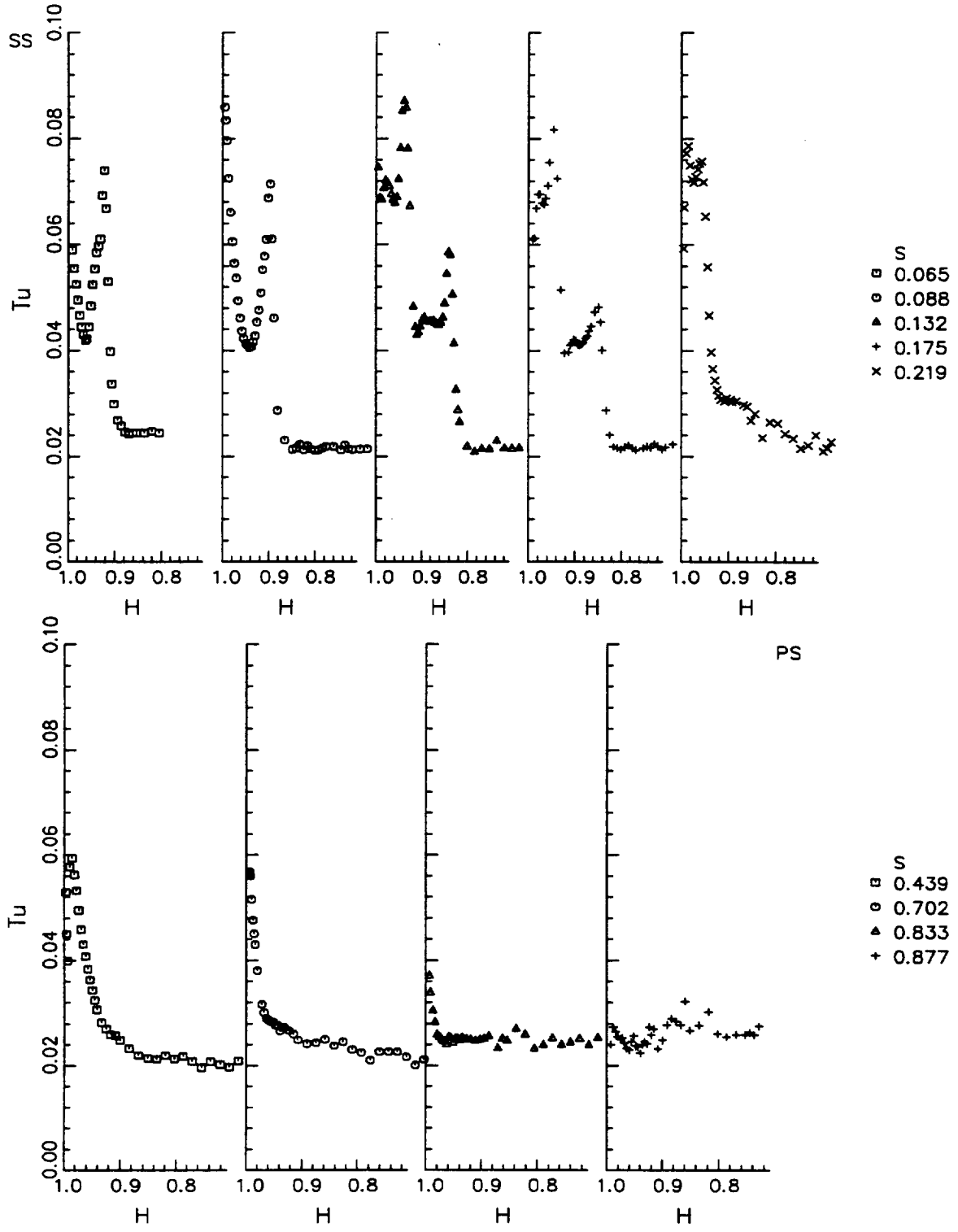

Figure 5. 34 Measured Total Turbulence Intensity on Casing Surface at x/c_m=0.85. SS - Suction Surface, PS -Pressure Surface.

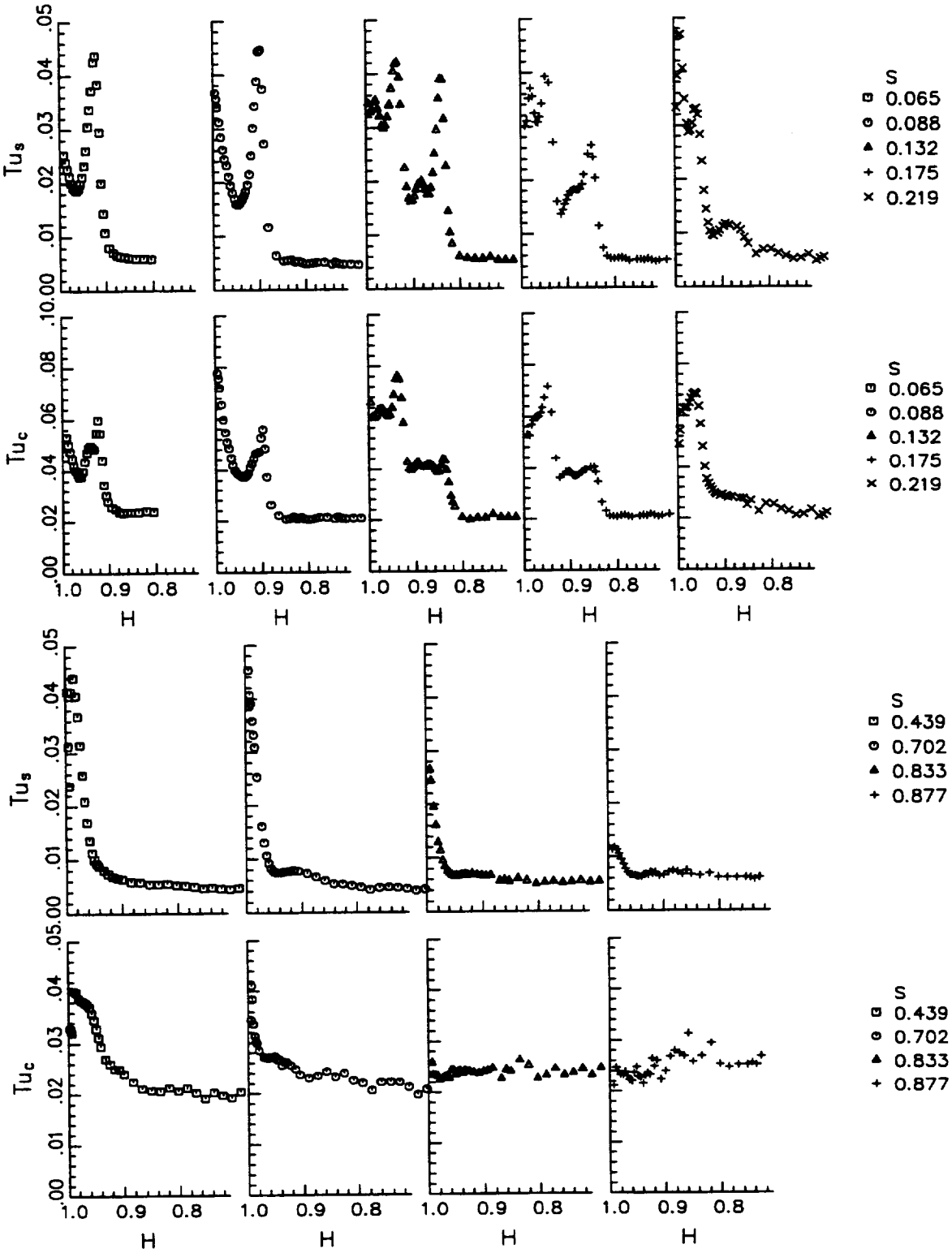

Figure 5. 35 Measured stream wise and cross wise turbulence intensity on casing surface at x/c_m=0.85.

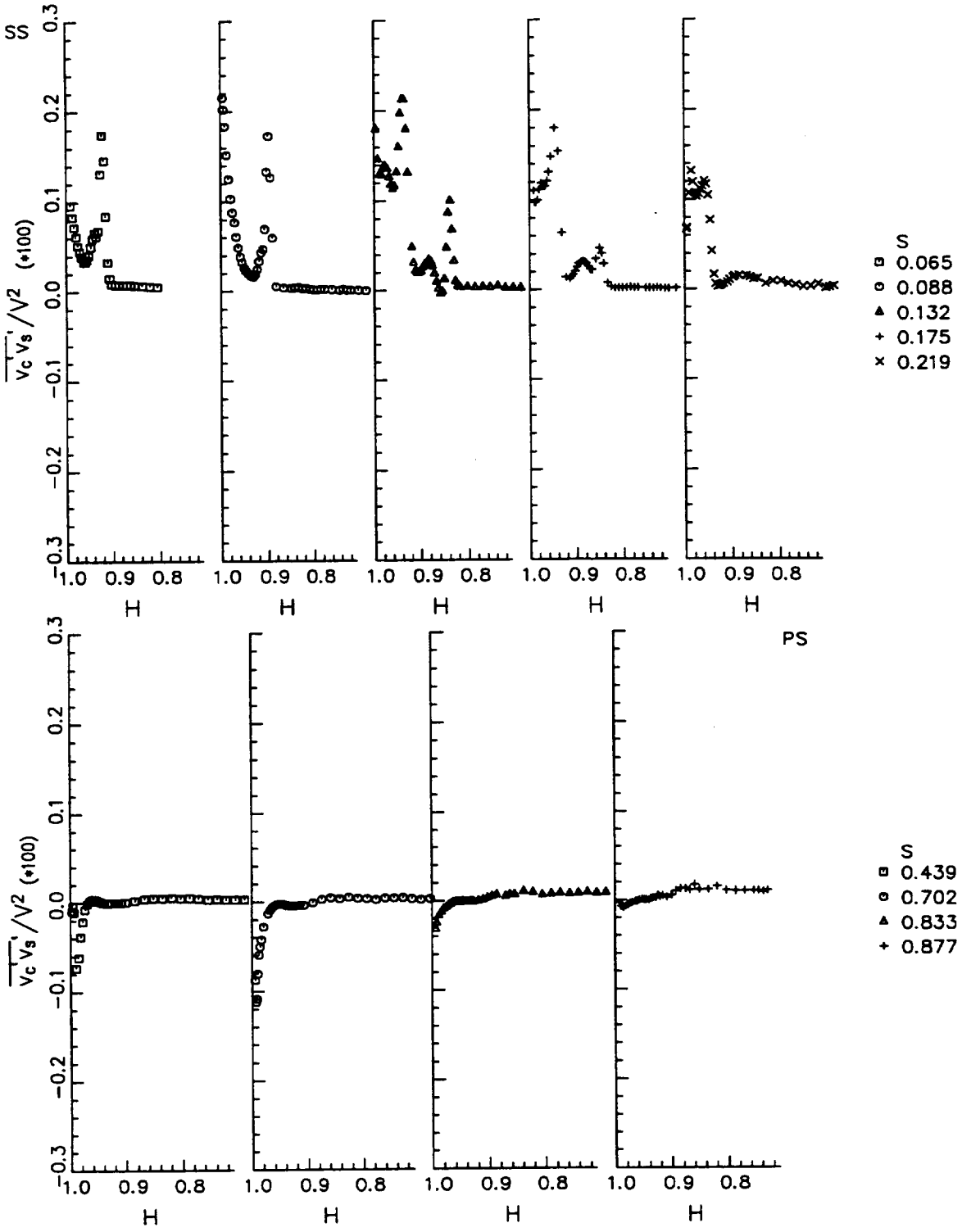

Figure 5. 36 Measured Velocity Correlation term at x/c_m=0.85 on the Casing surface. SS - Suction Surface, PS - Pressure Surface.

surface corner the measured Reynolds stress is very high, due to the presence of the passage vortex. In the mid pitch and pressure surface regions (S=0.439, .702, .833, and .877) the level decreases. toward the pressure side of the casing surface. The measured Reynolds stress term decreased to a minimum at the pressure side following a decrease in the boundary layer thickness due to the strong blade to blade pressure gradient (tangential direction).

5.4.3 Hub Endwall Measurements

On the hub endwall surface measurements of total turbulence intensity at seven tangential locations are shown in Figure 5.37. Due to access problems indicated earlier, measurements could not be obtained at locations closer to the suction surface. The boundary layers are thin in regions away from the suction side (compared to the casing endwall) and the turbulence intensity increases from a free stream value of 2.1% to approximately 5% at the closest measurements to the surface. The level of unsteadiness decreased toward the pressure surface. At the S=0.924 (very close to the pressure surface) location a slight increase in turbulence intensity in the free stream is an indication of the influence of blade pressure surface boundary layer. The turbulence intensity indicates thin, well behaved boundary layers, with portions of the measured intensity coming from the influence of the downstream rotor and auxiliary fan (see Section 5.3).

The measured individual components of turbulence (Figure 5.38) indicated that the hub endwall boundary layer, at least in regions far away from the secondary flow region,

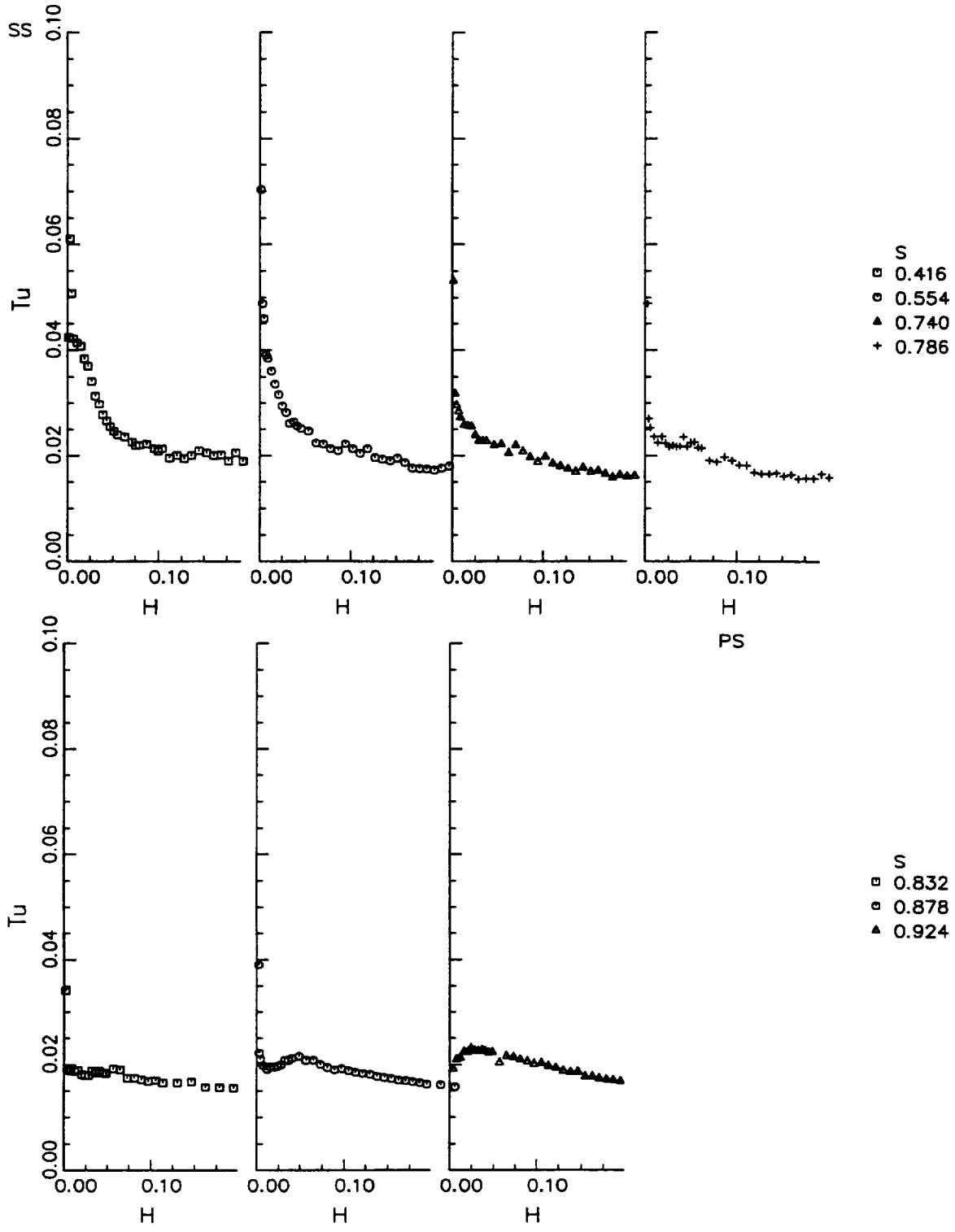

Figure 5. 37 Total Turbulence Measured on Hub Endwall at x/c_m=0.95. SS - Suction surface, PS - Pressure surface.

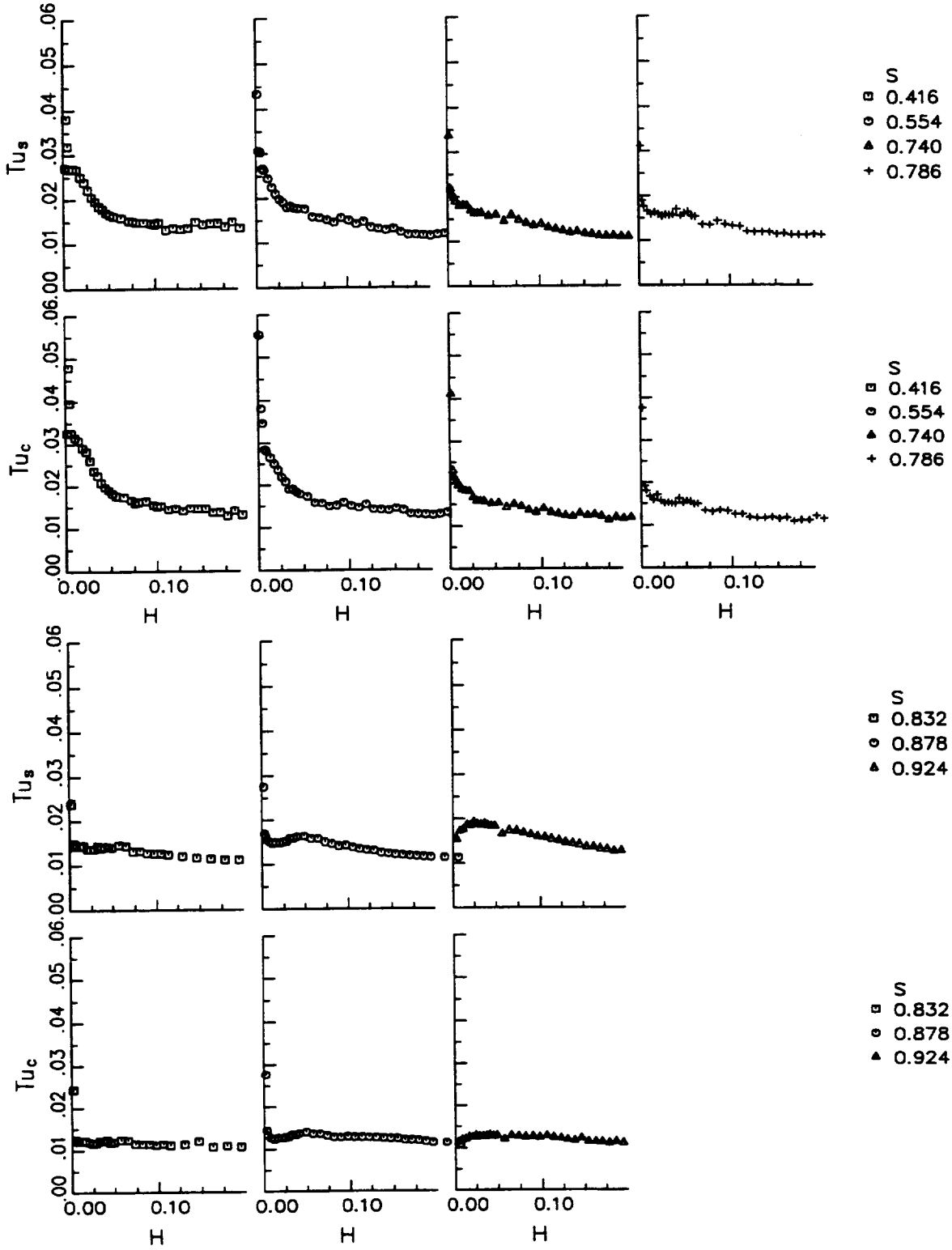

Figure 5. 38 Measured turbulence intensity in the stream wise and cross wise direction. Hub Endwall surface,x/c_m=0.95.

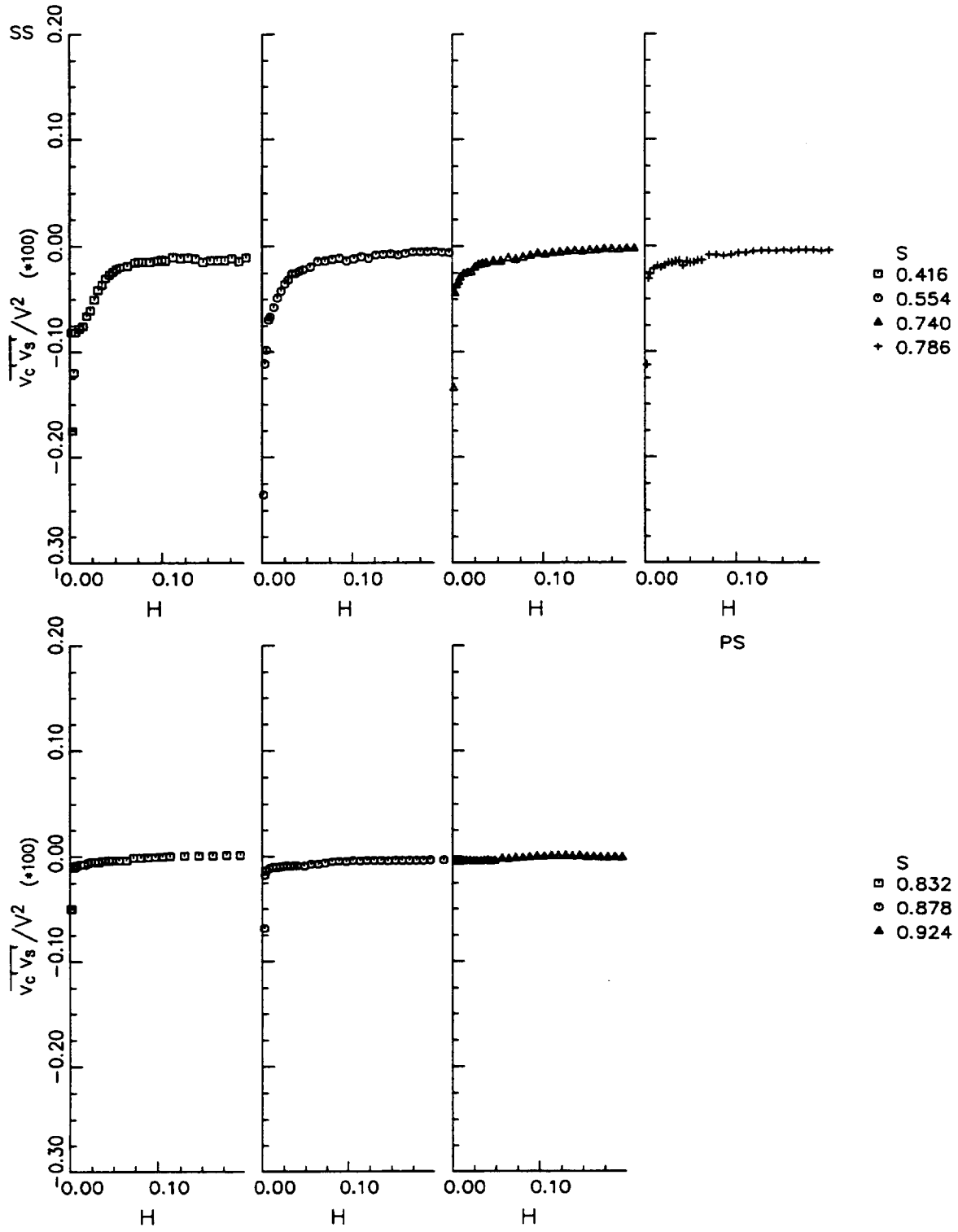

Figure 5. 39 Measured velocity correlation on hub endwall at x/c_m=0.95. SS - Suction Surface, PS - Pressure Surface.

exhibits characteristics of isotropic turbulence. The only measurement location where an appreciable difference between the cross wise and stream wise turbulence components is present is the location closest to the pressure surface (S=0.924). The crosswise component of velocity on the pressure surface is relatively small (compared to the suction surface).

Measurements of the Reynolds stress term (Figure 5.39) show an increase in the correlation term ($\overline{v_s' v_c'}$) toward the suction side. At locations close to the pressure surface, the correlation between the streamwise and the crosswise fluctuating velocities is small and is consistent with a thin boundary layer thickness, reported earlier.

5.4.4 Pressure Surface Turbulence Properties

Along the pressure surface of the nozzle blade, the flow visualization experiments indicated that the boundary layer is laminar in nature almost up to the trailing edge of the blade. The measurements at x/c_m=0.945, shown in Figures 5.40, 5.41, and 5.42 indicate that the boundary layers are turbulent or transitional near the trailing edge. This is confirmed by comparing the turbulence intensity at the corresponding locations on the suction surface (Figure 5.31). At this chordwise location the boundary layer seems to be turbulent all the way from hub-to-tip. The increase in turbulence in freestream turbulence is due to the potential effect of the down stream rotor (see section 5.3) on the vane boundary layer.

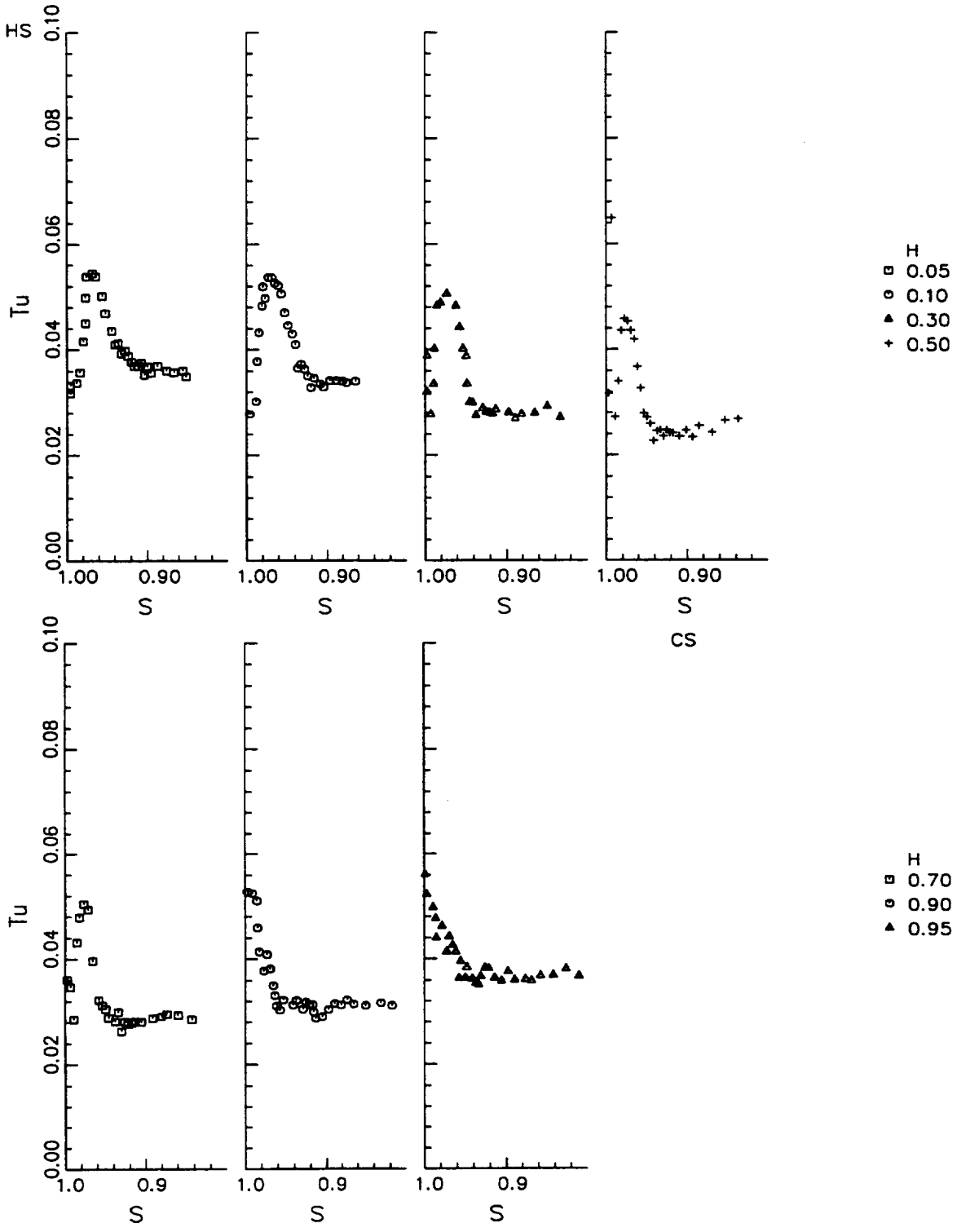

Figure 5. 40 Measured Total Turbulence Intensity on Pressure Surface at x/c_m=0.945. HS - Hub Surface, CS - Casing Surface.

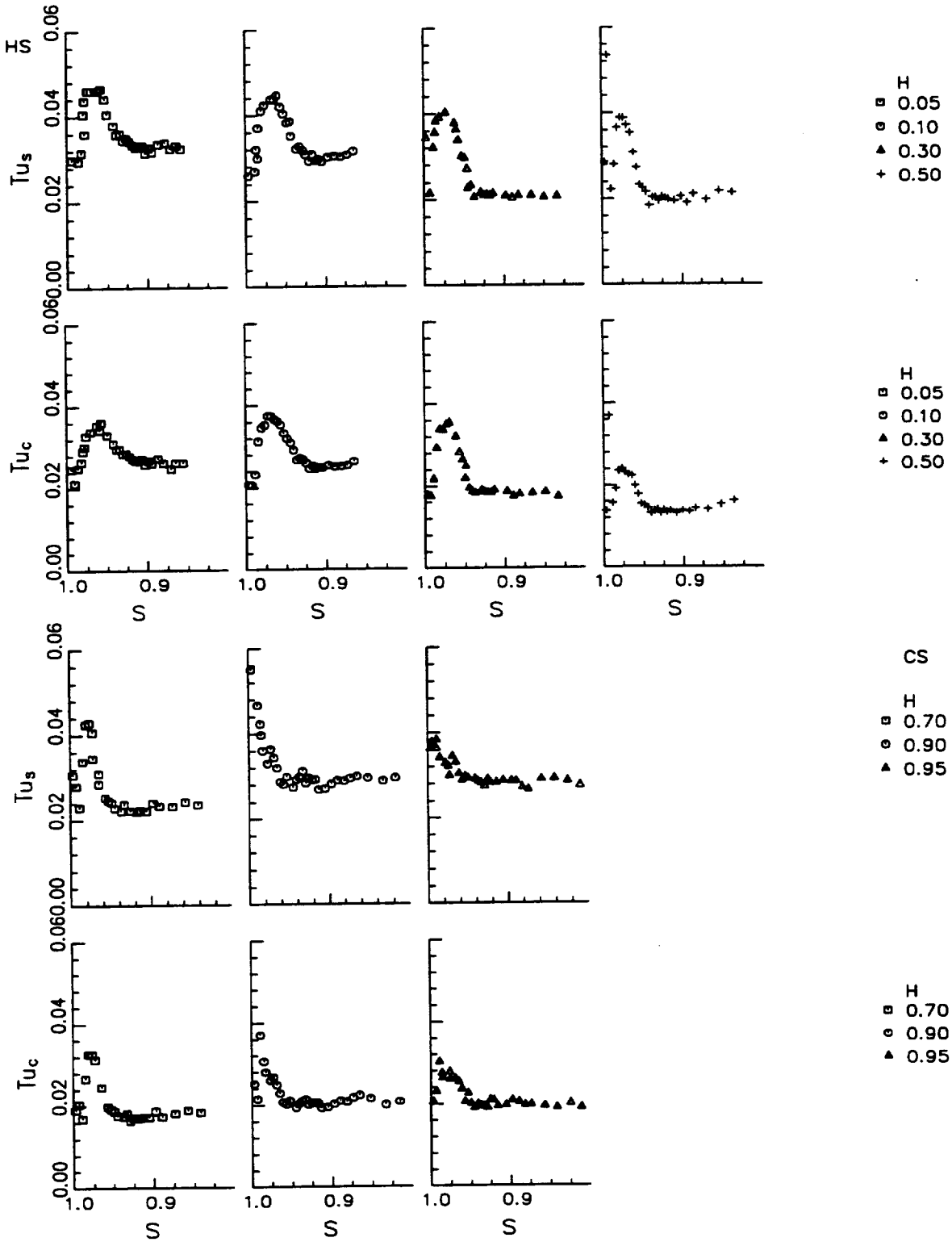

Figure 5. 41 Measured components of Turbulence intensity in the stream wise and cross wise direction at x/c_m=0.945. HS - Hub Surface, CS - Casing Surface.

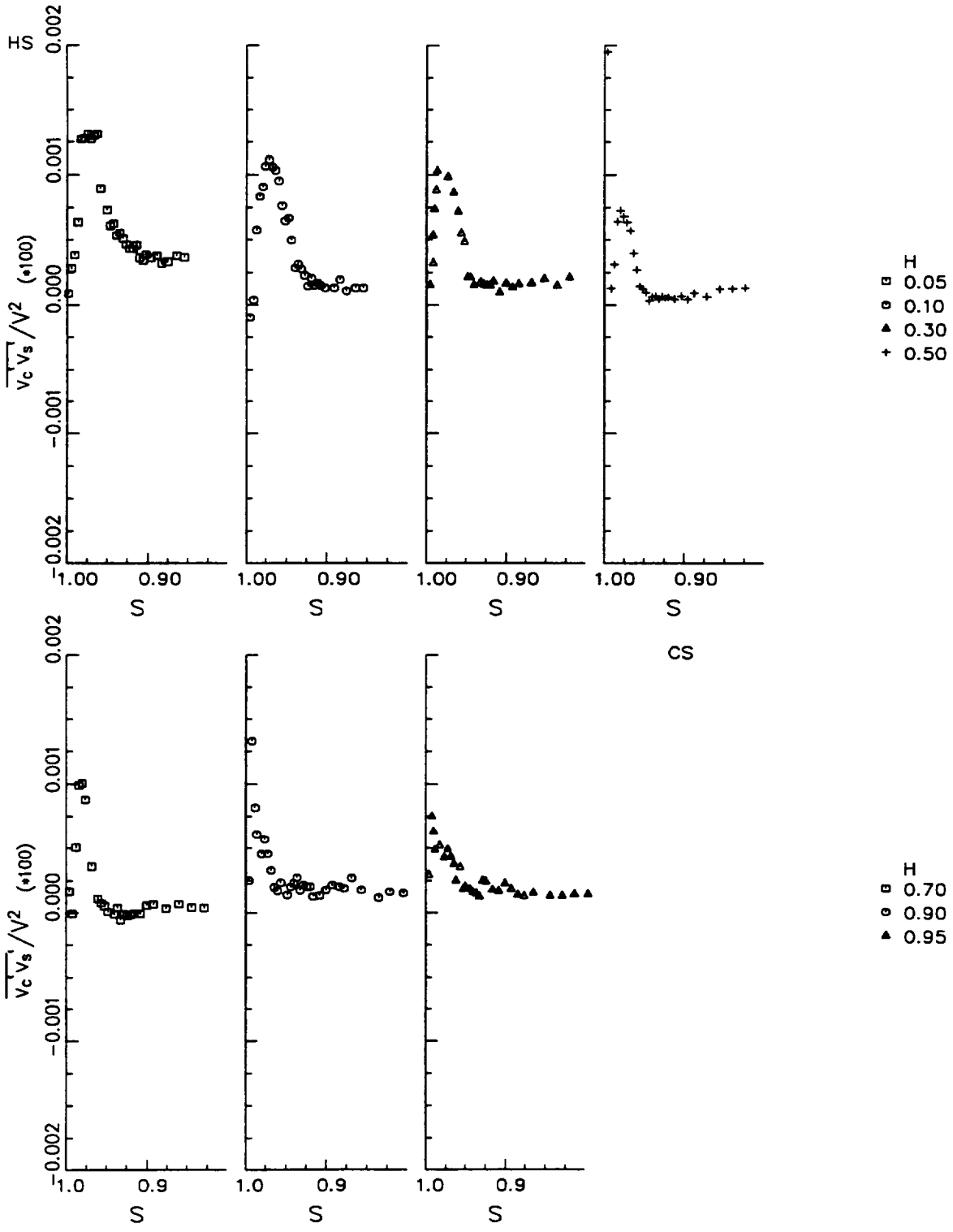

Figure 5. 42 Measured Velocity Correlation at x/c_m=0.945. HS - Hub Surface, CS - Casing Surface.

The measured Reynolds stress (Figure 5.42) is much smaller than those on the suction surface (Figure 5.31) indicating a very low correlation between the velocity fluctuations. In the free stream, since the main influence on the unsteadiness is the downstream rotor and fan, the velocity fluctuations are in phase (periodic) and the correlation is very low. In the boundary layer region and close to the trailing edge of the blade the fluctuations in the two measurement directions are damped at a different rate, thereby increasing the measured velocity correlation term.

In the free stream the turbulence intensity remained constant (close to 2.5 %) and did not change dramatically from the x/c_m =0.945 and 0.56 location. In general the free stream level of turbulence remained close to constant through out the nozzle passage.

5.5 Secondary Flow Region

Measurements in the suction- casing surface corner could be used to evaluate the extent of secondary flow, including the interaction between endwall and blade boundary layers, and the casing passage vortex. Measurements in the hub- suction corner could not be obtained due to access problems. The streamwise and crosswise components of velocity in the secondary flow region are shown in Figure 5.43. The small crossflows observed in the freestream may be due to the inaccuracy of the assumption that the flow is parallel to the blade surface and the alignment of the probe.

Maximum radial inward flow occurs at H=0.80, decreasing gradually to zero as the

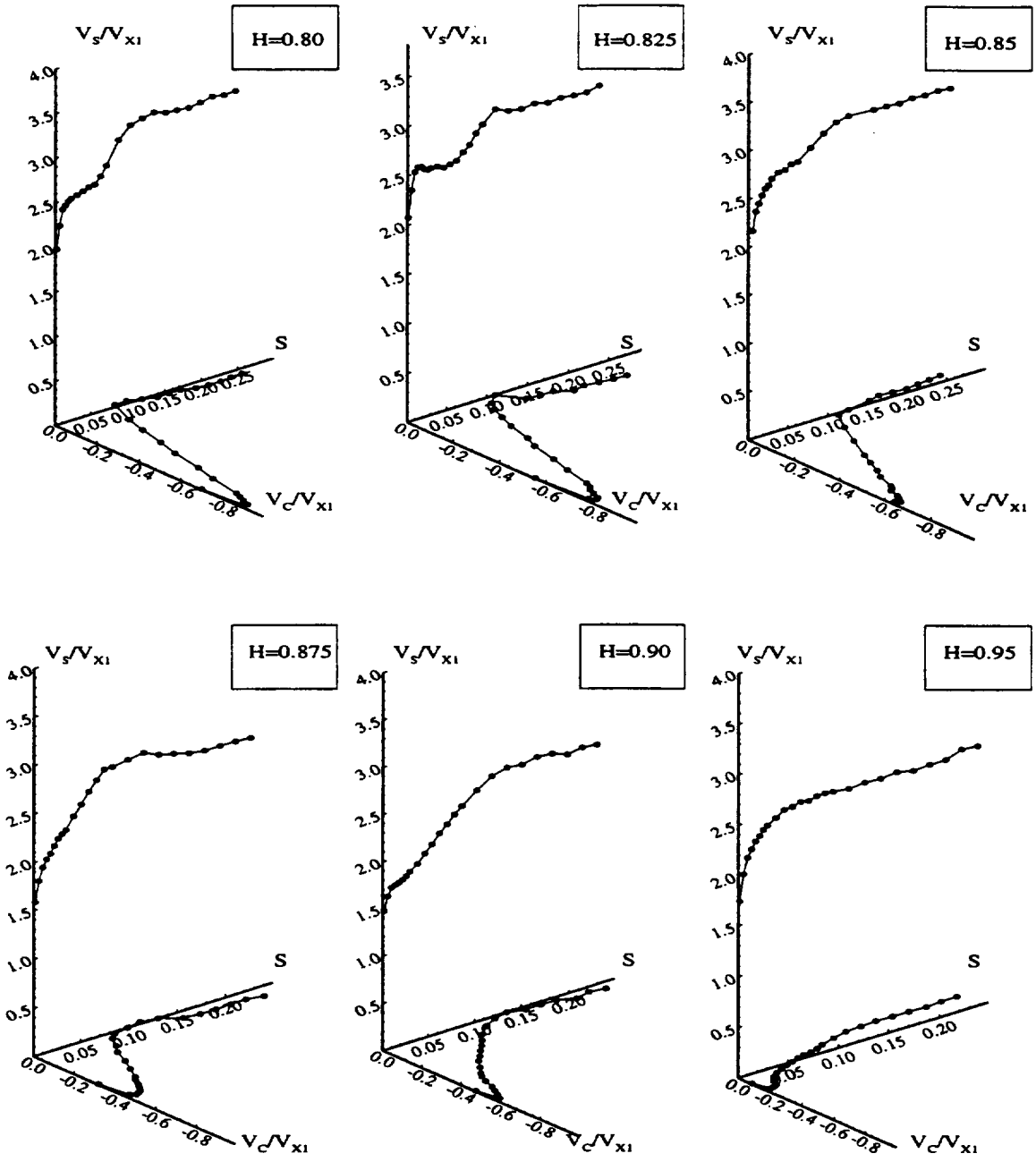

Figure 5. 43 Stream wise and cross wise velocity components in the casing-suction surface corner. (x/cm =0.85)

wall is approached. The radial flow due to the passage vortex and the radial flow due to the radial pressure gradient is in the same direction, hence the radial inward flow is augmented near the suction surface of the suction-casing corner. The spanwise locations along H=0.80 to H=0.825 represent the passage vortex. The spanwise station at H=0.95 is within the casing boundary layer and away from the secondary flow region.

Using the six measurement locations on the blade suction surface shown, as well as the casing wall boundary data, described in section 5.1.2, the measured flow properties can be interpolated to provide a composite and comprehensive understanding of the flow field.

The total velocity normalized by V_{x1} in the secondary flow region is shown in Figure 5.44. In the corner region, a slight increase in the measured velocity can be attributed to the flow overturning. The casing passage vortex, where the velocity minimum, is located close to the H=0.90 location near the suction surface. The velocity decreases in the blade boundary layers outside of the casing passage vortex.

Measured radial flow angles, presented in Figure 5.45, indicate radial inward flow over the entire region, with the maximum values occurring near H=0.79 to 0.9 locations. The magnitude of the radial flow angle decreases away from these regions. In the free stream, the radial flow angle is very low and is consistent with measurements taken by Zaccaria (1994) at x/c_m =0.935 using a pneumatic five hole probe. Close to the casing surface, the radial inward flow angle again decreases away from the corner, indicating that most of the radial flow occurs in the suction-casing surface corner.

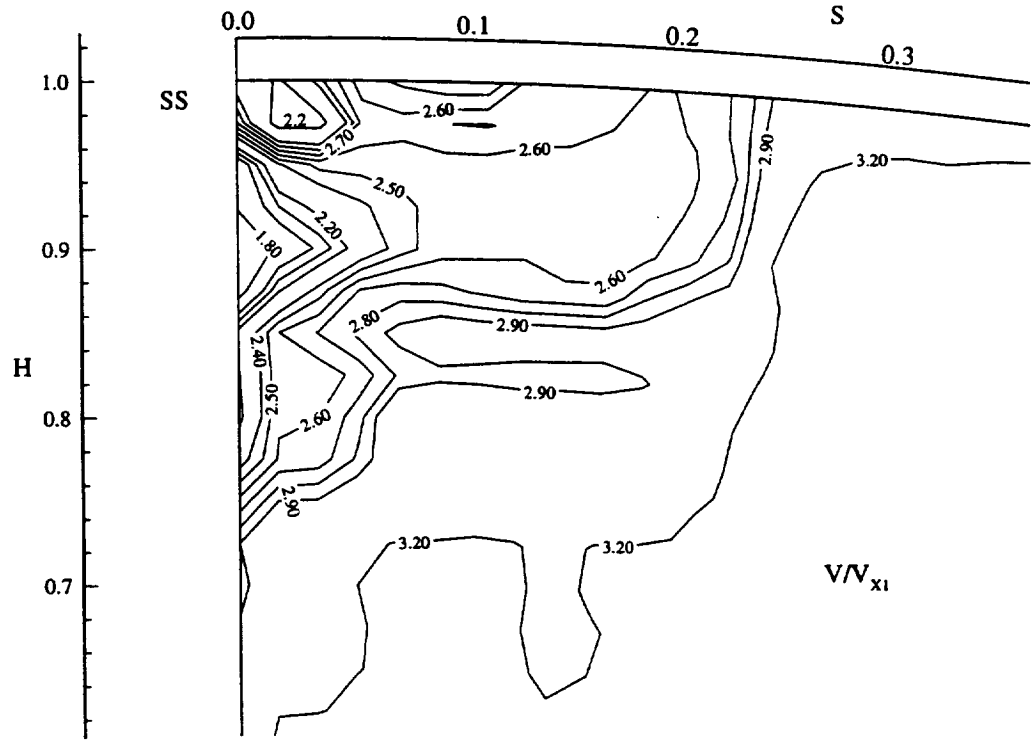

Figure 5. 44 Total Velocity Contours, Casing Suction Surface Corner. x/c_m =0.85.

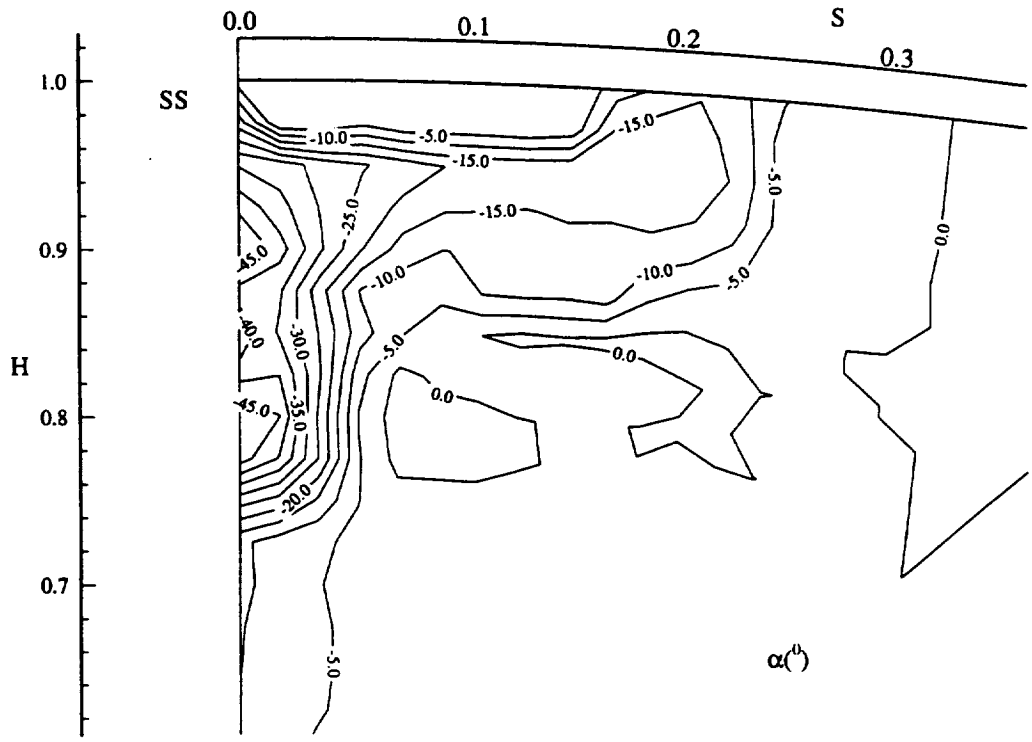

Figure 5. 45 Contours of Measured Radial Angle (in degrees) in the secondary flow region. x/c_m=0.85.

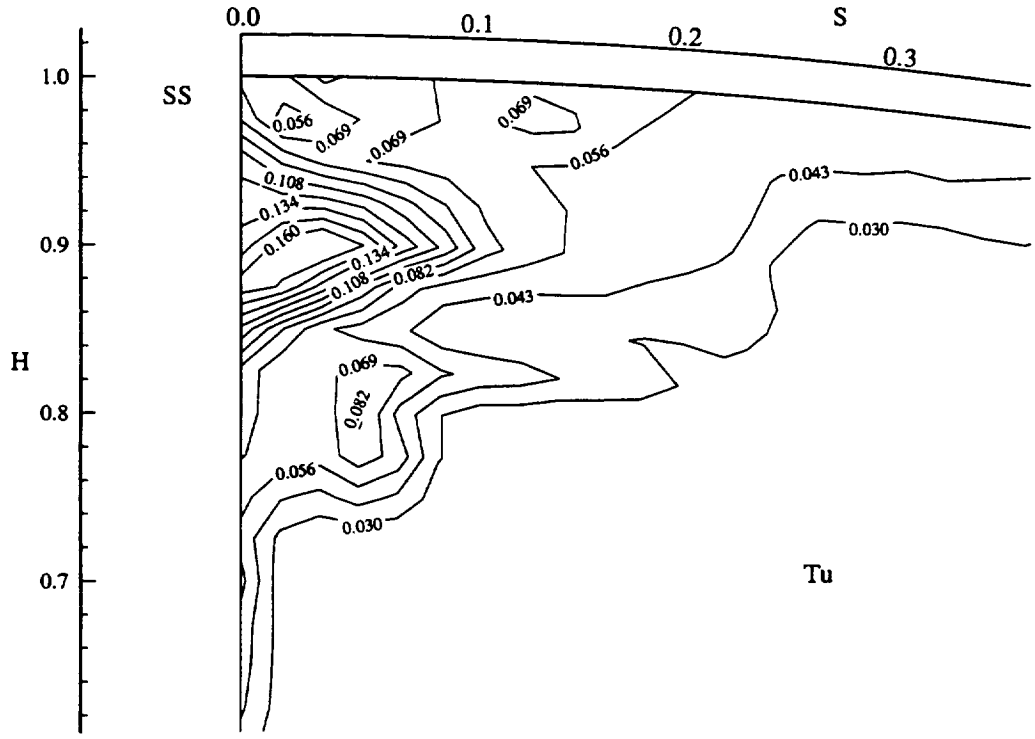

Figure 5. 46 Total Turbulence Intensity Contour (Equation 5.5). Casing-Suction surface corner, x/c_m=0.85.

The turbulence intensity (Tu) in the casing - suction surface corner (Figure 5.46) increases to a maximum value of 0.18 near the vortex core. Outside the corner, the freestream the turbulence intensity decreases dramatically to a average level of 0.03. The turbulence intensity in the casing endwall decreases toward the pressure surface, due to a decrease in the boundary layer thickness. The turbulence intensities decreases toward the pressure surface on both the casing and endwall surface.

The distribution of the velocity correlation, or Reynolds stress shown in Figure 4.47, indicates that the maximum value is centered around the H=0.875 location. The reversal in the sign of the $\overline{v_s' v_c'} / V^2$ term occurs due to the passage vortex in the secondary flow region. In the free stream, the measured velocity correlation is very low, increasing only slightly in the near wall regions. A slight increase in the measured $\overline{v_s' v_c'} / V^2$ occurs at H=0.96 due to the presence of a weak corner vortex. Along the suction surface, the correlation decreases toward midspan following the trend exhibited in turbulence intensity contours (Figure 5.46). In the casing endwall region the Reynolds stress term decreases toward zero over most of the pitch. It should be remarked here that the correlation $\overline{v_s' v_c'}$ is not the dominant Reynolds stress term. The dominant Reynolds stress term close to the surface is $\overline{v_s' v_n'}$ which could not be measured in the hot wire probe configuration employed in this investigation.

The increase in unsteadiness was localized in the secondary flow region, extending approximately from H=0.8 to the casing surface in the radial direction and from the

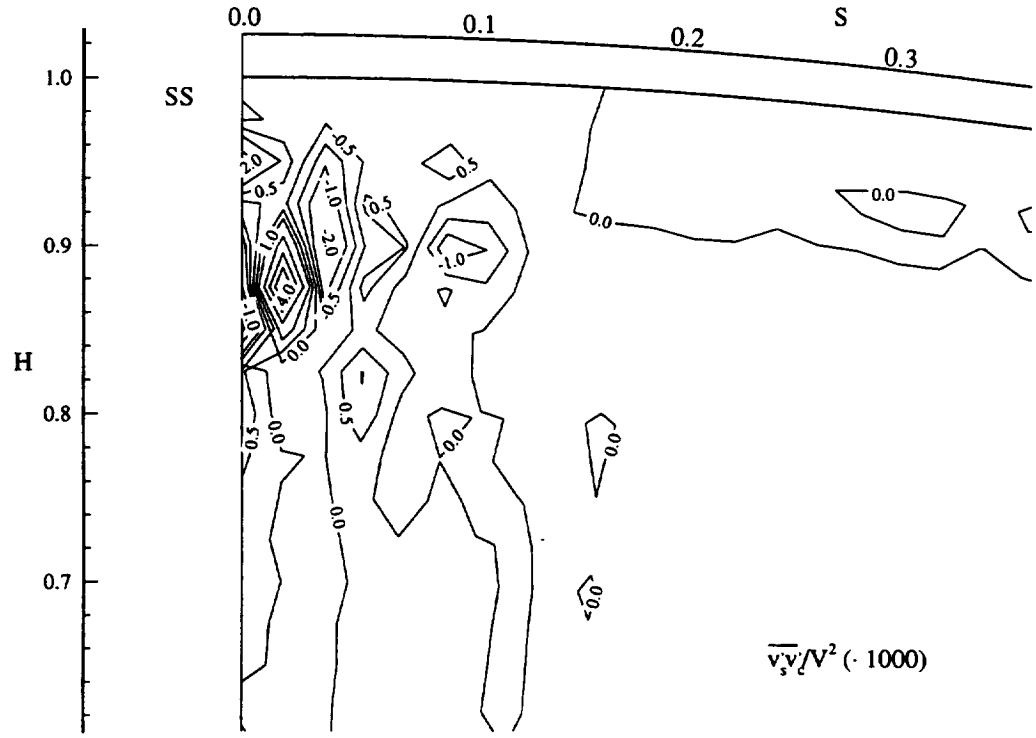

Figure 5. 47 Velocity Correlation $\overline{v_s' v_c'}$ in Suction- Casing Surface Corner. (x/c_m=0.85)

suction surface to S=0.19 in the pitch wise direction. The presence of the weak corner vortex could only be detected through an increased turbulence intensity and correlation.

CHAPTER 6

CONCLUSIONS AND RECOMMENDATIONS

Measurements in the nozzle passage of the AFTRF facility were performed using various experimental techniques, including surface static pressure measurements, x-wire anemometry, 2D LDV measurements, and flow visualization. The experimental results were compared with predictions of the flow using a quasi- three dimensional inviscid and a three dimensional boundary layer code. Measurements in the nozzle passage indicated very thin boundary layers over most of the blade suction and pressure surfaces. Thicker, turbulent boundary layers were measured only close to the trailing edge of the suction surface. Near the casing and hub endwalls, the viscous layers were more developed and turbulent in nature, with complex features observed due to interaction between the secondary flow and the annulus wall boundary layer.

6.1 Nozzle Passage Boundary Layers

The major conclusions that are drawn from the investigation described here can be summarized as follows:

1. The boundary layers on the pressure surface of the nozzle vane blade are laminar up to the trailing edge due to the presence of favorable pressure gradient that exists in this

region and low free stream turbulence at the inlet and in the nozzle free stream. Based on flow visualization experiments and seven radial surveys at x/c_m=0.945 the viscous layer was found to be very thin , δ^*/c_t=0.001 on the pressure surface at the midspan, compared to δ^*/c_t=0.002 at the suction surface, midspan.

2. On the suction surface of the blade, the boundary layers remain laminar over most of the blade passage up to approximately x/c_m=0.7, where the adverse pressure gradient influences the transition to turbulent flow. Outside the secondary flow region in the casing-suction surface corner, the boundary layers are thin (δ/c_t=0.014 at midspan) and are well behaved with a fairly strong crosswise flow due to the radial inward pressure gradient (β=-7° at H=0.5, β=-14° at H=0.70, suction surface, at closest measurement locations).

3. The boundary layer on the casing endwall surface is found to be much thicker than that on the hub endwall boundary layer due higher flow turning and larger secondary flow in this region. The velocity profiles in the casing-suction corner indicate wake like behavior due to the presence of a passage vortex. The velocity increases in the near wall region due to the interaction of the secondary flow region and the casing endwall boundary layer. Boundary layer thickness and turning of the flow decreases as the pressure surface is approached. The minimum static pressure location occurs earlier on the suction surface (at x/c=0.5) near the casing than that on the hub endwall (at x/c=0.81).

4. The secondary flow is much stronger in the casing-suction corner due to the presence of strong transverse pressure gradient, thicker inlet boundary layer, earlier lifting of the

passage vortex from the wall on the casing-suction surface corner, than observed on the hub-suction corner.

5. The secondary flow region in the suction-casing surface corner indicate the presence of the passage vortex detached from the blade surface. The radial inward flow along the suction surface in this region moves the passage vortex inward. The corner vortex is very weak and is marked by a slight increase in the unsteadiness.

6. The presence of a secondary flow region in the suction-casing surface corner results in a change in the sign of the measured velocity correlation ($\overline{v_s' v_c'}$) from positive to negative on either side of the passage vortex. The stream wise and cross wise velocity fluctuations were uncorrelated in the free stream region as expected. In the viscous region close to the surface of the blade and endwalls, the measured Reynolds stress increases.

7. Boundary layer thickness increase initially along the pressure surface of the blade up to approximately x/c=0.4, beyond which the integral properties decreases due to the presence of favorable pressure gradient. Along the suction surface, the boundary layer thickness increases smoothly up to the transition location (x/c=0.7) beyond which the boundary layers exhibited characteristic thickening toward the trailing edge.

8. The close nozzle-rotor spacing (20% of the nozzle chord length at midspan) results in an appreciable potential interactions within the nozzle flow field. Filtering of the rotor blade passing frequency signal removed the periodic unsteadiness due to the rotor and the fan and decreased the turbulent intensities from 2.1% to 1% at x/c_m=0.945. The random

unsteadiness in the blade passage is found to be smaller than the measured total unsteadiness.

9. Measurements of the Lagrangian integral length scale close to the trailing edge of the nozzle blade were determined to be appreciable (close to 2.2% of axial chord), indicating low turbulence dissipation rates. Digital filtering of the signal did not affect the length scale (filtering removed only the periodic fluctuations from the rotor and fans). LDV measurements in the nozzle passage at x/c_m=0.56 and hot wire probe measurements at x/c_m=0.85, 0.94, and 0.945 indicate that the turbulence intensity in the freestream remained constant through out the blade passage. Digital filtering proved to be a good technique in removing the rotor and auxiliary fan influence.

6.2 Three Dimensional Boundary Layer Prediction

Based on a comparison between the predicted and the measured boundary layer properties the following conclusions are drawn:

1. Prediction of the integral properties, i.e. momentum thickness, displacement thickness, and shape factor shows good agreement except in regions of secondary flow and endwall boundary layer flow, where the conventional boundary layer assumptions are no longer valid. On the suction surface, the solution was accurate from H=0.1 to H=0.7, with good agreement of the measured streamwise velocity profile. On the nozzle vane pressure surface, the agreement was even better due to the smaller extent of the secondary flow

region and the endwall boundary layers.

2. The procedure proved very difficult to implement along the endwall surfaces due to the inflow conditions along the blade-endwall boundaries. Specification of accurate external flow properties, in this case the nozzle passage static pressure distribution, and appropriate inflow conditions where critical for good predictions.

3. The accuracy of the solution is strongly dependent on the choice of grid spacing, especially in the normal direction. Accurate predictions were not obtained with less than 70 points in the normal direction.

6.3 Recommendations

Measurements performed during this experimental investigation allowed insight in to the development of a three dimensional boundary layer in a modern turbine nozzle vane passage. The realistic rotor-stator spacing and modern blade design enabled measurement of unsteadiness due to the rotor potential effect and the downstream fans in a turbine stage exemplary of current jet engine designs.

Future measurements could include hot film measurements along the suction surface to accurately locate the transition region in both the radial and axial directions, including unsteady transition phenomenon. Measurements should be acquired using a shaft encoder to remove the periodic unsteadiness from the rotor. Digital filtering described in

this research could be used to remove the influence of the downstream fans. Measurements downstream of the trailing edge using a miniature three sensor hot wire probe could enable determination of the unsteadiness in the secondary flow region and fully define the inflow conditions to the rotor. Addition of upstream turbulence generating mechanisms could lead to exploration of high inlet turbulence flows typical of turbine inlet conditions. In addition the high influence on unsteadiness of the downstream auxiliary fan should be decreased.

REFERENCES

Anand, A. K., and Lakshminarayana, B. " An Experimental Study of Three-Dimensional Turbulent Boundary Layer and Turbulent Characteristics Inside a Turbomachinery Rotor Passage,", ASME Journal of Engineering for Power, Vol. 100, 1978.

Anderson, O.L., "Assessment of a 3-D Boundary Layer Analysis to Predict Heat Transfer and Flow Field in Turbine Passage," NASA CR-174894, August 1985.

Bammert, K., and Sandsede, H., "Measurements of the Boundary Layer Development along a Turbine Blade with Rough Surface," ASME Paper 80-GT-40, 1980.

Blanco, E., Ballesteros, R., and Santolaria, C., "Angular Range And Uncertanty Analysis Of Non-Orthogonal Crossed Hot Wire Probes," ASME *Thermal Anemometry*, FED-Vol.167, 1993.

Blottner, F.G., "Finite Difference Method solution of the Boundary Layer Equations," AIAA Journal, Vol. 18, p.193-205, February 1970.

Bruscher, W.A., Grano, R.S., and McLaughlin, M.D., "Recomended Noise Control Design for The Hammond Wind Tunnel," ACS 497 Noise Control, Fall 1993.

Cebeci, T., and Smith, A. M. O., Analysis of Turbulent Boundary Layers, Academic Press, New York, 1974.

Deutsch, S., and Zierke, W. C., "The Measurement of Boundary Layers on a Compressor Blade in Cascade: Part 1 - A Unique Experimental Facility," ASME Journal of Turbomachinery, Vol. 109, October 1987.

Dhawan, S., and Narasimha, R., "Some Properties of Boundary Layer Flow During Transition from Laminar to Turbulent Motion," Journal of Fluid Mechanics,Vol. 3, 1958.

Dryden, H. L., "Air Flow in the Boundary Layer Near a Plate," NACA TR 562, 1936.

Hawthorne, W.R., "Rotational Flow Through Cascades," J. Mech. & Appl. Math., Vol. 3, 1955.

Hinze, O. J., Turbulence, McGraw Hill, New York, 1959.

Hodson, H. P., "The Development of Unsteady Boundary Layers on the Rotor of a Axial Flow Turbine," AGARD-CP-351, June 1983.

Holman, J.P.,Experimental Methods for Engineers, McGraw Hill, 1984.

Johnston, J. P.,"On Three-Dimensional Turbulent Boundary Layer Generated by Secondary Flow," Journal of Basic Eng., vol. 82., pp.233-248. 1960.

Katsanis, T., and McNally, W., "Revised Fortran Program For Calculating velocities and Streamlines on the Hub-Sroud Midchannel Stream Surface of an Axial-, Radial-, or Mixed Flow Turbomachine or Annular Duct. I - Users Manual," NASA TN D-8430, 1977.

King, L.V., "On The Convection Of Heat From Small Cylinders In A Stream Of Fluid: Determination Of The Convection Constants Of Small Platinum Wires With Applications To Hot-Wire Anemometry," Phil. Trans. Roy. Soc. A, 1914.

Klein, A., "Investigation of the Entry Boundary Layer on the Secondary Flows in the Blading of Axial Turbines," BHRAT 1004, 1966.

Krause, E. and Fernholtz, H. H., Editors, "Three Dimensional Turbulent Boundary Layers," IUTAM Symposium, Springerverlag, Belgium/Germany, 1982.

Lakshminarayana, B., Hah, C., and Govindan, T., "Experimental Study of the Boundary Layer on a Turbomachine Rotor Blade," in: *Three Dimensional Turbulent Boundary Layers*, IUTAM Symposium, Springerverlag, Berlin, 1982.

Lakshminarayana, B., Hah, C., and Govindan, T., "Three Dimensional Turbulent Boundary Layer Development on a Fan Rotor Blade," AIAA Journal, V22, pg 83-89, January 1984.

Lakshminarayana, B., Camci, C., Halliwell, I., and Zaccaria, M., "Investigation of the Three Dimensional Flow Field in a Turbine Including Rotor/Stator Interaction. Part 1: Design, Development and Performance of Turbine Facility," AIAA paper 92-3325, 1992.

Langston, L. S., Nice, M. L., and Hooper, R. M., "Three Dimensional Flow Within a Turbine Blade Passage," ASME Journal of Engineering for Power, Vol. 99, No. 1, pg. 21-28, Jan. 1977.

Lomas, C. G., Fundamentals of Hot Wire Anemometry, Cambridge University Press, Cambridge, 1986.

McLaughlin, D. K., Tiederman, W. G., "Biasing Correction for Individual Realization of Laser Anemometer Measurements in Turbulent Flow," Physics of Fluids, December, pp. 2082-2088, 1973.

Mee, D.J., Baines, N.C., and Oldfield, M.L.G.,"Detailed Boundary Layer Measurements on a Transonic Turbine Cascade,"ASME Journal of Turbomachinery,Vol. 114, 1992.

Mellor, G. L., and Herring, H. J. "Simple Eddy Viscosity Relations for the Three Dimensional Turbulent Boundary Layers," AIAA Journal, Vol. 15, No. 6, 1977.

Moore, J., Smith, B.L., "Flow in a Turbine Cascade. Part 2: Measurement of Flow Trajectories by Ethylene Detection," ASME Paper 83-GT-69, 1983.

McFarland, E.R., "Solution of Plane Cascade Flow Using Improved Surfface Singularity Methods," ASME Paper 81-GT-169, 1981.

Oka, S., and Kostic, Z., "Influence of Wall Proximity on Hot-wire Velocity Measurements," DISA Info., 13, 1972.

Patterson, R. W., "Turbofan Forced Mixer-Nozzle Internal Flowfied, I - A Benchmark Experimental Study" NASA CR-3492. April 1982.

Patrick, W. P., "Flowfield Measurements in a Separated and Reattached Flat Plate Turbulent Boundary Layer," NASA Contractor Report 4052, March 1987.

Pouagare, M., Galmes, J. M., and Lakshminarayana, B., "An Experimental Study of the Compressor Rotor Blade Boundary Layer," ASME Journal of Engineering for Gas Turbines and Power, Vol. 107, 1985.

Radeztsky, R. H., Jr., Reibert, M. S., and Takagi, S., "A software Solution to Temperature-induced Hot-wire Voltage Drift," ASME *Thermal Anemometry*, FED-Vol.167, 1993.

Sieverding, C. H., "Recent Progress in the Understanding of Basic Aspects of Secondary Flows in Turbine Blade Passages," ASME Journal of Engineering for Gas Turbines and Power, Vol. 107, April 1985.

Squire, L.C., "The Three Dimensional Boundary Layer Equations and Some Power Series Solutions," ARC Tech. Rpt. R&M 3006, 1957.

Strazisar, A. J., "Application of Laser Anemometry to Turbomachinery Flowfield Measurements," VKI LS 1985-03, 1985.

Tennekes, H., and Lumley, J. L., A First Course in Turbulence, MIT Press, Cambridge, 1972.

Vatsa, V.N., "A Three Dimensional Boundary Layer Analysis for Turbomachinery Applications," UTRC Report No. 84-44, 1984.

Vatsa, V.N., "A Three Dimensional Boundary Layer Analysis Including Heat Transfer and Blade Rotation Effects" Paper presented at the Third Symposium of Numerical and Physical Aspects of Aerodynamic Flows, Long Beach California, January 1985.

Vatsa, V.N., and Davis, R.T., "The Use of Levy-Lees Variables in 3-D Boundary Layer Flows," NASA CR-112315, January 1973.

Werle , M.J., and Verdon, J.M., "Viscid/Inviscid interaction Analysis for Symmetric Trailing Edges," UTRC Report R79-914493-5, January 1980.

Yavuzkurt, S., "A Guide to Uncertanty Analysis of Hot- Wire Data,"Journal of Fluids Engineering, Vol. 106, June 1984.

Zaccaria, M., Ristic, D., and Lakshminarayana, B., "Three Dimensional FlowField in a Turbine Nozzle Passage," AIAA/SAE/ASME/ASEE 29th Joint Propulsion Conference and Ehibit, Monterey, 1993.

Zaccaria, M., "An Experimental Investigation into the Steady and Unsteady Flow Field in a Axial Flow Turbine," PhD. Thesis, The Pensylvania State University, 1994.

APPENDIX A

ACOUSTIC MEASUREMENTS

During the operation of the AFTRF the noise level in the room without any sound absorption panels reaches very high levels. The acoustic energy radiated throughout the laboratory can influence the measurements during standard operation.

Measurements on the AFTRF performed by Bruscher et. al. (1993) included the determination of the acoustic sound field at various locations around the facility. The measurements where taken using a 1/3 octave sound pressure meter at five locations shown in Figure A.1. During normal operation of the facility, the two fans operate at a constant speed of 1770 RPM. The fans each with 16 rotor and 16 stator blades have resultant blade passing frequency of 472 Hz. A measurement location one axial chord upstream of the nozzle passage used to obtain x-wire measurements (Data Point #1) showed a very high level of acoustic energy in the frequency range of approximately 500 Hz (see Figure A.2). The maximum level reached is 125.6 dB with no apparent higher order harmonics. The very high level of acoustic energy was also apparent in the frequency spectrum of the hot-wire signal shown in Figure 5.26 and 5.27. At the downstream location (Data Point #2), the maximum level reached was even higher - 134.1 dB at the fan blade passing frequency.

In the regions away from the facility (Data points #3,4, and 5) the noise level was still appreciably high, averaging around 90 dB over a broad band of frequencies. The

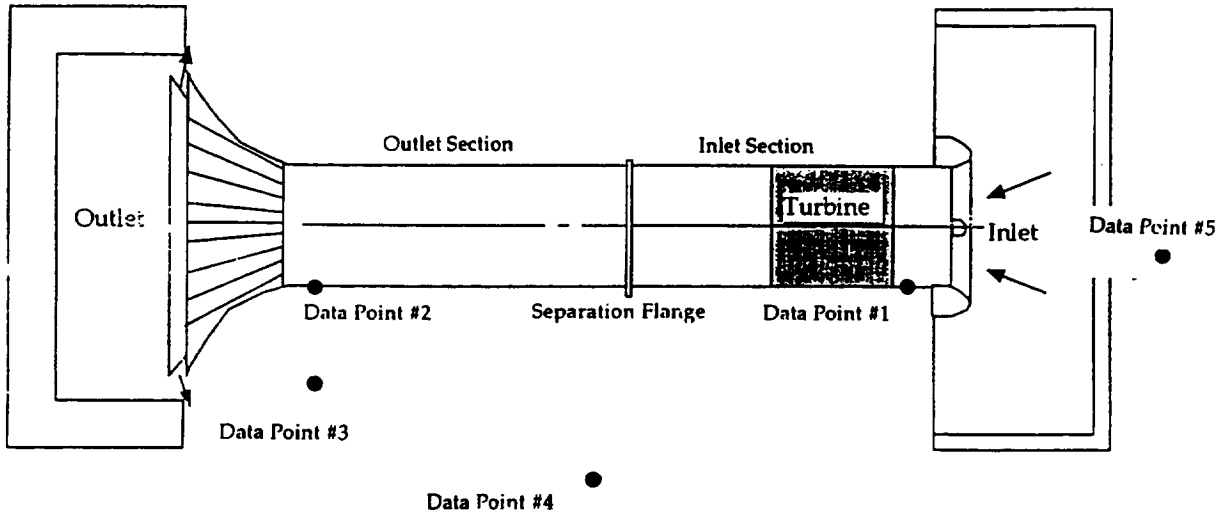

Point #1 - in the wind tunnel tube, just before the turbine.
Point #2 - in the wind tunnel tube just after the fans.
Point #3 - just outside the wind tunnel outlet and after the custom silencer cone
Point #4 - at operators station
Point #5 - just outside of the inlet and before the filter section.

Figure A. 1 Sound pressure level measurement locations around the AFTRF. Source Bruscher et. al. (1993).

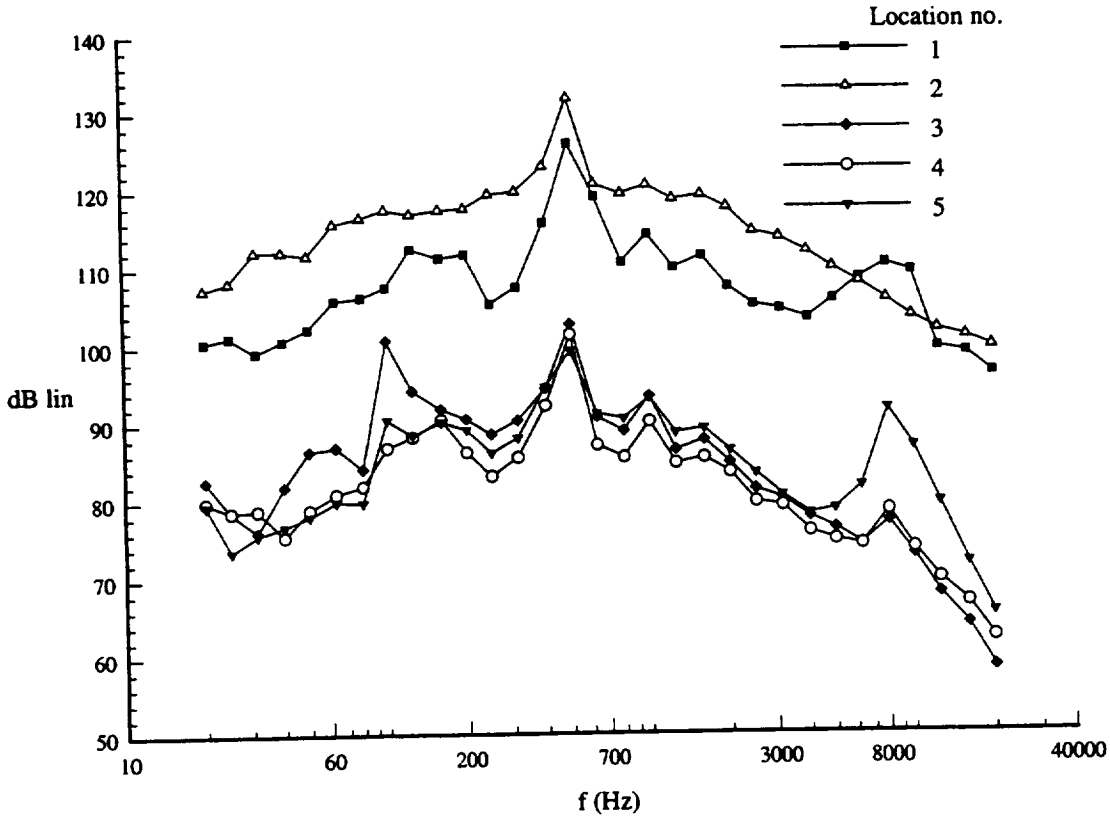

Figure A. 2 Measured sound pressure level at various measurement locations. Source Bruscher et. al. (1993).

increase at higher frequencies is probably due to the room reflections.

In future measurements, acoustic treatment of the inlet and outlet enclosures should alleviate the high level of noise present in the laboratory, but the influence on the unsteady measurements from the fans will remain and must be dealt with through the use of some post processing scheme, such as the one described in section 5.4.

APPENDIX B

HOT WIRE UNCERTAINTY ANALYSIS

The accuracy of hot wire measurements should be evaluated to access the accuracy of the measured properties. The sources of error include: voltmeter error, flow angularity error, ambient temperature drift, and velocity calibration error. Each of these sources are discussed below.

B.1 Probe Calibration

The cross wire, two sensor hot wire was calibrated in a low turbulence (< 1.0 %) calibration jet. The sensor was placed perpendicular to the flow. The probe was calibrated over a range of velocities from 0 to 120 m/s. A pitot-static probe connected to a manometer was used to measure the calibration jet velocity. The air velocity measured by the pitot-static probe is given by

$$V = \left(\frac{2RT\rho_{H_2O}gh}{p} \right)^{\frac{1}{2}} \tag{B.1}$$

where h is the manometer reading in inches of water. The manometer is used to measure the difference between the static and total pressures for the pitot-static probe. The error in reading the manometer is 0.025 inches of water. The uncertainty for the thermometer and barometer quoted by the manufacturer are 0.1 °K and 0.05 inches of Hg, respectively.

The significant source of error results from the pitot-static tube installation. According to

Holman (1984), the major source of error in a low turbulence flow away from solid surfaces is due to probe misalignment. The error due to the pitot-static installation is then 0.02 inches of water.

Based on these estimates the error in velocities is 0.8 percent.

B.2 Measurement Errors

The velocity measured by the hot wire sensor is obtained from King's law which is

$$E^2 = A + BV^{0.45} \tag{B.2}$$

where E is the anemometer output voltage taken across the Wheatstone bridge in the anemometer, V is the fluid velocity and A and B are the calibration constants. The uncertainty in the measured velocity is thus

$$U_V = \left[\left(\frac{\partial V}{\partial E}U_E\right)^2 + \left(\frac{\partial V}{\partial A}U_A\right)^2 + \left(\frac{\partial V}{\partial B}U_B\right)^2\right]^{\frac{1}{2}} \tag{B.3}$$

To find U_V, the uncertainties in E, A and B need to be found first. The error stated by the manufacturer for the anemometer bridge output voltage and the voltmeter output voltage are

$$U_{E_1} = 0.0002V \tag{B.4}$$

$$U_{E_2} = 0.002V \tag{B.5}$$

and the error due to reading the voltmeter is

$$U_{E_3} = 0.0005V \tag{B.6}$$

Another source of error that can change the anemometer output voltage is ambient

temperature drift. A change in ambient temperature causes a change in the heat transfer rate of the sensors. This results in a corresponding change in the measured output voltages from the anemometer. A correction scheme is used to correct the variation in anemometer output voltage due to temperature. Thus this error is neglected. The total uncertainty in E is then found from

$$U_E = \left(U_{E_1}^2 + U_{E_2}^2 + U_{E_3}^2\right)^{\frac{1}{2}} \tag{B.7}$$

The calibration constants A and B are obtained by fitting a straight line in the form

$$\ln A = A \ln V + B \tag{B.8}$$

through the calibration data. The uncertainty in A and B are then obtained from the equations

$$U_A = \left[\left(\frac{\partial A}{\partial E} U_E\right)^2 + \left(\frac{\partial A}{\partial V} U_V\right)^2\right]^{\frac{1}{2}} \tag{B.9}$$

$$U_B = \left[\left(\frac{\partial B}{\partial E} U_E\right)^2 + \left(\frac{\partial B}{\partial V} U_V\right)^2\right]^{\frac{1}{2}} \tag{B.10}$$

($\partial A/\partial B$ and $\partial B/\partial A$ are assumed to be zero.) Thus, substituting the uncertainties in A, B and E into equation (B.3) along with the nominal values for A, B and E yields

$$\frac{U_V}{V} = 1.9\ \% \tag{B.11}$$

which is the total uncertainty in the measured velocity. Yavuzkurt (1984) states that the

mean and rms components of velocity have the same percent error, thus

$$\frac{U_{Tu}}{Tu} = 1.9\ \% \tag{B.12}$$

which is the total uncertainty in the measured turbulence intensity.

The uncertainty in the angular measurement of the coefficients A_α and U_{cf} is defined by Blanco, Ballestros and Santolaria (1993) in the following manner. The angular coefficient uncertainty can be written in the form (Δ is the uncertainty):

$$\frac{\Delta A_\alpha}{A_\alpha} = \sqrt{\left(\frac{\Delta V_{e1}}{V_{e1}}\right)^2 + \left(\frac{\Delta V_{e2}}{V_{e2}}\right)^2} \tag{B.13}$$

The velocity coefficient U_{cf} is :

$$\frac{\Delta U_{cf}}{\Delta \alpha} = \sqrt{\left(\frac{dU_{cf}}{d\alpha}\right)^2} \tag{B.14}$$

For a 90° probe wire angle the calculated uncertainty in the measured angle are calculated to be $\Delta\alpha = \pm 0.79°$.

APPENDIX C

ERRORS IN LDV MEASUREMENTS

LDV measurements are subject to numerous errors, most of which can be quantified. The discussion here, which is based on the error analysis of Patrick (1987) uses the ASME measurement uncertainty analysis to calculate the uncertainty (also described by Zaccaria, 1994). The errors are separated into both precision and bias errors. Bias errors include errors from laser beam geometry, counter processor errors and seeding bias errors. The laser beam geometrical errors consist of finite probe volume bias, beam location bias, beam orientation bias, fringe spacing uncertainty bias, negative velocity beam bias, angle bias and frequency broadening bias. The processor bias errors are made up of errors due to comparison accuracy, clock synchronization, quantizing, threshold limit, electronic noise and pedestal filter removal. Finally, the seeding bias errors include errors resulting from the flow distortion, particle lag, statistical or velocity bias and Bragg cell bias. Most of the bias errors are very small compared to the precision errors (discussed below), and thus are neglected. The bias errors which can be on the order of magnitude of the precision errors are discussed in detail below.

Statistical or velocity biasing was first mentioned by McLaughlin and Tiederman (1972). It occurs as a result of two reasons. The first is that the velocity magnitude varies with time. The second is that in a uniformly seeded flow, more particles pass through the probe volume per unit time during periods when the velocity is greater than when the velocity is

lower than the mean velocity. Thus a high data rate causes the measured values to be biased toward a higher value than the true mean. In the nozzle, where the turbulence intensity was less than 5 %, the error due to statistical bias is less than 0.5% based on the analysis of Strazisar and Powell (1980).

Angle bias occurs when the flow is not parallel to the plane containing the laser beams. The factor controlling the angle bias is the ratio N/N_{fr} , where N is the minimum number of cycles required by the signal processor and N_{fr} is the number of measurable fringes. The angle bias can be minimized by reducing the N/N_{fr} ratio. Frequency shifting was used to minimize the angle bias, and thus this error is negligible also.

The precision errors in LDV measurement are data processing errors which result from averaging a finite number of data samples per data point. In LDV measurements, the velocity being measured does not remain constant during the sampling period but fluctuates due to turbulence. Thus the precision error is

$$S = \sqrt{\frac{\sum_{i=1}^{N} \left(V_i - \overline{V}\right)^2}{N-1}} = v' \qquad \text{(C.1)}$$

where

$$\overline{V} = \frac{1}{N} \sum_{i=1}^{N} V_i \qquad \text{(C.2)}$$

where V_i is the velocity of the i'th sample and $\overline{V}$ is the sample mean velocity. The precision error calculated by equation (C.1) is an estimate of the rms turbulence level. For an infinite number of samples, S becomes an exact measurement of the turbulence level.

For a finite number of samples, both the rms turbulence level, v', and the mean sample velocity $\overline{V}$, will deviate from the true turbulence level and mean velocity of the flow field by precision errors $S_{v'}$ and $S_{\overline{V}}$, respectively. Patterson (1982) states that the mean square turbulence intensity has a Chi-square distribution. Thus for a large sample size (N>50) the precision error of the turbulence intensity measurement can be found from

$$\frac{S_{v'}}{v'} = \frac{1}{\sqrt{2N}} \tag{C.3}$$

Relative to the mean velocity measurements, the sampling distribution of $\overline{V}$ is normal about the population mean $\overline{V}_p$(true mean) as a mean with a standard deviation of $v'_p/\sqrt{N}$. Thus the precision error in the mean velocity measurement can be estimated as

$$\frac{S_{\overline{V}}}{\overline{V}_p} = \frac{1}{\sqrt{N}}\left(\frac{v'_p}{V_p}\right) \tag{C.4}$$

which is a function of the true turbulence intensity,$\left(v'_p/V_p\right)$. The quantity, $\left(v'_p/V_p\right)$, is unknown but can be approximated by the measured ratio of the turbulence to the mean velocity, $\left(v'/\overline{V}\right)$.

For the LDV measurements in the nozzle, where the sample size was 200, the precision errors in the mean velocity and the turbulence intensity are 0.1% and 5.0%, respectively. Thus using equation (A.6), the total uncertainty for a 95% confidence level is as follows,

Nozzle flow field: $S_{\overline{V}}/\overline{V} = 0.2\ \%$

$S_{v'}/V' = 10\ \%$

APPENDIX D

THREE DIMENSIONAL BOUNDARY LAYER GOVERNING EQUATIONS

The governing equations for the three dimensional boundary layer code are defined by Vatsa (1985). The notation includes the following

u_1,u_2,u_3 - velocity components

s_1,s_2,s_3 - boundary layer curvilinear coordinates

h_1,h_2,h_3 - metric scale coefficients

g - Covariant metric tensor

ω - rotor speed

h- enthalpy

The governing set of equations becomes:

Continuity Equation:

$$\frac{\partial}{\partial s_1}\left(\frac{\sqrt{g}}{h_1}\rho u_1\right) + \frac{\partial}{\partial s_2}\left(\frac{\sqrt{g}}{h_2}\rho u_2\right) + \frac{\partial}{\partial s_3}\left(\frac{\sqrt{g}}{h_3}\rho u_3\right) = 0 \qquad \text{(D.1)}$$

Momentum Equation - s_1 direction:

$$\begin{aligned}
&\frac{u_1}{h_1}\frac{\partial u_1}{\partial s_1} + \frac{u_2}{h_2}\frac{\partial u_1}{\partial s_2} + u_3\frac{\partial u_1}{\partial s_3} + u_1u_1\frac{g_{12}}{g}\left\{\frac{g_{12}}{h_1^2}\frac{\partial h_1}{\partial s_1} + \frac{\partial h_1}{\partial s_2} - \frac{1}{h_1}\frac{\partial g_{12}}{\partial s_1}\right\} \\
&\qquad + u_1u_2\frac{1}{g}\left\{h_1h_2\left[1+\left(\frac{g_{12}}{h_1h_2}\right)^2\right]\frac{\partial h_1}{\partial s_2} - 2g_{12}\frac{\partial h_2}{\partial s_1}\right\} \\
&+ u_2u_2\frac{h_1}{g}\left\{\frac{\partial g_{12}}{\partial s_2} - h_2\frac{\partial h_2}{\partial s_1} - \frac{g_{12}}{h_2}\frac{\partial h_2}{\partial s_2}\right\} - 2\frac{h_1h_2}{\sqrt{g}}\omega_3u_2 - 2\frac{g_{12}}{\sqrt{g}}\omega_3u_1 \\
&-\omega^2 r\frac{h_1h_2^2}{g}\frac{\partial r}{\partial s_1} + \omega^2 r\frac{h_1g_{12}}{g}\frac{\partial r}{\partial s_2} + \frac{h_1h_2^2}{\rho g}\frac{\partial p}{\partial s_1} - \frac{h_1g_{12}}{\rho g}\frac{\partial p}{\partial s_2} = \frac{1}{\rho}\frac{\partial}{\partial s_3}\left\{\mu\frac{\partial u_1}{\partial s_3} - \rho\overline{u_1'u_3'}\right\}
\end{aligned} \qquad \text{(D.2)}$$

Momentum Equation - s_2 direction:

$$\frac{u_1}{h_1}\frac{\partial u_2}{\partial s_1}+\frac{u_2}{h_2}\frac{\partial u_2}{\partial s_2}+u_3\frac{\partial u_2}{\partial s_3}+u_1u_1\frac{h_2}{g}\left\{\frac{\partial g_{12}}{\partial s_1}-h_1\frac{\partial h_1}{\partial s_2}-\frac{g_{12}}{h_1}\frac{\partial h_1}{\partial s_1}\right\}$$

$$+u_1u_2\frac{1}{g}\left\{h_1h_2\left[1+\left(\frac{g_{12}}{h_1h_2}\right)^2\right]\frac{\partial h_2}{\partial s_1}-2g_{12}\frac{\partial h_1}{\partial s_1}\right\}$$

$$+u_2u_2\frac{g_{12}}{g}\left\{\frac{g_{12}}{h_2h_2}\frac{\partial h_2}{\partial s_2}-\frac{1}{h_2}\frac{\partial g_{12}}{\partial s_2}+\frac{\partial h_2}{\partial s_1}\right\}+2\frac{g_{12}}{\sqrt{g}}\omega_3u_2+2\frac{h_1h_2}{\sqrt{g}}\omega_3u_1 \qquad \text{(D.3)}$$

$$-\omega^2r\frac{h_2h_1^2}{g}\frac{\partial r}{\partial s_2}+\omega^2r\frac{h_2g_{12}}{g}\frac{\partial r}{\partial s_1}+\frac{h_2h_1^2}{\rho g}\frac{\partial p}{\partial s_2}-\frac{h_2g_{12}}{\rho g}\frac{\partial p}{\partial s_1}=\frac{1}{\rho}\frac{\partial}{\partial s_3}\left\{\mu\frac{\partial u_2}{\partial s_3}-\rho\overline{u_2'u_3'}\right\}$$

Energy Equation :

$$\frac{u_1}{h_1}\frac{\partial h_T}{\partial s_1}+\frac{u_2}{h_2}\frac{\partial h_T}{\partial s_2}+u_3\frac{\partial h_T}{\partial s_3}=\frac{1}{\rho}\frac{\partial}{\partial s_3}\left\{\lambda\frac{\partial t}{\partial s_3}-\rho\overline{u_3'h_r'}+\mu\frac{\partial}{\partial s_3}-\left(\frac{u_T^2}{2}\right)\right\} \qquad \text{(D.4)}$$

$$+\frac{u_1}{2h_1}\frac{\partial}{\partial s_1}\left(\omega^2r^2\right)+\frac{u_2}{2h_2}\frac{\partial}{\partial s_2}\left(\omega^2r^2\right)+\frac{u_2}{2}\frac{\partial}{\partial s_3}\left(\omega^2r^2\right)$$

Additional equations used are given bellow:

Equation of State:

$$p=\rho RT \qquad \text{(D.5)}$$

REPORT DOCUMENTATION PAGE

Form Approved
OMB No. 0704-0188

1. AGENCY USE ONLY (*Leave blank*)	2. REPORT DATE	3. REPORT TYPE AND DATES COVERED
	May 1997	Final Contractor Report

4. TITLE AND SUBTITLE

Three Dimensional Viscous Flow Field in an Axial Flow Turbine Nozzle Passage

5. FUNDING NUMBERS

WU–523–26–33
G–NAG3–555

6. AUTHOR(S)

D. Ristić and B. Lakshminarayana

7. PERFORMING ORGANIZATION NAME(S) AND ADDRESS(ES)

Pennsylvania State University
Department of Aerospace Engineering
University Park, Pennsylvania 16802

8. PERFORMING ORGANIZATION REPORT NUMBER

E–10772

9. SPONSORING/MONITORING AGENCY NAME(S) AND ADDRESS(ES)

National Aeronautics and Space Administration
Lewis Research Center
Cleveland, Ohio 44135–3191

10. SPONSORING/MONITORING AGENCY REPORT NUMBER

NASA CR–4779

11. SUPPLEMENTARY NOTES

Project Manager, Robert J. Boyle, Turbomachinery and Propulsion Systems Division, NASA Lewis Research Center, organization code 5820, (216) 433–5889.

12a. DISTRIBUTION/AVAILABILITY STATEMENT

Unclassified - Unlimited
Subject Category 34

This publication is available from the NASA Center for AeroSpace Information, (301) 621–0390.

12b. DISTRIBUTION CODE

13. ABSTRACT ***(Maximum 200 words)***

The objective of this investigation is experimental and computational study of three dimensional viscous flow field in the nozzle passage of an axial flow turbine stage. The nozzle passage flow field has been measured using a two sensor hot-wire probe at various axial and radial stations. In addition, two component LDV measurements at one axial station (x/c_m=0.56) were performed to measure the velocity field. Static pressure measurements and flow visualization, using a fluorescent oil technique, were also performed to obtain the location of transition and the endwall limiting streamlines. A three dimensional boundary layer code, with a simple intermittency transition model, was used to predict the viscous layers along the blade and endwall surfaces. The boundary layers on the blade surface were found to be very thin and mostly laminar, except on the suction surface downstream of 70% axial chord. Strong radial pressure gradient, especially close to the suction surface, induces strong cross flow components in the trailing edge regions of the blade. On the endwalls the boundary layers were much thicker, especially near the suction corner of the casing surface, caused by secondary flow. The secondary flow region near the suction-casing surface corner indicates the presence of the passage vortex detached from the blade surface. The corner vortex is found to be very weak. The presence of a closely spaced rotor downstream (20% of the nozzle vane chord) introduces unsteadiness in the blade passage. The measured instantaneous velocity signal was filtered using FFT square window to remove the periodic unsteadiness introduced by the downstream rotor and fans. The filtering decreased the free stream turbulence level from 2.1% to 0.9% but had no influence on the computed turbulence length scale. The computation of the three dimensional boundary layers is found to be accurate on the nozzle passage blade surfaces, away from the endwalls and the secondary flow region. On the nozzle passage endwall surfaces the presence of strong pressure gradients and secondary flow limit the validity of the boundary layer code.

14. SUBJECT TERMS

Turbine aerodynamics

15. NUMBER OF PAGES

197

16. PRICE CODE

A09

17. SECURITY CLASSIFICATION OF REPORT	18. SECURITY CLASSIFICATION OF THIS PAGE	19. SECURITY CLASSIFICATION OF ABSTRACT	20. LIMITATION OF ABSTRACT
Unclassified	Unclassified	Unclassified	